Template-Assisted Materials Engineering

by

Jung Hun (Kevin) Song

A dissertation submitted to the Graduate Faculty in Chemical Engineering in partial
fulfillment of the requirements for the degree of Doctor of Philosophy
The City University of New York

2009

This manuscript has been read and accepted for the Graduate Faculty in Engineering in satisfaction of the dissertation requirements for the degree of Doctor of Philosophy.

Date

Dr. Ilona Kretzschmar
Chair of Examining Committee

Date

Dean Mumtaz Kassir
Executive Officer

Dr. Alexander Couzis

Dr. Charles Maldarelli

Dr. Raymond Tu

Dr. Vinod Menon

Supervision Committee

THE CITY UNIVERSITY OF NEW YORK

Abstract

Template-Assisted Materials Engineering

by

Jung Hun (Kevin) Song

Advisor: Ilona Kretzschmar

Recent developments in colloidal assembly have led to novel fabrication techniques for nano- and microscopic materials of interest to many fields of science and engineering. The design of more complex processes and applications requires a greater variety of versatile preparation techniques. In this thesis, we present the application of Template-Assisted Materials Engineering (TAME) to obtain porous polymeric materials using various types of colloids and explore potential applications of the resulting porous materials.

TAME is used to fabricate three-dimensional (3D) colloidal assemblies within geometric confinement. Further, we show that TAME can be used as a secondary template to form porous polymeric materials retaining the shape of the templating confinement. Advantages of utilizing TAME in colloidal assembly are the precise positioning and sizing of colloidal assemblies. For porous materials, advantages include control over pore size and distribution, porosity, shape, and materials. Building on these advantages, the TAME technique is employed to fabricate multi-sectional porous polymeric fibers with controlled sections of varying pore structure and is subsequently extended to synthesizing a multi-stage catalytic membrane reactor using catalyst-coated, surface-anisotropic colloids. Further, the versatility of the TAME approach is illustrated by applying it to the fabrication of macroscopic, porous materials using a biodegradable polymer and PDMS. Last but not least, TAME is applied to assemble 3D colloidal crystals for the study of photonic properties using fluorescently tagged and novel, magnetically enhanced colloids.

Overall, TAME is shown to be a versatile, yet precise fabrication technique that can be employed in the preparation of materials for a wide range of applications. In addition, the intrinsic control over the colloidal assembly and the resulting porous materials make TAME an effective and efficient method for obtaining functional 3D materials.

Acknowledgements

First and foremost, I offer my sincerest gratitude to my advisor, Prof. Ilona Kretzschmar, who has shown relentless encouragements, guidance, and support for me and this thesis work. It is her never-ending passion and commitment to her students, research, and lab that made this thesis work possible. It is truly a great honor to have met and worked with her.

In addition, I would like to thank my thesis committee members, Prof. Alexander Couzis, Prof. Charles Maldarelli, Prof. Vinod Menon, and Prof. Raymond Tu for their guidance and insightful discussions in the respective fields to further advance and improve this thesis work. I would like to express my appreciations to Prof. Menon and Mr. Harish Natarajan S K for the photonics studies in this work.

Further, this thesis work would not have been possible without great assistance and discussions from the current and former *Kretzschmar Lab* members – Dr. Amar Pawar, Dr. Jingqin Cui, Ms. Sonia Matthews, Ms. Hsin-Yu Chen, and Mr. Bin Ren. All the undergraduate researchers who have worked on many of the projects are deeply appreciated for their help in sample preparations and characterization. Also, Mr. Andy Eng, Mr. Zhengrong Xu, and Ms. Lisa Taylor are greatly appreciated for their support and help with many technical and clerical jobs. Lastly, great friends and memories made during the years at CCNY made my graduate student life unique and unforgettable - Dr. Cesare Ciani, Mr. Chi Lo, Ms. Lorraine Leon, Mr. Philip Mathews, Mr. Spyridon Monastiriotis, Dr. Tieuvi Nguyen, and Dr. Stewart Russell.

Finally, I would like to dedicate this thesis to my parents, Mr. Byung Song and Mrs. Jung Song. It is there continuing love, support, sacrifice, and guidance that made this work possible and for me to be here. Without them, this would not have been possible. Thank you!!!

Jung Hun (Kevin) Song

August 2009

Contents

List of Figures

List of Tables

Chapter 1

Introduction

Development of novel hierarchical materials is at the heart of the continuously evolving fields of micro- and nanotechnology. During the past several decades, micro- and nanotechnology have focused on developing innovative techniques to synthesize and fabricate multi-functional, three-dimensional (3D) materials.[1, 2] 3D materials, in contrast to many existing one- and two-dimensional (2D) materials, possess unique and functional properties that demonstrate a wide applicability in many fields, e.g., catalysis, bioengineering, and photonics.[3-10] Concurrently, innovative fabrication techniques to obtain micro- and nano-scale 3D materials have proven to be difficult and expensive.[11-13] To address the obstacles at hand, *Template-Assisted Materials Engineering (TAME)* is employed in the fabrication of multi-functional 3D materials at the micro- and nanometer length scale.

TAME utilizes an object or collection of objects to pattern and mold the desired intermediate and/or final material.[11, 14] By applying TAME to colloidal assembly, controllability and directionality are implemented in the colloidal structure that promise to have a vast impact (e.g., increased efficiency and decreased processing time) on 3D colloidal assembly at the desired scale.[2, 11, 15, 16] Many of the template-free 3D assemblies of micro- and nanometer-sized colloids are obtained by organization of colloids from a suspension on a 1D planar substrate where the action of natural forces dominates the assembly process to result in planar 3D assembly with no directionality.[16-18] In addition, the control of the assembly process, subsequently affecting the quality of the material, is limited to only a few factors including solvent type, ambient temperature and humidity, and the types of surfaces involved.[19, 20] These interactions imposed by natural forces and ambient conditions can be overcome by the implementation of TAME. Utilizing TAME, more complex 3D colloidal materials requiring a high degree of control in shape, size, and structural dimensions can be achieved.[14, 21, 22]

Colloidal assemblies achieved through utilization of TAME can further be employed as sacrificial templates to obtain porous structures.[16, 21, 23] By infiltrating the interstitial spaces with fillers and subsequently removing the templates, an inverse 3D porous material with interconnecting pores is fabricated. The unique nature and properties of the templated colloidal assemblies allow to precisely control the characteristics of the templated porous materials.[17, 21, 24] As a result, templated colloidal assemblies have not only become important for the synthesis of multi-functional 3D materials, but also as a secondary sacrificial template for highly porous 3D materials. With the ever growing interest in complex 3D colloidal assemblies and their colloid-templated porous counterparts, 3D materials fabricated through TAME possess crucial benefits to increasing the efficiency of many potential applications including, but not limited to catalysis[25, 26] and separation engineering,[27] tissue engineering,[28, 29] and photonics.[1, 30, 31]

The thesis aims to develop and apply TAME as a methodology to (i) obtain 3D cylindrical polymeric colloidal assemblies with a controlled number of sections and (ii) fabricate multi-functional porous polymeric materials. Employing different types and sizes of colloids, and different templates, multi-functional cylindrical colloidal assemblies and the resulting porous materials are achieved. This thesis investigates (i) the assembly behavior and structure of the colloidal assemblies in cylindrical templates; (ii) the interaction between the sacrificial colloidal templates and the infiltrating materials; and (iii) the resulting porous structures.

In the following, a detailed literature review of 3D templated colloidal assemblies and colloid-templated porous materials is presented in Chapter 2. In addition, a short section of Chapter 2 is dedicated to the application of 3D templated materials. Chapter 3 focuses on the fabrication of multi-sectional templated colloidal assemblies in a microcapillary and the resulting porous polymeric fibers. Chapter 4 entails utilization of anisotropic colloids as the building block for the fabrication of a catalytic membrane reactor templated in a microcapillary. Chapter 5 is devoted to macro-scale fabrication of porous polymeric material, while Chapter 6 explores the multi-sectional colloidal assembly of fluorescent colloids for application in photonics. The thesis is concluded with a discussion of future work in Chapter 7.

REFERENCES

1. Xia, Y. N.; Gates, B.; Yin, Y. D.; Lu, Y. *Advanced Materials* **2000,** *12*, 693-713.

2. Yang, S. M.; Jang, S. G.; Choi, D. G.; Kim, S.; Yu, H. K. *Small* **2006,** *2*, 458-475.

3. Ulbricht, M. *Polymer* **2006,** *47*, 2217-2262.

4. Chung, T. S. *Polymers & Polymer Composites* **1996,** *4*, 269-283.

5. Karageorgiou, V.; Kaplan, D. *Biomaterials* **2005,** *26*, 5474-5491.

6. Ozdemir, S. S.; Buonomenna, M. G.; Drioli, E. *Applied Catalysis a-General* **2006,** *307*, 167-183.

7. Langer, R.; Tirrell, D. A. *Nature* **2004,** *428*, 487-492.

8. Lee, K. Y.; Mooney, D. J. *Chemical Reviews* **2001,** *101*, 1869-1879.

9. Soten, I.; Ozin, G. A. *Current Opinion in Colloid & Interface Science* **1999,** *4*, 325-337.

10. Waterhouse, G. I. N.; Waterland, M. R. *Polyhedron* **2007,** *26*, 356-368.

11. Wang, D. Y.; Mohwald, H. *Journal of Materials Chemistry* **2004,** *14*, 459-468.

12. Grzybowski, B. A.; Wilmer, C. E.; Kim, J.; Browne, K. P.; Bishop, K. J. M. *Soft Matter* **2009,** *5*, 1110-1128.

13. Rycenga, M.; Camargo, P. H. C.; Xia, Y. N. *Soft Matter* **2009,** *5*, 1129-1136.

14. Dziomkina, N. V.; Vancso, G. J. *Soft Matter* **2005,** *1*, 265-279.

15. Stein, A.; Schroden, R. C. *Current Opinion in Solid State & Materials Science* **2001,** *5*, 553-564.

16. Velev, O. D.; Lenhoff, A. M. *Current Opinion in Colloid & Interface Science* **2000,** *5*, 56-63.

17. Jiang, P.; Bertone, J. F.; Hwang, K. S.; Colvin, V. L. *Chemistry of Materials* **1999,** *11*, 2132-2140.

18. Kotov, N. A.; Liu, Y. F.; Wang, S. P.; Cumming, C.; Eghtedari, M.; Vargas, G.; Motamedi, M.; Nichols, J.; Cortiella, J. *Langmuir* **2004,** *20*, 7887-7892.

19. Jin, C. J.; McLachlan, M. A.; McComb, D. W.; De La Rue, R. M.; Johnson, N. P. *Nano Letters* **2005,** *5*, 2646-2650.

20. Singh, K. B.; Tirumkudulu, M. S. *Physical Review Letters* **2007,** *98*.

21. Song, J. H.; Kretzschmar, I. *Langmuir* **2008,** *24*, 10616-10620.

22. Yang, P. D.; Rizvi, A. H.; Messer, B.; Chmelka, B. F.; Whitesides, G. M.; Stucky, G. D. *Advanced Materials* **2001,** *13*, 427-431.

23. Yan, F.; Goedel, W. A. *Advanced Materials* **2004,** *16*, 911-915.

24. Jiang, P.; Hwang, K. S.; Mittleman, D. M.; Bertone, J. F.; Colvin, V. L. *Journal of the American Chemical Society* **1999,** *121*, 11630-11637.

25. Sedlacek, B.; Kahovec, J., *Synthetic Polymeric Membranes*. Walter De Gruyter: New York, 1987.

26. Lloyd, D., *Materials Science of Synthetic Membrane*. American Chemical Society: Washington D.D., 1985.

27. Sirkar, K.; Lloyd, D., *New Membrane Materials and Processes for Separation*. American Institute of Chemical Engineers: New York, 1988; Vol. 84.

28. Park, J.; Bronzion, J., *Biomaterials - Principles and Applications*. CRC Press: Boca Raton, 2003.

29. Vieth, W. R., *Membrane Systems: Analysis and Design*. Oxford University Press: Munich, 1988.

30. Miguez, H.; Yang, S. M.; Ozin, G. A. *Langmuir* **2003,** *19*, 3479-3485.

31. Miguez, H.; Yang, S. M.; Ozin, G. A. *Applied Physics Letters* **2002,** *81*, 2493-2495.

Chapter 2

Template-Assisted Materials Engineering (TAME)

Chapter 2 gives a brief overview of recent advances in template-assisted materials engineering (TAME) from the perspective of nano- and micro-scale colloidal science and engineering. The first section explores the various techniques currently employed in the fabrication of three-dimensional (3D) colloidal assemblies with an emphasis on template-assisted assembly using cylindrical confinement. In the subsequent section, porous polymeric materials templated by 3D colloidal assemblies are introduced. Lastly, analysis and potential functionality of nano- and micro-scale templated materials are discussed.

2.1 Template-Assisted Three-Dimensional Colloidal Assembly

The two main methodologies employed in the fabrication of 3D colloidal assemblies are free-standing and template-assisted colloidal assemblies.[1] The free-standing assembly approach includes all methods that result in the assembly of colloids without any physical restrictions or entrapments.[2] On the other hand, template-assisted 3D assembly involves the assembly of colloids in a scaffold or guide with a predefined geometry that is used to arrange the colloidal particles with the aim of influencing the outcome of a subsequent process.[3-6] Many of the template-assisted 3D colloidal assembly methods are in part derived from free-standing colloidal assembly. Therefore, it is important to understand the fundamentals behind the free-standing assembly approach. Of particular importance to the thesis work are assembly techniques that result in assemblies at interfaces and in geometrical confinement.

2.1.1 Free-Standing Colloidal Assemblies

Recently, many free-standing colloidal assembly (FSCA) techniques have been explored because of their wide applicability and advantages.[7-9] One of the most facile FSCA techniques is sedimentary assembly (Figure 2.1A).[2,10] Although it has proven to be the most facile route, the technique is deficient in obtaining colloidal assemblies with efficient processing time, reliability, and reproducibility.[11] In contrast to the sedimentary assembly, the flotation assembly technique (Figure 2.1B) has been reported to be a more efficient and reliable technique. Kotov et al.,[8, 9] Park et al.,[12-14] Tong et al.,[15] and Goedel et al.[7] have extensively worked on developing a simple, yet widely applicable method, the so-called *flotation self-assembly of colloids*. Flotation self-assembly of colloids is driven by a minute difference in densities between the colloids and the solvent, which allows the colloids to float at the air-solvent interface (Figure 2.2). Some of the advantages that flotation self-assembly offer are (i) applicability of the methodology across varying sizes of colloids; (ii) potential fabrication of larger, long-range ordered colloidal assemblies, and (iii) shorter assembly times.[8]

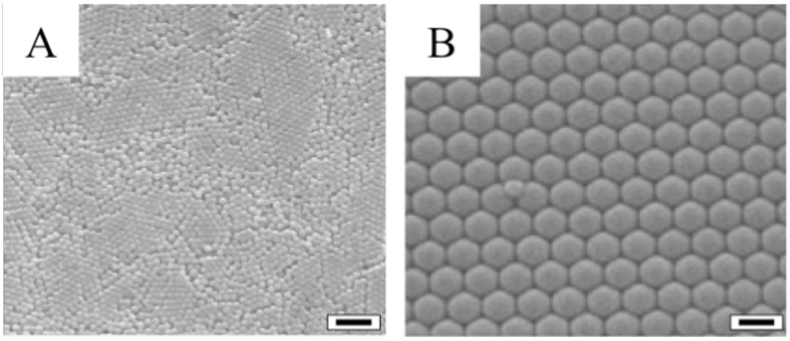

Figure 2.1 Three-dimensional colloidal assemblies. (A) Colloidal assembly of sub-micron polymeric colloids using sedimentation assembly.[16] Scale bar 1 µm. (B) Colloidal assembly of sub-micron polymeric colloids using flotation self-assembly.[13] Scale bar 250 nm.

Several forces govern the interactions in the flotation self-assembly.[8] These forces include buoyancy, gravity, lateral capillary forces (floating and immersion), and electrostatic forces (attractive and repulsive).[17, 18] Among these forces, vertical forces, which include buoyancy, gravity, and immersion lateral capillary forces, are major forces that govern the floatation behavior of the colloids within the solution. The buoyancy force is the dominating force caused by the density difference between the colloids and the solvent, where the less-dense colloids rise through the more-dense solvent. Second to the buoyancy force is gravity, which competes against the buoyancy force to settle the colloids towards the bottom.[8, 17] Following gravitational forces, the lateral capillary forces are the weakest forces, yet have the greatest importance in the subtle arrangement of colloids at the interface and ultimately determine the quality of the 3D colloidal assembly.

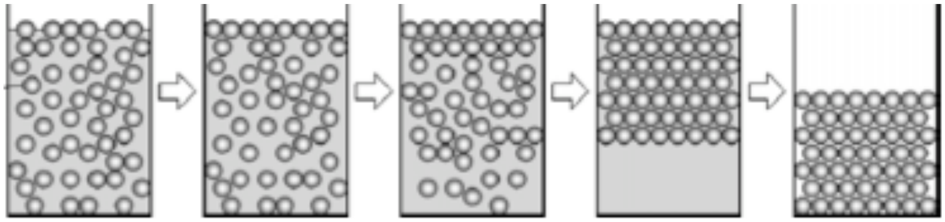

Figure 2.2 Schematics of floating self-assembly.[9] Colloids suspended in a less-dense solvent rise through the solution to the solvent-air interface. Owing to capillary forces, the neighboring colloids are organized into a close-packed structure resulting in a 3D colloidal assembly.

Lateral capillary forces are caused by the perturbations of the meniscus or the liquid interface between the colloids. Two similar colloids floating at a liquid interface are attracted to each other due to the deformation of the interface between them. Larger deformation of the interface usually leads to greater attraction of the colloids.[17] The deformation causes a decrease in the gravitation potential energy of the colloids allowing their aggregation at the surface. This effect is called the *flotation capillary force* and is depicted in Figure 2.3A. An additional attraction, the so-called *immersion capillary force*, occurs between colloids that are partially immersed or confined in a liquid layer as shown by Figure 2.3B. Here, the attraction results from the deformation of the liquid surface caused by the wetting properties (the position of the contact line and the contact angle) of the particles.[17, 19] Note depending on the shape of the interface deformation, interaction forces may also be repulsive as depicted in Figures 2.3 C and D.

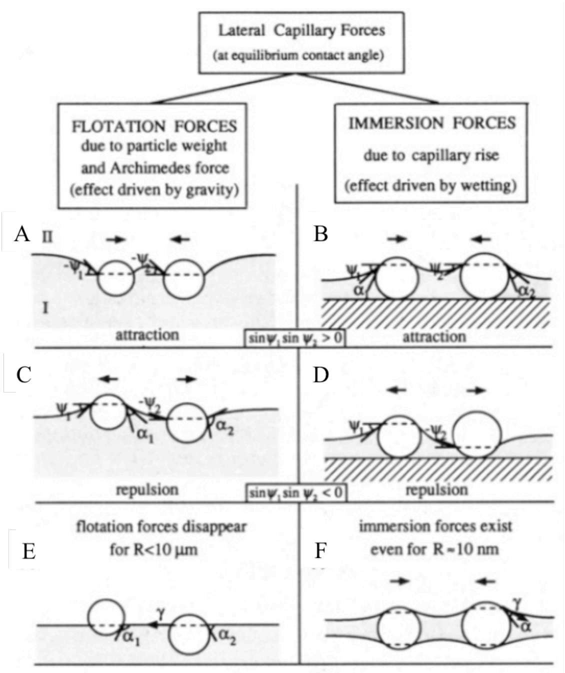

Figure 2.3 Attractive and repulsive colloidal interactions caused by different interface deformations. (A) Attractive flotation. (B) Attractive immersion. (C) Repulsive flotation. (D) Repulsive immersion. (E) Absences of flotation force R < 10 μm. (F) Presence of immersion force R → 10 nm.[19]

Lateral capillary forces are described by solving the Laplace equation of capillarity for a small meniscus slope as shown in Equation 2.1.[17]

$$\nabla^2\zeta = q^2\zeta \tag{2.1}$$

$$\begin{aligned} q^2 &= \frac{\Delta\rho g}{\sigma} \text{ for thick films} \\ q^2 &= \frac{(-\Pi')}{\sigma} \text{ for thin films} \end{aligned} \tag{2.2}$$

where ζ is the interfacial shape around a single particle, Δρ is the difference between the mass density of the two fluids, Π' is the derivative of the disjoining pressure with respect to film thickness, and σ is the surface tension between the fluid and the colloids. The interfacial shape, exponentially decaying at infinity, is expressed by Equation 2.3 in cylindrical coordinates.

$$\zeta(r) = AK_0(qr) \tag{2.3}$$

where K_0 is the modified Bessel function of the second kind and zeroth order, A is a constant of integration, and r is the radial coordinate of the curvature of the meniscus. From the above equations, the lateral capillary interaction energy between two colloids is derived through the application of the superposition approximation.[19, 20] This approximation assumes that the interfacial deformation caused by two colloidal particles is equal to the sum of the deformations caused by the individual colloids in isolation.[21] The lateral capillary interaction energy with respect to the Laplace equation is expressed by Equation 2.4:

$$\Delta W \approx -2\pi Q_1 Q_2 K_0(qL) \tag{2.4}$$

where ΔW is the variation in the lateral capillary interaction energy (gravitational energy for *flotation force* and wetting energy for *immersion force*), L is the distance between the centers of the two colloids, and Q_i is the capillary charge. Capillary charge, expressed by Equation 2.5, accounts for the local deviation of the meniscus shape from planarity at the three phase contact line.

$$Q_i \equiv r_i \sin\psi_i \tag{2.5}$$

where r_i is the radii of the contact line and ψ_i is the slope angle at the contact line with respect to the colloidal particle *i*. From the variation in the lateral capillary interaction energy, the lateral capillary force is derived as shown in Equation 2.6.

$$F = -\frac{d\Delta W}{dL} \tag{2.6}$$

Lateral capillary forces are derived combining Equations 2.4 – 2.6 yielding Equation 2.7 (generalized) and 2.8 (asymptotic: qL<< 1).

$$F = -2\pi Q_1 Q_2 q K_1(qL) \tag{2.7}$$

$$F = -\frac{2\pi Q_1 Q_2}{L} \quad \text{asymptotic form} \tag{2.8}$$

where K_1 is the modified Bessel function. In the particular case, where the radii of the colloids are equal and the separation lengths between colloids is in the range of the radius of curvature of the meniscus and the capillary length, the following relationships for flotation and immersion forces are derived, Equation 2.9.

$$\begin{aligned} F &\propto \left(\frac{R^6}{\sigma}\right) K_1(qL) \ \text{for flotation force} \\ F &\propto R^2 \sigma K_1(qL) \ \text{for immersion force} \end{aligned} \tag{2.9}$$

From Equation 2.9, it is apparent that the flotation force decreases and that the immersion force increases as the interfacial (surface) tension increases. In addition, the flotation force shows a greater dependence on the radius of the colloids in comparison to the immersion force. The flotation force is shown to be negligible below a colloidal radius of 5 μm, while the immersion force is still significant even down to a 2 nm colloid radius, as depicted in Figures 2.4 E and F.[17, 19, 20] The interactions between the electrostatic and lateral capillary forces have been characterized by Paunov[22] and the interested reader is referred to his review article. However, it is critical to mention that the lateral capillary force dominates over the electrostatic repulsive force in 3D colloidal assembly.[8]

Due to the forces described above, nucleation of a free-standing 3D colloidal assembly occurs at the liquid-air interface. In addition to a sustained buoyancy and the acting lateral capillary forces, convective forces (onset of evaporation) drive the close-packed assembly of the 1st layer.[8] The close-packed 1st layer acts as a nucleation template for subsequent layers. As a result a layer-by-layer assembly of colloidal particles is achieved that is mainly driven by the buoyancy force.[8] The long-range movements or Brownian motion of particles are significantly reduced by the crystallization and colloidal particles become practically fixed at their respective positions. As the solution evaporates from the system, a self-assembled 3D colloidal structure is obtained.

2.1.2 Template-Assisted Colloidal Assemblies

As more complex applications are introduced and developed in the field of colloidal science and engineering, the development of novel, tailorable and controllable colloidal assembly techniques has also prospered. In addressing the ever-growing demand, template-assisted colloidal assembly (TACA) is employed. TACA allows precise and convenient control over the colloidal assembly by merely changing the shape and dimensions of the template.[23] In addition, the templates utilized for the assemblies affect the phase behavior by expanding the types of lattices that can be obtained lending itself to multiple colloidal crystallinity within one assembly.[5, 24] Different templates have been explored ranging from filters to slit fillers to patterned surfaces.[2, 6, 25] TACA has shown to be an effective tool to obtain engineered colloidal assemblies by allowing "*nature to do your work"*.[26]

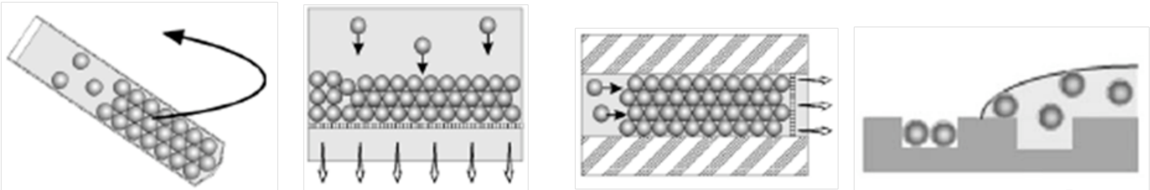

Centrifugation **Filtration** **Slit Filling** **Patterned Surface**

Figure 2.4 Different types of template-assisted assembly.[2] (A) Centrifugation. (B) Filtration. (C) Slit filling. (D) Patterned Surface.

Each template is employed to obtain a specific colloidal assembly. Centrifugation allows "one-pot" colloidal assembly by enhanced gravitational sedimentation of colloids as shown in Figure 2.4A. Due to the induced packing through gravitational forces, colloidal assemblies obtained from centrifugation exhibit local to long-range ordering. Filtration and slit filling techniques employ the same theoretical background in that both methods allow the fast removal of the solvent from the colloidal solution utilizing small cavities present along the sides of the template,[2] as shown in Figures 2.4 B and C. Both methods offer a faster assembly process in comparison to sedimentation.[2] However, the difference between the filtration and the slit filling techniques is that the filtration technique does not require a geometrical confinement, while the slit filling technique confines the colloids between two parallel walls. Patterned-surface assembly of colloids offers another precise control in 3D colloidal assembly (Figure 2.5).[5, 24] Substrates with various patterns have shown to produced extrinsic colloidal assemblies that are not found or hard to obtain naturally. Many patterned surfaces result in unique colloidal assembly shapes such as channels,[27, 28] spherical,[1] ellipsoidal,[29] and rectangular shaped assemblies.[30-32]

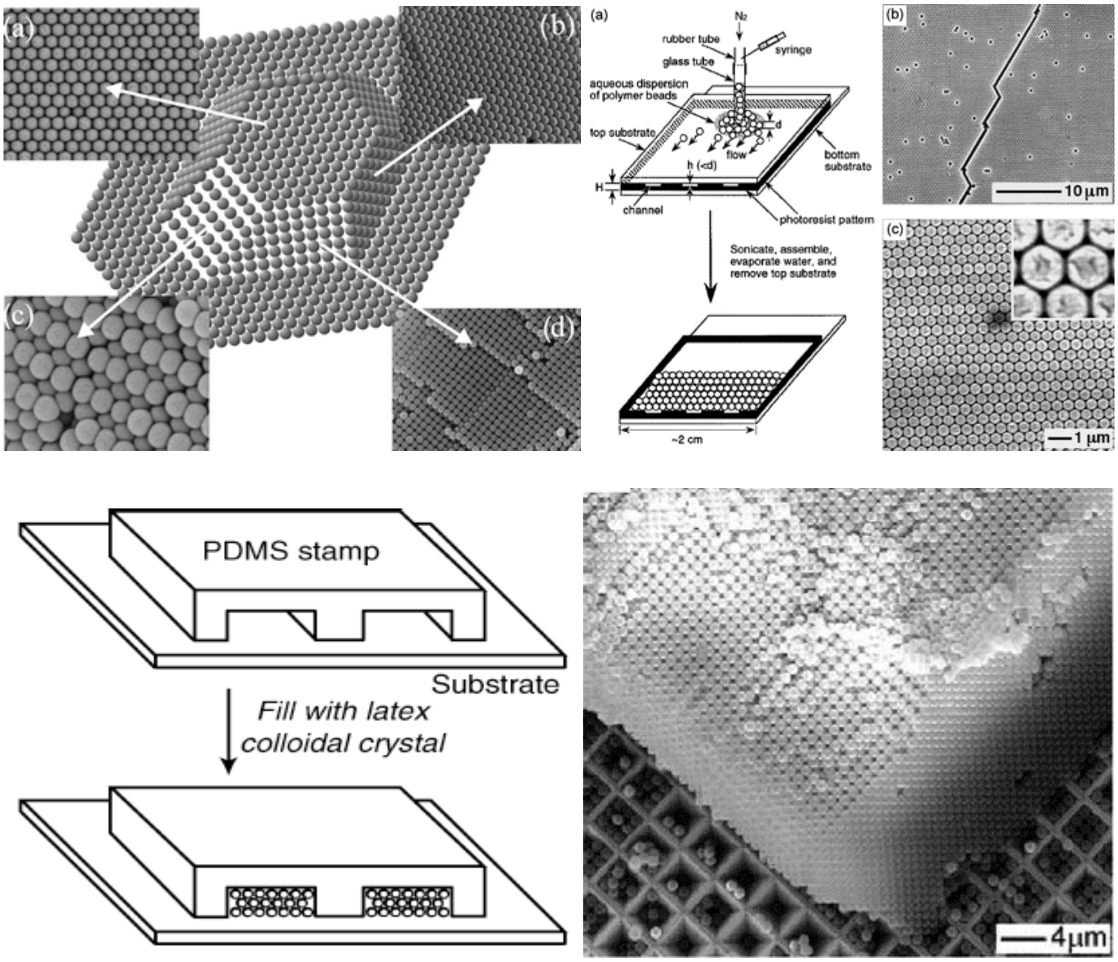

Figure 2.5 Template-Assisted Colloidal Assemblies. (Upper Left) Different colloidal assembly obtained through TACA using patterned surfaces with facets at various angles and patterns.[5] (Upper Right) Filtration technique employed to obtain 3D Face Center Cubic colloidal crystal.[33] (Lower Left) Slit filling of colloids inside PDMS channels.[34] (Lower Right) Square-packed assembly of colloids using a pyramidally patterned surface.[5]

In addition to the various templates listed above, cylindrical templates posses interesting characteristics that are crucial to various applications including membranes, scaffolds, and photonics owing to the radial symmetry and the axial directionality.[35] The physical forces involved in cylindrical colloidal assembly are occurring in everyday life and are summarized under the term “capillary rise”, which describes the initial movement of a fluid in a cylindrical capillary.

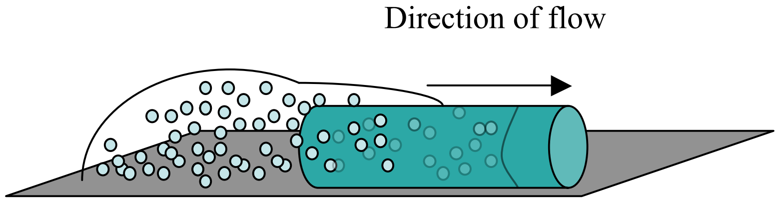

Figure 2.6 Schematic of capillary rise of a colloidal solution in a polymeric capillary.

The capillary rise or Laplace flow occurs in a capillary due to the difference in hydrostatic pressure within a liquid, which is created by the interfacial deformation, i.e., the curvature of the liquid surface, as mentioned in the previous section. As a result of the pressure difference, the liquid in a higher pressure region will flow towards the region of lower pressure as depicted in Figure 2.6.[36] In the following section, the Laplace relationship with respect to the flow in a cylindrical capillary is reviewed.

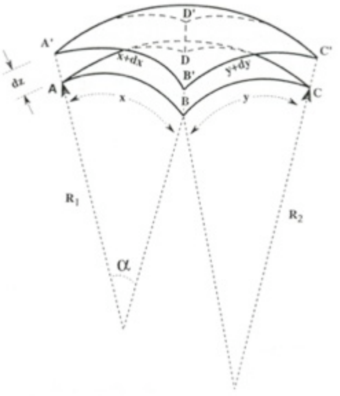

Figure 2.7 Curved surface view used to analyze the Laplace equation.[37]

As shown in the Figure 2.7, the increase in the area along the radii R_1 and R_2 results in a change of the surface area, *dA*, as shown by Equation 2.10.

$$dA = (x + dx)(y + dy) - xy = xdy + ydx + dxdy \tag{2.10}$$

$$dA = xdy + ydx \tag{2.11}$$

Equation 2.10 is further reduced to Equation 2.11 by the fact that the changes, *dx* and *dy*, in their respective directions are minute compared to the values of x and y. The change in the surface free energy associated with the change in the area is given by Equation 2.12.[37]

$$dG = \sigma dA \tag{2.12}$$

where G is the surface free energy, and σ is the surface tension. The surface free energy is equated to the work required to move the interface through a specific volume element, Equation 2.13.

$$\sigma(xdy + ydx) = \Delta pxydz \tag{2.13}$$

The arc length of both x and $(x + \Delta x)$ is related by the angle α, Equation 2.14.

$$\begin{matrix} x = R_1\alpha \\ y = R_2\alpha \end{matrix} \text{ and } \begin{matrix} (x + \Delta x) = (R_1 + dz)\alpha \\ (y + \Delta y) = (R_2 + dz)\alpha \end{matrix} \tag{2.14}$$

where R_I is the radius of curvature in the respective directions. Substitution of Equation 2.14 into Equation 2.13, results in the capillary rise for a tube, Equation 2.15.

$$\Delta p = \sigma(\frac{1}{R_1} + \frac{1}{R_2}) \tag{2.15}$$

In the case of a spherical surface in a thin capillary, where $R_1 = R_2 = R_s$, Equation 2.15 simplifies into Equation 2.16.

$$\Delta p = \frac{2\sigma}{R_c} \tag{2.16}$$

Furthermore, an approximation of the height rise can be determined by balancing the hydrostatic pressure with the vertical component of the surface tension as expressed by Equation 2.17.

$$\frac{2\sigma\cos\theta}{R_c} = \rho gh = \Delta p \tag{2.17}$$

where h is the height rise caused by balancing of the hydrostatic pressure exerted by the weight of the liquid beneath the interface with the surface tension.

As stated above, the initial driving force for the cylindrical assembly comes from the capillary flow. However, after the initial capillary rise, the colloidal crystallization and assembly occurs by convective assembly because of the evaporation of the solvent at the open end of the capillary.[17, 21, 38, 39] Kim et. al.[21, 40] have modeled the flow behavior of numerous multiphase colloidal solutions to determine the liquid throughput/evaporation rate in cylindrical TACA. The equations of continuity for the solid and liquid phases are used in the model expressed by Equation 2.18.

$$\begin{aligned} &\frac{\partial \phi}{\partial t} + \nabla \cdot (\phi V_s) = 0 \\ &\frac{\partial (1-\phi)}{\partial t} + \nabla \cdot ((1-\phi) V_f) = 0 \end{aligned} \tag{2.18}$$

where ϕ is the volume fraction of colloids in a homogeneous solution, and V_s and V_f are the velocities of solid and liquid, respectively. The two continuity equations, Equation 2.18, are summed for the volume-average velocity of a colloidal solution, Equation 2.19.

$$\begin{aligned} &\nabla \cdot q = 0 \\ &q = (1-\phi) V_f + \phi V_s = -(1-\phi) u + V_s \\ &u = V_s - V_f \end{aligned} \tag{2.19}$$

where q is the flow rate and u is the slip velocity of the colloids. Bürger et al,[41] derived a simplified momentum equation for the solid and the liquid, where the effective solid stress function and solid-fluid interaction have been integrated. The combined continuity and momentum equation of the solid is shown in Equation 2.20.

$$\frac{\partial \phi}{\partial t} + \nabla \cdot (\phi q) = \frac{\partial}{\partial x}\left(A(\phi) \frac{\partial \phi}{\partial x} \right) \tag{2.20}$$

where A(ϕ) is a value obtained using the resistance coefficient, the effective solid stress function, the viscosity, and the volume fraction.[21] The flow rate or evaporation rate at the open-end of the capillary, can be estimated through a simple diffusion model using a set of boundary conditions[21] or via experiments. Kim et al.[21] show that the length of the packed colloidal assembly increases and the growth rate decrease slightly with time. The results of their simulations are depicted in Figures 2.8 A and B.

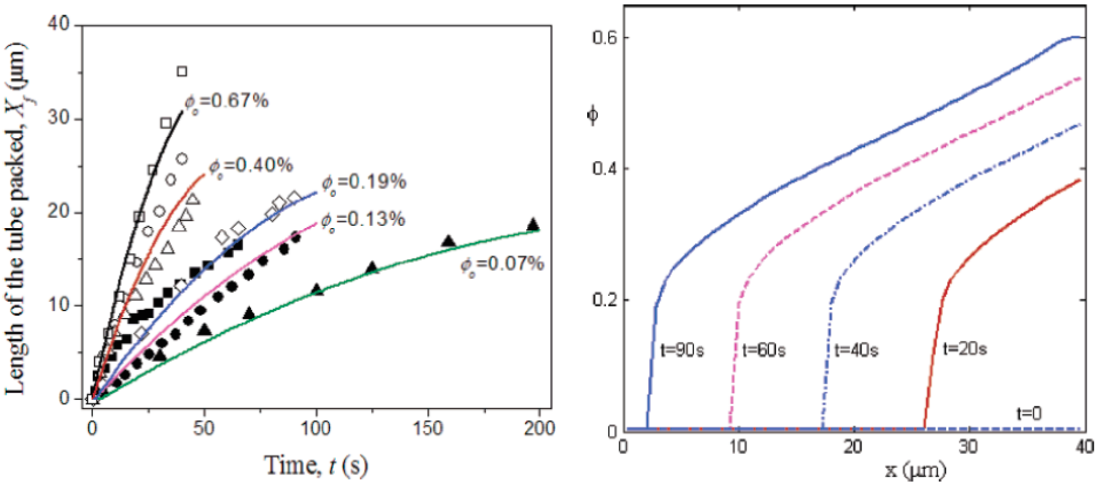

Figure 2.8 Capillary Filling. (a) Length of colloidal filling, x, as a function of time, t, and volume fraction used, ϕ. (b) Volume fraction, ϕ, as a function of filling length, x, and the filling time, t.[21]

2.1.3 Packing and Porosity in Cylindrical Confinement

The type of colloidal packing obtained by capillary flow and convective assembly is of interest for many applications including chromatography.[35, 42] The special interest is due to the fact that the colloidal packing within the template determines the porosity within the confinement, permeability through the interstitial spaces, pressure drop, linear velocity, and hydrodynamic dispersion.[43-46] Erickson,[47, 48] Pickett,[49] Mueller,[50] Jorgenson,[51] and Elhert[43] have developed detailed models and simulations to predict the parameters that affect packing arrangements of spherical colloids inside a cylindrical confinement. Their work shows that the essential parameter determining the packing of the colloidal particles is the aspect ratio between the diameter of the cylindrical template and the diameter of the colloids.[43, 52] For the determination of the aspect ratio, the packing algorithms use uniform spherical colloids in a fixed cylindrical domain. The aspect ratios investigated range from 1.8 to 20.3.[49, 50]

Pickett's study concentrates on the packing behavior of colloids in the aspect ratio ranges of ~1.8 to ~2.155, as shown in Figure 2.9. The study defines six domains of packing regions.

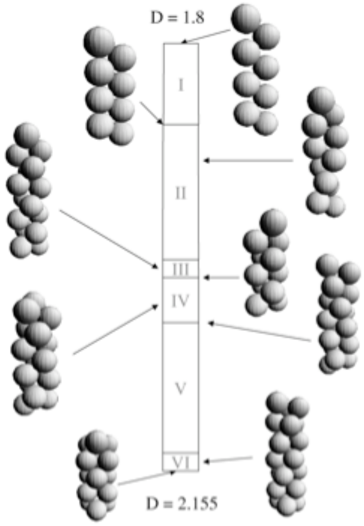

Figure 2.9 Close-packed configuration regions of uniform hard spheres. The six ranges are distinguished by the ratio between the cylindrical domain diameter and the hard sphere diameter.[49]

Region 1, with the aspect ratio between 1.8 and 1.866, is an achiral phase consisting of a zigzag planar arrangement of colloids. Region 2, with the aspect ratio between 1.866 and 1.99, is a chiral phase of two helices. Region 3, with the aspect ratio between 1.99 and 2, consists of two staggered helices and in a notable case where the aspect ratio is 2, achiral doublets are formed. Regions 4, 5, and 6 show two and three staggered and identical "linked" helices, with ratios ranging from 2 to 2.155. Other symmetric packing arrangements may be seen at specific ratios where four, five and seven spheres form a base and where sets of layers may be rotated by 45°, 36°, and 30°, respectively.[48]

Mueller's work tests a wider range of aspect ratios, mainly 2 to 20.3.[50] In his study, Mueller measures the porosity of the colloidal packing within a defined cylindrical domain. The experimental and numerical results have been tabulated and are summarized in Table 2.1.

Table 2.1 Tabulated results of experimental and numerical calculations of porosity determined by aspect ratio (D/h). [50]

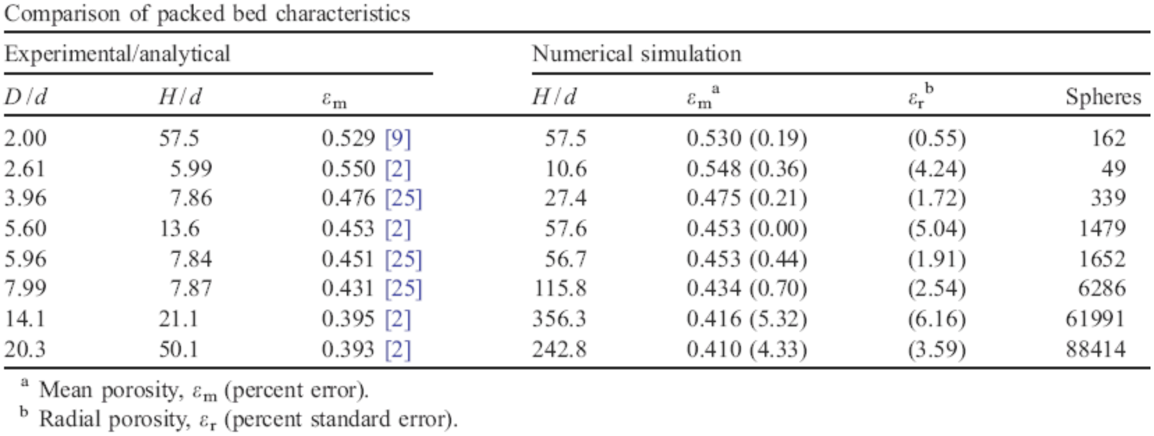

Comparison of packed bed characteristics

Experimental/analytical			Numerical simulation			
D/d	H/d	ε_m	H/d	ε_m[a]	ε_r[b]	Spheres
2.00	57.5	0.529 [9]	57.5	0.530 (0.19)	(0.55)	162
2.61	5.99	0.550 [2]	10.6	0.548 (0.36)	(4.24)	49
3.96	7.86	0.476 [25]	27.4	0.475 (0.21)	(1.72)	339
5.60	13.6	0.453 [2]	57.6	0.453 (0.00)	(5.04)	1479
5.96	7.84	0.451 [25]	56.7	0.453 (0.44)	(1.91)	1652
7.99	7.87	0.431 [25]	115.8	0.434 (0.70)	(2.54)	6286
14.1	21.1	0.395 [2]	356.3	0.416 (5.32)	(6.16)	61991
20.3	50.1	0.393 [2]	242.8	0.410 (4.33)	(3.59)	88414

[a] Mean porosity, ε_m (percent error).
[b] Radial porosity, ε_r (percent standard error).

In addition, radial porosity is studied based on the different aspect ratios. The radial porosity behaves as a dampened sinusoidal function as the porosity is measured from the walls of the cylinder to the center (Figure 2.10). This effect is caused by the geometrical wall effect and the random packing of colloids in the cylindrical geometry.[43]

Based on the numerical solutions of both hard and soft sphere models, colloidal packing is predicted to range from random colloidal packing to regional close packing at the wall region. Typical packing structures obtained from a numerical solution and an experiment are shown in Figure 2.11.

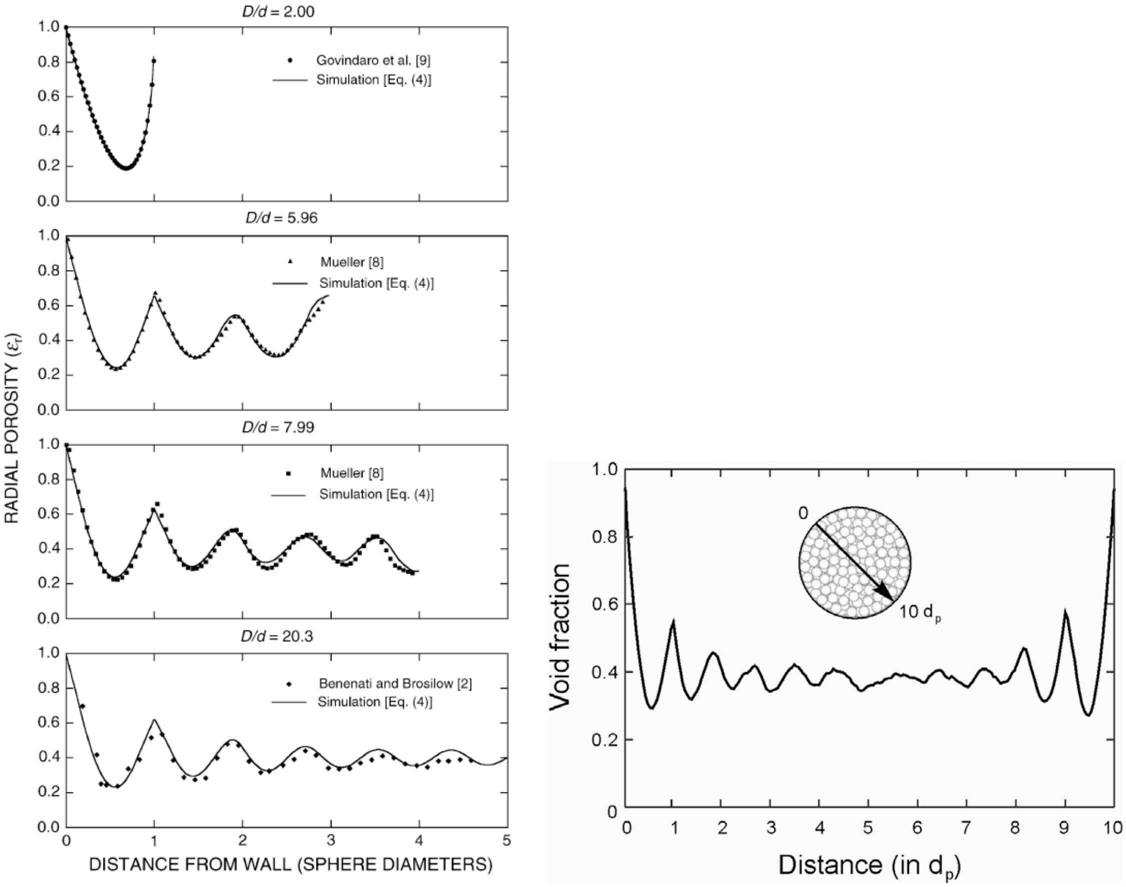

Figure 2.10 Study of radial porosity based on the aspect ratio. (Left) Experimental and simulation radial porosity data as a function of distance away from the wall at different aspect ratios. Aspect ratio increases from top to bottom. (Right) Experimental radial porosity or void fraction as a function of distance.[43, 44, 46]

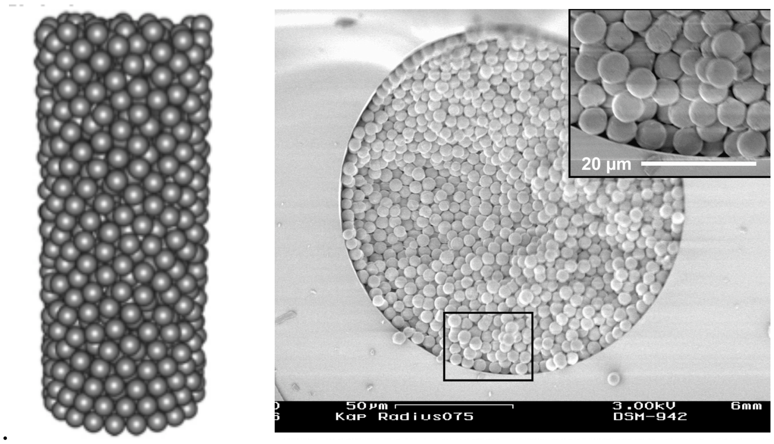

Figure 2.11 Packing of colloids in cylindrical geometry. (Left) Colloidal packing determined using the aspect ratio of 7.99. (Right) The random packing structure is evident in the experimental data taken from Ehlert.[43, 50]

The porosity of colloidal assemblies in cylindrical domains determined from various studies range from 26 to 45% with the packing order ranging from close-packing (26% porosity) to dense random packing (36% porosity) obtained by vibrating or shaking of colloids in the template to very loose random packing (45% porosity) resulting from gradual defluidization of solvents or sedimentation of colloids.[43-46]

2.2 Templated Porous Polymeric Materials

A porous polymeric material (PPM), in its simplest form, is a polymer possessing pores that are formed either intrinsically (by molecular spacing) and/or extrinsically (by application of external forces). PPMs have important applications as membranes, filters, photonic band gap materials, and scaffolds in biology,[53, 54] chemistry,[55] physics,[6] and separation engineering.[55, 56] PPMs are becoming increasingly popular because of their low raw material and fabrication costs. In addition, many PPM fabrication techniques can be easily scaled up or down to produce PPMs with tunable properties such as durability, flexibility, chemical inertness, and transparency. These properties have led to the replacement of traditional porous materials such as ceramics and metals. For example, polyimide membranes have replaced more expensive composite membranes in a large water filtration process.[55] Of particular importance to the thesis work are PPMs templated using colloidal assemblies. In the following, a brief review of the literature available on general porous polymeric materials is given, which leads into enhanced pore size and porosity control in PPMs through colloid templating.

2.2.1 Porous Polymeric Materials

Despite favorable characteristics, PPMs have not yet reached their full potential partially because of the limited control over pore size and porosity.[57] For example, a very narrow pore size distribution with a specific porosity and long-range order is needed for photonic applications.[6] A deviation of as little as 5 to 10% can render a photonic structure unusable.[6] Further, application of PPMs in membrane technology requires precise knowledge of pore size and porosity of the employed PPM to enable the modeling of the separation process and the catalytic efficiency of the membrane reactor.[56, 58, 59] Excellent control over the porosity and pore size also influences the adhesion and proliferation of cells in PPMs used as scaffold.[60]

Currently, the pore size of PPMs is controlled by the molecular precursor (intrinsic pore size) or by the application of chemical or physical processes such as etching or extrusion, respectively. The pore size distributions obtained with these means range from the molecular scale to micrometers.[56] Control of pore size and porosity may potentially improve efficiency of PPMs when applied in the areas of separation and catalysis engineering,[10, 55, 56, 58, 61-65] tissue engineering,[10, 60, 66-68] alternative energy science,[55, 69] and optics/photonics.[6, 10, 34, 70-72]

Polymers are large molecules synthesized from covalent bonding of monomers of identical chemical units. A polymeric material is comprised of a network of polymer chains that exhibits intrinsic pores. The intrinsic pores and their size distribution are determined by the properties of the polymer chains and the conditions under which the polymer is polymerized. Properties affecting the pore size are polarity, steric characteristics, and chemical composition of the main and side chains.[61, 73] Important polymerization parameters are temperature and time, which affect the extent of cross-linking and degree of polymerization leading to variation in the intrinsic pore size and porosity.

In general, a polymer with a higher molecular weight, a higher degree of hydrogen bonding, a higher degree of cross-linking, and a higher glass transition temperature (T_g) posseses smaller pores and a narrower pore-size distribution than a low-molecular weight polymer with a low degree of cross-linking, a low number of H-bonding and a low T_g.[61] For example, polysulfone with ether termination has smaller pores and a narrower pore size distribution due to a more regular structure with a high bulk density of 1.37 g/cm^3, an elevated glass transition temperature (T_g = 220°C), and a lower free volume compared to polysulfone containing an aliphatic isopropyllidene group. The isopropyllidene group reduces the regularity in chain packing and lowers the bulk density to 1.23 g/cm^3 resulting in a reduced glass transition temperature (T_g = 190 °C).[61]

Intrinsic pore sizes for polymeric materials are in the low Ångstrom range (1-10 Å). Due to the very small pore size, pure polymer films are often referred to as non-porous and are considered to be excellent materials for applications in gas separation. The intrinsic porosity of polymers is listed in the literature as less than 2%.[61, 73] The transport through polymer films with pore sizes below 5 Å is best described with the solution-diffusion model, while pore diameters above 10 Å require a pore-flow model.[74, 75]

The pore size of a porous polymeric material is directly related to its porosity and the application for which it is used. Table 2.2 lists the ranges of pore diameters, the corresponding pore size nomenclature, and the area(s) of potential application.[55, 56, 76]

Note that there is no conformity with respect to the nomenclature in the literature, however, the nomenclature given in Table 2.2 is used throughout this project.

Table 2.2 PPM pore size characterization.[55]

Pore Diameter	Nomenclature	Application
molecular spacing	Non-porous	Gas Separation (GS)/Reverse Osmosis (RO)
$d_p < 2$ nm	Microporous	Nanofiltration (NF)
$d_p = 2 – 50$ nm	Mesoporous	Ultrafiltration (UF)
$d_p > 50$ nm	Macroporous	Microfiltration (MF)

Figure 2.12 shows exemplary scanning electron microscope (SEM) images of mesoporous (Celgard, d_p = 20-40 nm), and macroporous (Acurell, d_p = 200 nm) polypropylene PPMs, as well as a mesoporous polysulfone hollowfiber PPM with an inner diameter of approximately 1 mm. It is evident from Figure 2.12 that these PPMs exhibit non-uniform pore geometries and a broad pore size distribution. The difference in their structure is mainly caused by the different fabrication methods employed. Celgard (Figure 2.12A), for example, is made by stretching. Acurell (Figure 2.12B) is fabricated using the phase-separation technology, while the hollow fiber (Figure 2.12 C and D) is produced by solution casting.

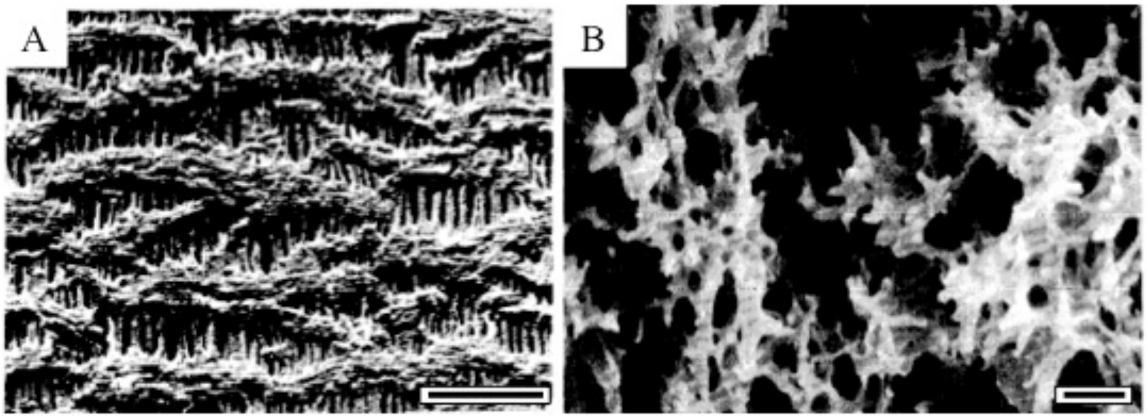

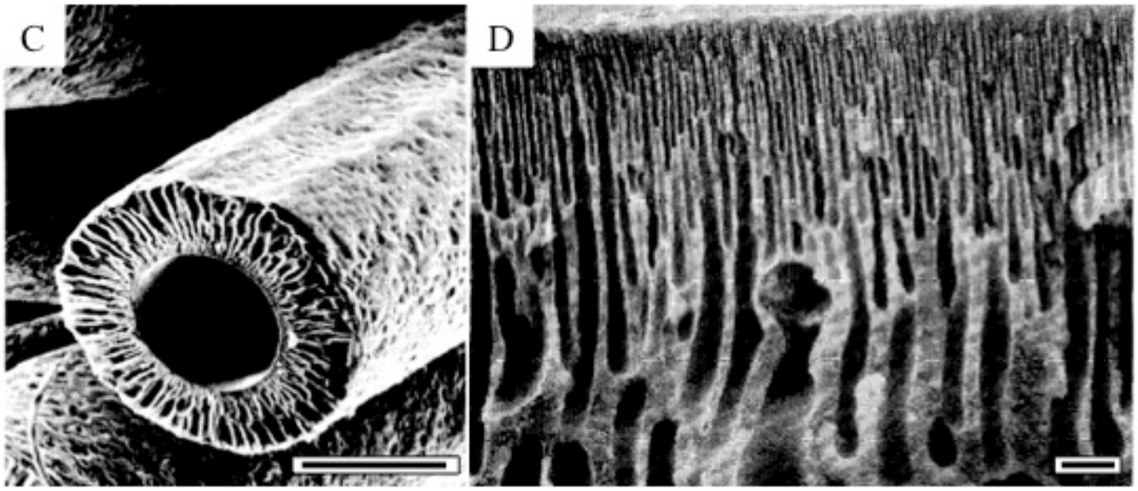

Figure 2.12 Various types of porous materials. (A) Micrograph of Celgard mesoporous polypropylene PPM. Scale bar 500 nm. (B) Micrograph of Accurel macroporous polypropylene PPM with rated pore of 200 nm. Scale bar 5 µm. (C) and (D) Large-scale and zoomed-in micrographs of mesoporous polysulfone hollowfiber PPM with a diameter of ~ 1mm, respectively. Scale bar 500 and 50 µm, respectively. [56]

Until recently, the majority of techniques used for the fabrication of PPMs involved either physical or mechanical methods with the most frequently utilized techniques being solution casting, stretching, chemical/track-etching, phase separation, and micro-fabrication.[61, 65, 76] More recently, chemical approaches have been explored as nanoscale pore features have gained importance.[34] Table 2.3 lists the fabrication methods together with the types of polymers and their applications.[55, 56, 58, 61, 76]

Table 2.3 Fabrication methods for PPMs and selected polymeric materials with corresponding applications. (a) RO=Reverse osmosis UF=Ultrafiltration GS=Gas separation MF=Microfiltration

Fabrication Method	Polymeric Material	Major Application[a]
Solution Casting	Cellulose Acetate/Polysulfone	RO, UF/GS
Chemical/Track Etching	Polycarbonate	MF
Stretching	Polytetrafluoroethylene	UF/MF
Phase Separation	Polyacrylonitrile	UF
Microfabrication	Silicon Nitride	MF

Solution Casting

Originally developed by Zsigmondy[77], the solution casting method was adopted and further improved by researchers at General Electric (Figure 2.13).[56] In solution casting, a PPM is fabricated by casting of a liquid polymer solution onto a planar base surface. Subsequently, the liquid solution is gelled slowly by exposing it to humid air to form a film. As more absorption of water from the atmosphere occurs, the film transitions itself to a hardened PPM.[56] PPMs fabricated using the solution casting method possess an uneven pore architecture because of the non-uniform absorption of water from the atmosphere. Alteration of the composition of the casting solution and the gelation conditions are found to improve the pore architecture.[55, 56] However, PPMs from solution casting always possess a smaller pore configuration at the air-polymer interface compared to the polymer-base interface. Differences in pore size distributions of up to 100 times are commonly observed.[55]

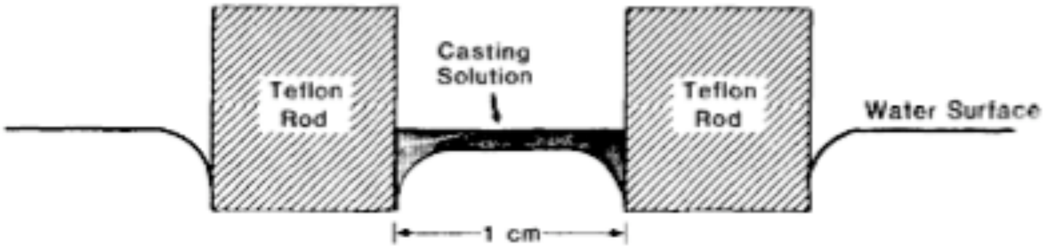

Figure 2.13 Sketch of solution casting technique developed by General Electric Co. applied for casting of ultrathin films of polycarbonate. [56]

Chemical/Track-Etching

In chemical/track-etching,[78, 79] the PPM is made by exposing a thin polymer film to a field of α-particles followed by exposure of the material to chemical etching to produce straight-bore through circular pores. Etching has been found to enable better control of the pore size than solution casting with a disadvantage of much lower porosity.[80] Figure 2.14A illustrates the fabrication of track-etched PPMs, while Figure 2.14B shows an SEM image of a polycarbonate membrane with 400 nm pores. Although the pore sizes are better controlled in comparison to solution casting, a very irregular distribution of pores is observed.

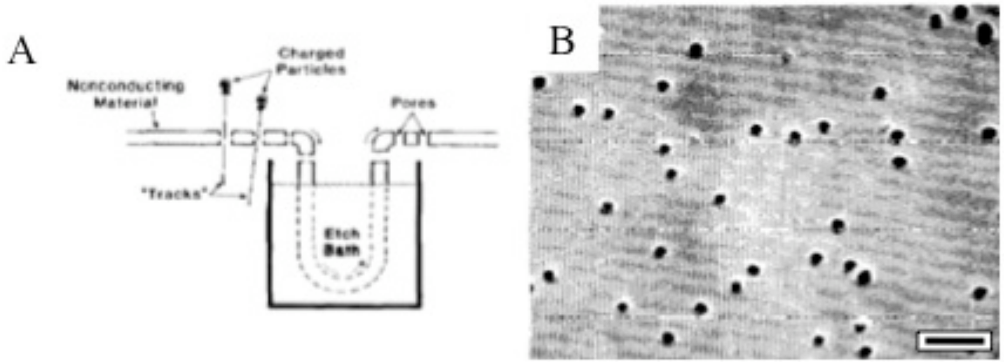

Figure 2.14 Porous materials obtained through etching technique. (A) Flow chart for track/chemical etching. (B) Nucleopore Polycarbonate PPM with a rated pore size of 400 nm.[56]

Similar to the etching technique, microfabrication techniques such as photo, ion and electron beam lithography are employed to achieve regular pore structures in PPMs through an etching-like process.[55] Many of the PPMs fabricated by lithographic techniques are mainly synthesized using silicon-based polymers with thicknesses of approximately 1 to 5 μm and pore sizes ranging from 100 nm to 4 μm.[81] However, these techniques pose problems, such as slow linear processing, pore blocking, and low pore density with the limitation of only fabricating 2D materials.[35, 81]

Stretching

Stretching techniques involve mechanical stretching of a polymeric material to increases its intrinsic porosity. Industrial stretching utilizes consecutive steps of cold stretching and hot stretching followed by heat setting.[82] Performing these steps results in permanent high-aspect ratio micro-tears in the polymeric material with reasonable pore uniformity.[56] With polypropylene, for example, pore sizes in the range of 20 nm and smaller can be achieved, which yields a PPM with high permeability for gases and vapors.[56] Figure 2.12A shows the micrograph of a stretched PPM fabricated from polypropylene (Celgard) by Celanase.[56] Another well-known example of a stretched PPM is Gore-Tex. Gore-Tex is an expanded polytetrafluoroethylene (PTFE) that has been stretched both uniaxially and biaxially yielding an intricate network of pores with diameters ranging from 20 nm to 10 μm as shown in the SEM image in Figure 2.15.[83, 84] In Gore's patents,[83, 84] the wide range of pores and the porosity are shown to be directly related to the strength of the PTFE PPM as well as the increased susceptibility towards impregnation with fillers and surface activators.

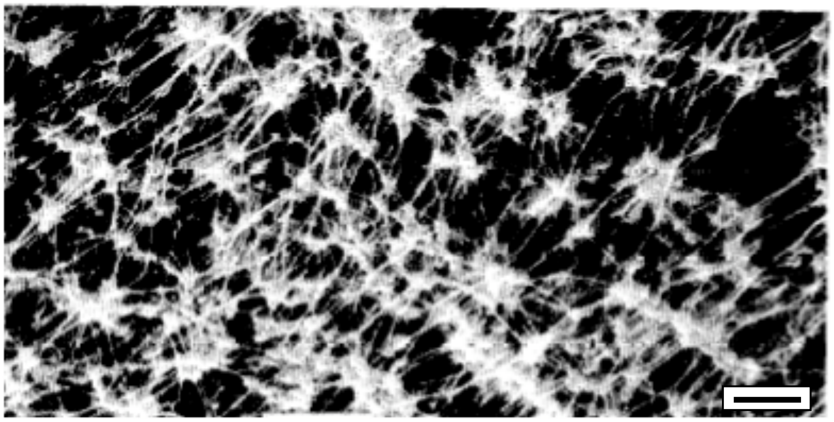

Figure 2.15. Stretched PTFE with pores ranging 20 nm up to 10,000 nm. Scale bar 50 μm.[56]

Phase Separation

The phase-separation (PS) method recently reviewed by van de Witte is both a chemical and physical synthesis technique to fabricate PPMs.[85] In PS, the separation of polymer solutions into two phases of different concentrations are used to control the pore size. The solidification of the phase with the higher polymer concentration after phase separation yields a porous network. Depending on which desolvation mechanism is involved, four phase separation techniques are distinguished: (i) precipitation in a non-solvent – *non-solvent induced* (*NIPS*), (ii) solvent evaporation – *evaporation induced* (*EIPS*), (iii) precipitation by absorption of non-solvent from the vapor phase – *vapor induced* (*VIPS*), and (iv) precipitation by cooling – *thermally induced* (*TIPS*).[55, 56, 85]

NIPS is utilized in fabricating PPMs in the non-porous to microporous regime. EIPS, VIPS, and TIPS are used in fabricating PPMs in the micro- to macroporous regime.

Biodegradable PPMs

Biodegradable PPMs are a relatively new group of porous polymeric materials that have been developed specifically for the field of tissue engineering.[53, 54, 86, 87] Tighter requirements with respect to bio-compatibility, control of pore size, and high porosity limit the type of polymers and methods available for the fabrication of biodegradable PPMs.[66-68] Additional properties such as *elasticity, directionality, and mechanical/physical properties* may further limit the range of usable polymers.[67] Table 2.4 summarizes several polymer precursors for biodegradable PPMs, the methods utilized in the fabrication of the PPMs employing these polymers, the pore-size range obtained, and the corresponding porosity. Fabrication techniques, such as freeze-drying, salt-leaching and electrospinning, have been thoroughly reviewed and studied by Peppas,[86, 88] Mooney,[87, 89] and Langer.[53, 54, 90]

Table 2.4 Precursors, fabrication techniques, and properties of biodegradable PPMs.[66, 91]

Biocompatible Material	**Fab. Technique**	**Pore Size (μm)**	**Porosity (%)**
Collagen	Freeze-drying	10 – 135	> 70
Hyaluronic Acid	Salt-leaching	100 – 600	80 – 90
Poly(lactide)	Salt-leaching	~600	> 60
Poly(lactide-*co*-glycolide)	Sintering/Electrospinng	~70 – 210	30 – 60
Poly(propylene fumarate)	Salt-leaching	70 – 800	51 – 97

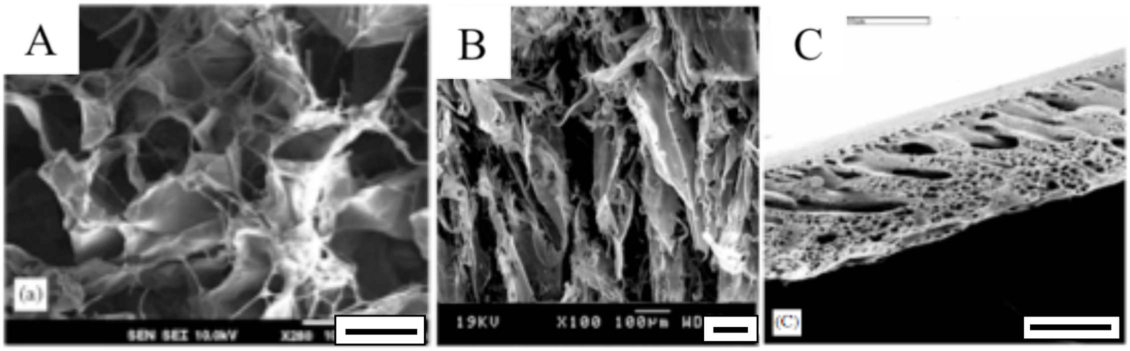

Figure 2.16 Scanning electron microscope images of biodegradable PPMs. (A) Collagen-based PPM obtained with freeze-drying technique.[92] Scale bar 100 µm. (B) Poly(D,L-lactide)-based PPM obtained using freeze-drying.[93] Scale bar 100 µm. (C) Poly(lactide-*co*-glycolide)-based PPM obtained via phase-separation.[54] Scale bar 100 µm.

Figure 2.16 depicts three biodegradable polymers; collagen, poly(D,L-lactide), and poly(lactide-*co*-glycolide). As is evident from Figure 2.16, random pore architectures are observed in biodegradable PPMs as well. The random pore structures result from different techniques employed in each respective fabrication process. Both PPMs depicted in Figures 2.16 A and B are synthesized by the freeze-drying or lyophilization technique. The technique involves dehydration of frozen raw material solution followed by sublimation of the solvent at a reduced surrounding pressure. A large variation of pore sizes is observed due to the limited control of the process.[92,93] The variation in pore size in Figure 2.16C is caused by the phase separation technique, where tight control of pore size and the porosity have shown to be difficult.[54]

2.2.2 Colloid-Templated Porous Polymeric Materials

Nano- and micro-colloidal templating have received special attention as techniques that allow the control of pore size and porosity as well as the miniaturization of membrane manufacturing processes driven by recent research in modern membrane technology.[2, 6, 55, 94] Especially, the fact that the pore size can be changed independently of the porosity by controlling particle size and particle packing separately has caught the imagination of many researchers. Xia et al.,[95] showed that tailored surface structures are generated when various colloidal particle sizes and domains with different packing are employed. Figure 2.17 shows 2D and 3D colloidal assemblies obtained from colloids with varying sizes that have been used as templates for porous polymeric materials.[6]

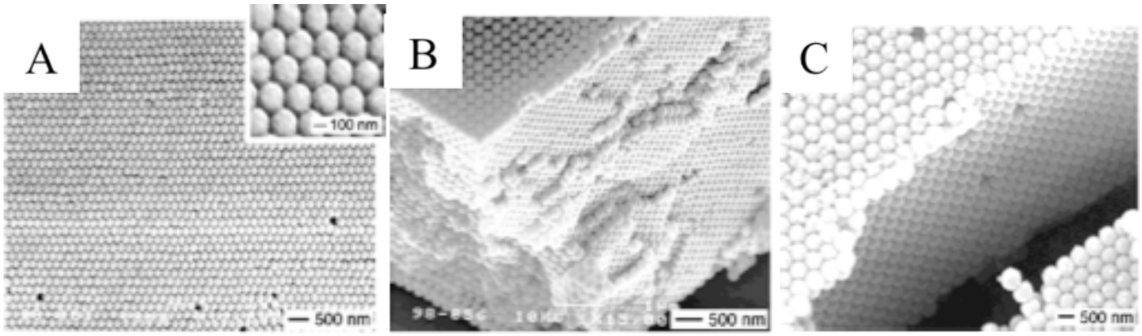

Figure 2.17 SEM images of colloidal assemblies.[6] (A) 2D 280 nm Polysytrene (PS) colloidal assembly (B) Cross-sectional image of 3D 280 nm PS assembly. (C) Cross-sectional image of 3D 400 nm PS assembly.

Figure 2.18 shows an example of porous structures fabricated using colloidal assemblies like those shown in Figure 2.17.

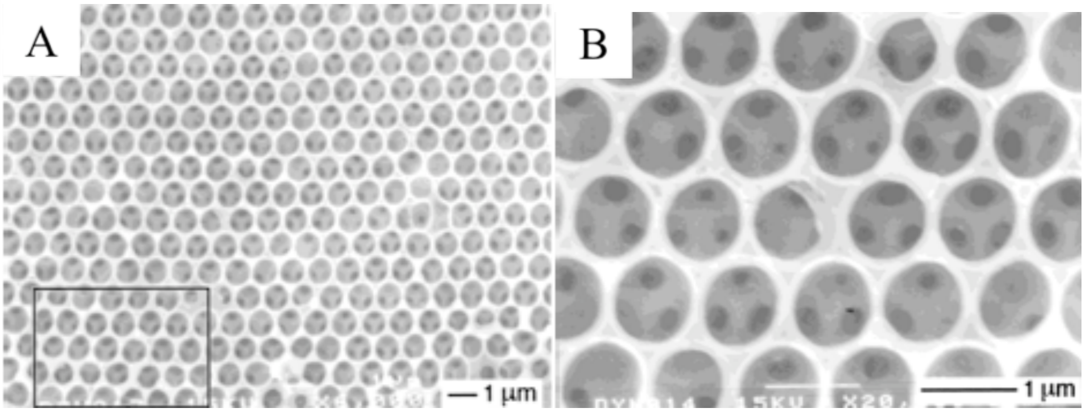

Figure 2.18 SEM images of highly ordered porous structures obtained with colloidal templating.[95] (A) PPM fabricated using 1 µm silica colloids with poly(acrylate-methacrylate) copolymer as backbone. (B) rectangular inset of image (a) showing a sub-layer porous structure.

After the colloidal templates have been formed, a polymeric precursor is allowed to infiltrate the interstitial voids formed by the colloidal particles employing the Laplace flow described earlier. Once the precursor is cured by means of polymerization through an appropriate agent, i.e. UV light, heat, or other activators, the colloids entrapped within the polymer matrix can be removed by different methods. A variety of backbone materials and the appropriate method for the removal of the templating colloids are given in Table 2.5.[10]

Table 2.5 Polymeric precursors used to fabricate PPMs and their corresponding templating materials as well as the removal methods.[10]

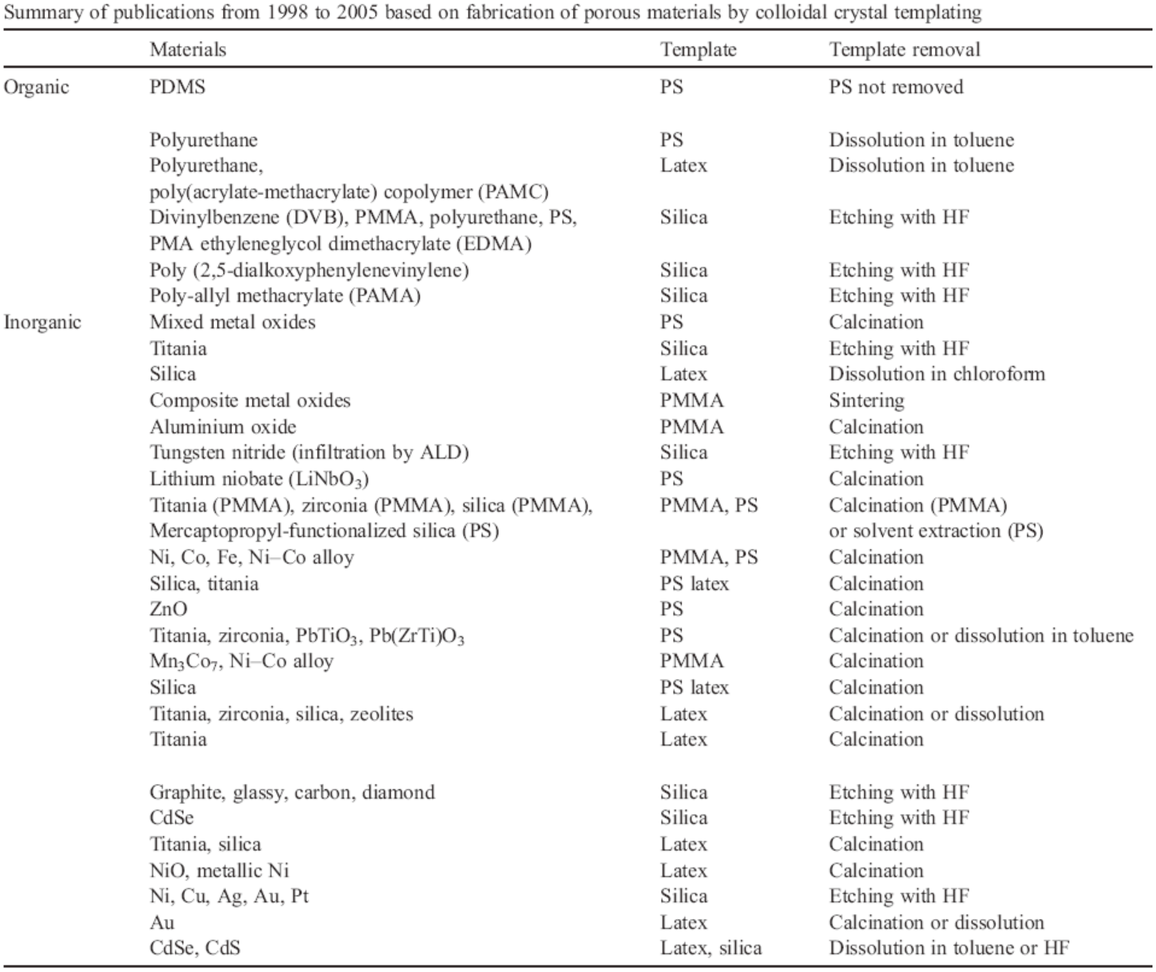

Summary of publications from 1998 to 2005 based on fabrication of porous materials by colloidal crystal templating

	Materials	Template	Template removal
Organic	PDMS	PS	PS not removed
	Polyurethane	PS	Dissolution in toluene
	Polyurethane, poly(acrylate-methacrylate) copolymer (PAMC)	Latex	Dissolution in toluene
	Divinylbenzene (DVB), PMMA, polyurethane, PS, PMA ethyleneglycol dimethacrylate (EDMA)	Silica	Etching with HF
	Poly (2,5-dialkoxyphenylenevinylene)	Silica	Etching with HF
	Poly-allyl methacrylate (PAMA)	Silica	Etching with HF
Inorganic	Mixed metal oxides	PS	Calcination
	Titania	Silica	Etching with HF
	Silica	Latex	Dissolution in chloroform
	Composite metal oxides	PMMA	Sintering
	Aluminium oxide	PMMA	Calcination
	Tungsten nitride (infiltration by ALD)	Silica	Etching with HF
	Lithium niobate ($LiNbO_3$)	PS	Calcination
	Titania (PMMA), zirconia (PMMA), silica (PMMA), Mercaptopropyl-functionalized silica (PS)	PMMA, PS	Calcination (PMMA) or solvent extraction (PS)
	Ni, Co, Fe, Ni–Co alloy	PMMA, PS	Calcination
	Silica, titania	PS latex	Calcination
	ZnO	PS	Calcination
	Titania, zirconia, $PbTiO_3$, $Pb(ZrTi)O_3$	PS	Calcination or dissolution in toluene
	Mn_3Co_7, Ni–Co alloy	PMMA	Calcination
	Silica	PS latex	Calcination
	Titania, zirconia, silica, zeolites	Latex	Calcination or dissolution
	Titania	Latex	Calcination
	Graphite, glassy, carbon, diamond	Silica	Etching with HF
	CdSe	Silica	Etching with HF
	Titania, silica	Latex	Calcination
	NiO, metallic Ni	Latex	Calcination
	Ni, Cu, Ag, Au, Pt	Silica	Etching with HF
	Au	Latex	Calcination or dissolution
	CdSe, CdS	Latex, silica	Dissolution in toluene or HF

Depending on the backbone material and the colloid material used different removal techniques must be employed. Colloids based on silica must be etching by hydrofluoric acid, which presents a significant health hazards, whereas polymeric colloids can be removed by dissolution or calcinations methods. Calcination is a process that uses heat to burn off polymeric colloidal material. The dissolution method dissolves the targeted templating polymeric colloidal particles. A list of polymers and their respective solvents is given in Table 2.6.

Table 2.6 List of polymers and respective solvents that dissolve the polymers.[96, 97]

Polymers	Solvents that dissolve the listed polymer
Polystyrene	THF
Polycarbonate	THF
Polymethacrylates	Acetonitrile
Polypropylene	o-dichlorobenzene
Polyacrylonitrile	N,N-dimethylformamide
Polyolefines	Xyleen
Polyester	N-methyl-2-pyrolidinon
Polyacrlyic acid	Water
Polyvinylalcohol	Water

The porous structure left behind by the colloids will have porosities in the range of 55% to 64%. In addition, it is important to recognize the ordered structure of the pores as well as the presence of *inter-connecting* pores formed by the colloidal contacts within the polymer matrix.[70] The inter-connected pore structure arises from the partial wetting of the polymeric monomer at the contact points between colloids. Colvin et. al.[70] have indicated that the polymeric precursor viscosity and polymer shrinkage are two key factors controlling the shape and the size of the inter-connecting pores. High-viscosity precursors are limited in the ability to penetrate into the interstitial voids due to both wetting and capillary phenomena.[70] Therefore, more viscous precursors will lead to larger interconnecting pores as shown in Figure 2.19. In addition to the viscosity, polymer volume shrinkage is also involved in the pore structure formation.[98]

Porous structures like those shown in Figure 2.19 have been found to possess novel and unique properties that are neither found in bulk materials nor in the molecular precursor used for the backbone.[99] Some of these novel properties are tunable optical properties[6] and alterable surface properties. In addition, utilizing nano- and micro-scale colloids reduces the manufacturing costs. The PPMs based on colloidal templating with smaller and significantly finer domains exhibit higher efficiency and can be applied in catalytic membrane separation, biotechnology, and semiconductor industry.

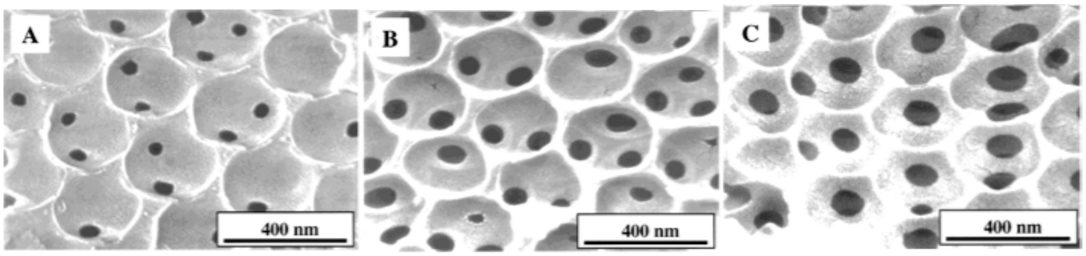

Figure 2.19 Polyurethane PPM structures templated with 353 nm silica colloids and polymers of increasing viscosity leading to pore diameters ranging from (A) 60 nm to (C) 118 nm.[70]

2.2.3 Pore Sizes and Porosity Characterization

Porosity and permeability are essential parameters in defining the applicability of a porous polymeric material. Both parameters are determined by the *average pore size*, *pore size distribution*, and *void spaces* of a PPM. Several methods have been developed for the measurement of porosity and permeability of porous materials.[100, 101] One of the techniques utilized to measure the PPM pore characteristic is microscopic analysis.

The most straightforward method to investigate the morphology of a PPM is to visualize its nanoscopic or microsocpic structure with a microscope. The rapid development of optical, fluorescence, electron, and scanning probe/tunneling microscopes has lead to enthralling observations.[100, 102, 103] Microscope images or micrographs offer direct visual information regarding the surface pore shape, surface porosity, cross-sectional features, and in some cases even allow 3-D image analysis.[100, 104] Going from large micrometer to nanometer pores, *Scanning and Transmission Electron*

Microscopes (EM), Confocal Microscopes (CM), and *Atomic Force Microscopes (AFM)* are the tools of choice for determining the morphology of PPMs.

With the implementation of Field Emission Guns in EM, the resolution capability has improved drastically such that even pore structures of sub-nanometer size can be detected.[100] Manabe et al.,[105, 106] have developed a technique where the pore radius distribution *N(r)*, determined from the probability of pores to be on the cut-off line, is related to the distribution function *F(x)* of the length x of pores on the cut-off line on a micrograph. In order to obtain the distribution function *F(x)*, a micrograph of a cross section parallel to the membrane surface, Figure 2.20B, is used. Evenly scaled cut-off lines are drawn parallel to each other on the micrograph, where the cut-off length of each pore, x_i, and the pore intervals, Δx, are determined. Pore intervals are classified into the number of data F[x] by different interval length ranges such as 0 to Δx, Δx to $2\Delta x$, and so on. From the number of data F[x], the distribution function *F(x)* is determined by Equation 2.21.

$$F(x) = \frac{F[x]}{\Delta x} \tag{2.21}$$

Assuming ellipsoidal pores, the pore radius distribution $N_e(r)$ is determined using Equation 2.22, where Φ_e is the shape factor.

$$N_e(r) = -\frac{4}{\pi\Phi_e}\frac{d(F(x)/x)}{dx} \qquad ellipsoidal \tag{2.22}$$

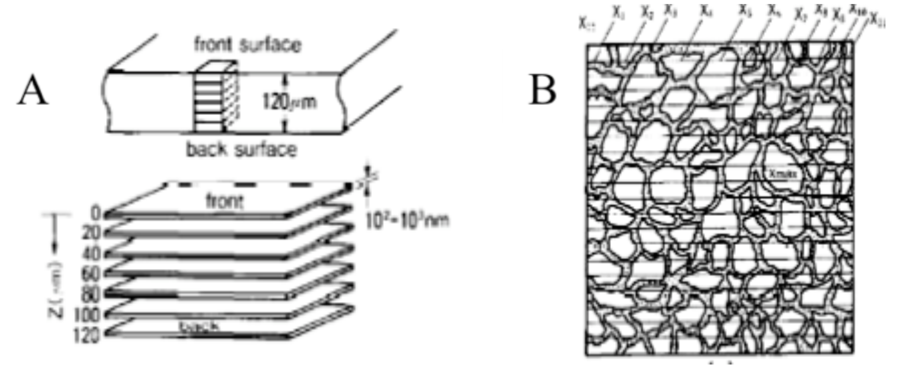

Figure 2.20 Schematic depiction of porosity determination through microscopy.[105, 106] (A) Slicing of a resin-embedded PPM. (B) Microscope images of complex PPM fabricated by phase-separation method with cut-off lines.

From the pore radius distribution $N_e(r)$, the porosity $P_e r$ and pore density N are obtained using Equation 2.23.

$$\begin{aligned} P_e r &= \pi \int r^2 N_e(r) dr \\ N &= \int N_e(r) dr \end{aligned} \tag{2.23}$$

The resulting correlation images provide useful morphological information, but cannot accurately model the actual morphology. Zeman and Denault[107, 108] devised software that enables quantitative analysis of a digitized EM micrograph. The analysis algorithm is based on color (black and white) differentiation. A digitized micrograph of 256 x 256 pixels is scanned pixel by pixel and the level of darkness is determined digitally. The precise position of the pores is determined using the darkness level, while the pore positions are used to determine the pore sizes and the porosity of the PPM. Figure 2.21 shows an example of such a black and white EM graph and the frequency of grey level changes on the micrograph.

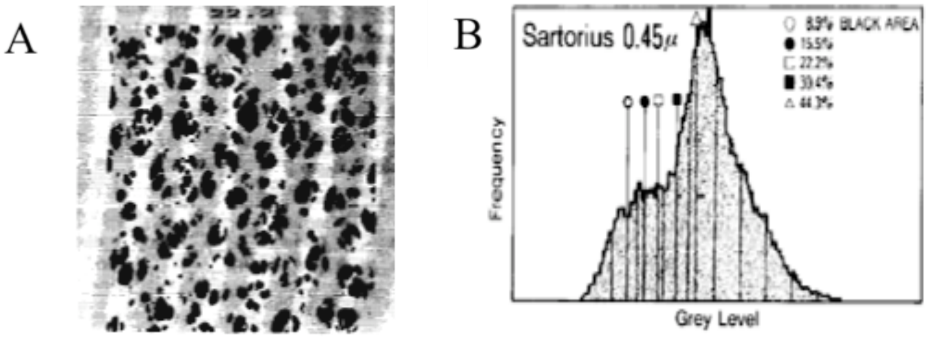

Figure 2.21 (A) Binary EM microscope images of Sartorius SM 11106 PPM. (B) A typical darkness level change and the apparent frequency of grey level changes from the micrograph.[107, 108]

Despite the fact that the analysis of EM micrographs is a widely accepted and used tool for determining the morphology of PPMs, there are several downsides to this technique. For example, sample charging, e^- beam irradiation, and high vacuum can affect the material and lead to faulty analysis. CM and AFM are more flexible with respect to sample properties, preparation, and pore detection. Specific techniques used to image porous polymeric materials utilizing CM and AFM have been reviewed by several research groups.[102, 104, 109-113] Examplary 3D AFM scans of a co-block polymer in Phase Contrast Mode and Lateral Force Mode are depicted in Figures 2.22 A and B, respectively.

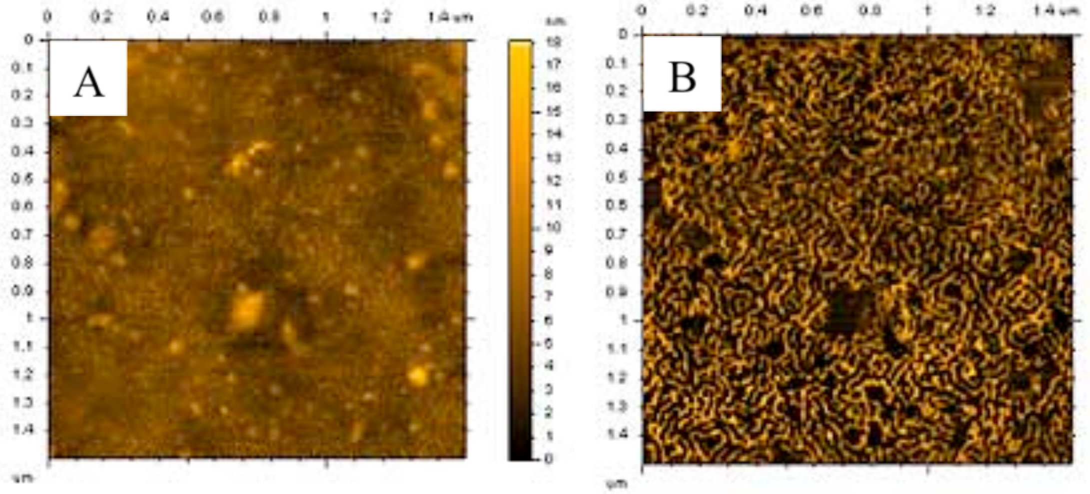

Figure 2.22 3D image of co-block polymer scanned using an AFM.[75, 104, 114] **(A) Phase contrast mode. (B) Lateral force mode. Porous morphology on a sub-micron length scale is observed.**

2.3 Summary

Templated-assisted materials engineering (TAME) has shown to be an effective tool to fabricate novel, tailorable, controlled, and efficient functional 3D materials. From colloidal assembly to porous material fabrication, TAME can be applied to obtain desired materials with defined characteristics. Further, utilizing TAME in colloidal templating in a geometrical confinement offers a method to fabricate 3D porous polymeric materials with directionality that may be applied in a number of applications.

REFERENCES:

1. Velev, O. D.; Lenhoff, A. M.; Kaler, E. W. *Science* **2000,** *287*, 2240-2243.

2. Velev, O. D.; Lenhoff, A. M. *Current Opinion in Colloid & Interface Science* **2000,** *5*, 56-63.

3. Clark, T. D.; Ferrigno, R.; Tien, J.; Paul, K. E.; Whitesides, G. M. *Journal of the American Chemical Society* **2002,** *124*, 5419-5426.

4. Grzybowski, B. A.; Wilmer, C. E.; Kim, J.; Browne, K. P.; Bishop, K. J. M. *Soft Matter* **2009,** *5*, 1110-1128.

5. Dziomkina, N. V.; Vancso, G. J. *Soft Matter* **2005,** *1*, 265-279.

6. Xia, Y. N.; Gates, B.; Yin, Y. D.; Lu, Y. *Advanced Materials* **2000,** *12*, 693-713.

7. Yan, F.; Goedel, W. A. *Advanced Materials* **2004,** *16*, 911-915.

8. Liu, Y. F.; Wang, S. P.; Lee, J. W.; Kotov, N. A. *Chemistry of Materials* **2005,** *17*, 4918-4924.

9. Kotov, N. A.; Liu, Y. F.; Wang, S. P.; Cumming, C.; Eghtedari, M.; Vargas, G.; Motamedi, M.; Nichols, J.; Cortiella, J. *Langmuir* **2004,** *20*, 7887-7892.

10. Hoa, M. L. K.; Lu, M. H.; Zhang, Y. *Advances in Colloid and Interface Science* **2006,** *121*, 9-23.

11. Chung, Y. W.; Leu, I. C.; Lee, J. H.; Hon, M. H. *Langmuir* **2006,** *22*, 6454-6460.

12. Im, S. H.; Lim, Y. T.; Suh, D. J.; Park, O. O. *Advanced Materials* **2002,** *14*, 1367-1369.

13. Kim, M. H.; Im, S. H.; Park, O. O. *Advanced Functional Materials* **2005,** *15*, 1329-1335.

14. Im, S. H.; Park, O. O. *Langmuir* **2002,** *18*, 9642-9646.

15. Zeng, F.; Sun, Z. W.; Wang, C. Y.; Ren, B. Y.; Liu, X. X.; Tong, Z. *Langmuir* **2002,** *18*, 9116-9120.

16. Chung, Y. W.; Leu, I. C.; Lee, J. H.; Hon, M. H. *Applied Physics a-Materials Science & Processing* **2004,** *79*, 2089-2092.

17. Kralchevsky, P. A.; Denkov, N. D. *Current Opinion in Colloid & Interface Science* **2001,** *6*, 383-401.

18. Dimitrov, A. S.; Nagayama, K. *Langmuir* **1996,** *12*, 1303-1311.

19. Kralchevsky, P. A.; Nagayama, K. *Langmuir* **1994,** *10*, 23-36.

20. Paunov, V. N.; Kralchevsky, P. A.; Denkov, N. D.; Nagayama, K. *Journal of Colloid and Interface Science* **1993,** *157*, 100-112.

21. Kim, B. M.; Qian, S.; Bau, H. H. *Nano Letters* **2005,** *5*, 873-878.

22. Paunov, V. N. *Langmuir* **1998,** *14*, 5088-5097.

23. Rycenga, M.; Camargo, P. H. C.; Xia, Y. N. *Soft Matter* **2009,** *5*, 1129-1136.

24. Wu, H. K.; Thalladi, V. R.; Whitesides, S.; Whitesides, G. M. *Journal of the American Chemical Society* **2002,** *124*, 14495-14502.

25. Velev, O. D.; Jede, T. A.; Lobo, R. F.; Lenhoff, A. M. *Chemistry of Materials* **1998,** *10*, 3597-3602.

26. Wang, D. Y.; Mohwald, H. *Journal of Materials Chemistry* **2004,** *14*, 459-468.

27. Miguez, H.; Yang, S. M.; Ozin, G. A. *Langmuir* **2003,** *19*, 3479-3485.

28. Miguez, H.; Yang, S. M.; Ozin, G. A. *Applied Physics Letters* **2002,** *81*, 2493-2495.

29. Yi, G. R.; Moon, J. H.; Yang, S. M. *Advanced Materials* **2001,** *13*, 1185-1188.

30. Ye, J. H.; Zentel, R.; Arpiainen, S.; Ahopelto, J.; Jonsson, F.; Romanov, S. G.; Torres, C. M. S. *Langmuir* **2006,** *22*, 7378-7383.

31. Xia, D. Y.; Li, D.; Luo, Y.; Brueck, S. R. J. *Advanced Materials* **2006,** *18*, 930-933.

32. Yang, P. D.; Deng, T.; Zhao, D. Y.; Feng, P. Y.; Pine, D.; Chmelka, B. F.; Whitesides, G. M.; Stucky, G. D. *Science* **1998,** *282*, 2244-2246.

33. Park, S. H.; Xia, Y. N. *Langmuir* **1999,** *15*, 266-273.

34. Stein, A.; Schroden, R. C. *Current Opinion in Solid State & Materials Science* **2001,** *5*, 553-564.

35. Moon, J. H.; Kim, S.; Yi, G. R.; Lee, Y. H.; Yang, S. M. *Langmuir* **2004,** *20*, 2033-2035.

36. Morrison, I.; Ross, S., *Colloidal Dispersion*. John Wiley and Sons Inc.: New York 2002.

37. Hiemenz, P.; Rajagopalan, R., *Principles of Colloid and Surface Chemistry*. 3rd ed.; Marcel Dekker: New York, 1997; p 650.

38. Kim, E.; Xia, Y. N.; Whitesides, G. M. *Journal of the American Chemical Society* **1996,** *118*, 5722-5731.

39. Kim, E.; Xia, Y. N.; Whitesides, G. M. *Advanced Materials* **1996,** *8*, 245-247.

40. Kim, B. M.; Sinha, S.; Bau, H. H. *Nano Letters* **2004,** *4*, 2203-2208.

41. Burger, R.; Fjelde, K. K.; Hofler, K.; Karlsen, K. H. *Journal of Engineering Mathematics* **2001,** *41*, 167-187.

42. Li, F.; He, J. B.; Zhou, W. L. L.; Wiley, J. B. *Journal of the American Chemical Society* **2003,** *125*, 16166-16167.

43. Ehlert, S.; Roesler, T.; Tallarek, U. *Journal of Separation Science* **2008,** *31*, 1719-1728.

44. Muller, C. R.; Holland, D. J.; Sederman, A. J.; Mantle, M. D.; Gladden, L. F.; Davidson, J. F. In *Magnetic Resonance Imaging of fluidized beds*, 2008; pp 53-62.

45. Baldwin, C. A.; Sederman, A. J.; Mantle, M. D.; Alexander, P.; Gladden, L. F. *Journal of Colloid and Interface Science* **1996,** *181*, 79-92.

46. Sederman, A. J.; Alexander, P.; Gladden, L. F. *Powder Technology* **2001,** *117*, 255-269.

47. Harris, W. F.; Erickson, R. O. *Journal of Theoretical Biology* **1980,** *83*, 215-246.

48. Erickson, R. O. *Science* **1973,** *181*, 705-716.

49. Pickett, G. T.; Gross, M.; Okuyama, H. *Physical Review Letters* **2000,** *85*, 3652-3655.

50. Mueller, G. E. *Powder Technology* **2005,** *159*, 105-110.

51. Hsieh, S. C.; Jorgenson, J. W. *Analytical Chemistry* **1996,** *68*, 1212-1217.

52. Jung, S.; Ehlert, S.; Mora, J. A.; Kraiczek, K.; Dittmann, M.; Rozing, G. P.; Tallarek, U. *Journal of Chromatography A* **2009,** *1216*, 264-273.

53. Levenberg, S.; Langer, R., *Current Topics in Developmental Biology* **2004**, *61*, 113-134.

54. Langer, R.; Tirrell, D. A. *Nature* **2004,** *428*, 487-492.

55. Ulbricht, M. *Polymer* **2006,** *47*, 2217-2262.

56. Lonsdale, H. K. *Journal of Membrane Science* **1982,** *10*, 81-181.

57. Dixon, A. G. *Int. J. Chem. Reactor Eng.* **2003,** *1*, 1-35.

58. Ozdemir, S. S.; Buonomenna, M. G.; Drioli, E. *Applied Catalysis a-General* **2006,** *307*, 167-183.

59. Vankelecom, I. F. J. *Chemical Reviews* **2002,** *102*, 3779-3810.

60. Capes, J. S.; Ando, H. Y.; Cameron, R. E. *Journal of Materials Science-Materials in Medicine* **2005,** *16*, 1069-1075.

61. Pandey, P.; Chauhan, R. S. *Progress in Polymer Science* **2001,** *26*, 853-893.

62. Sirkar, K.; Lloyd, D., *New Membrane Materials and Processes for Separation*. American Institute of Chemical Engineers: New York, 1988; Vol. 84.

63. Kesting, R., *Synthetic Polymeric Membranes*. John Wiley & Sons, Inc.: New York, 1985.

64. Lloyd, D., *Materials Science of Synthetic Membrane*. American Chemical Society: Washington D.D., 1985.

65. de Jong, J.; Lammertink, R. G. H.; Wessling, M. *Lab on a Chip* **2006,** *6*, 1125-1139.

66. Karageorgiou, V.; Kaplan, D. *Biomaterials* **2005,** *26*, 5474-5491.

67. Park, J.; Bronzion, J., *Biomaterials - Principles and Applications*. CRC Press: Boca Raton, 2003.

68. Vieth, W. R., *Membrane Systems: Analysis and Design*. Oxford University Press: Munich, 1988.

69. Dokko, K.; Akutagawa, N.; Isshiki, Y.; Hoshina, K.; Kanamura, K. *Solid State Ionics* **2005,** *176*, 2345-2348.

70. Jiang, P.; Hwang, K. S.; Mittleman, D. M.; Bertone, J. F.; Colvin, V. L. *Journal of the American Chemical Society* **1999,** *121*, 11630-11637.

71. Imhof, A.; Pine, D. J. *Advanced Materials* **1998,** *10*, 697-700.

72. Imhof, A.; Pine, D. J. *Nature* **1997,** *389*, 948-951.

73. George, S. C.; Thomas, S. *Progress in Polymer Science* **2001,** *26*, 985-1017.

74. Cui, J. Q.; Kretzschmar, I. *Langmuir* **2006,** *22*, 8281-8284.

75. Koros, W. J.; Fleming, G. K. *Journal of Membrane Science* **1993,** *83*, 1-80.

76. Chung, T. S. *Polymers & Polymer Composites* **1996,** *4*, 269-283.

77. Zsigmondy, R. Filter And Method of Producing Same. 1421341, 1922.

78. Fleische.Rl; Alter, H. W.; Walker, R. M.; Furman, S. C.; Price, P. B. *Science* **1972,** *178*, 255-263.

79. Fleische.Rl; Price, P. B.; Walker, R. M. *Scientific American* **1969,** *220*, 30-39.

80. Price, P. B. Molecular Sieves and Methods For Producing Same. 3303085, Feb. 7, 1967, 1962.

81. Kuiper, S.; van Rijn, C. J. M.; Nijdam, W.; Elwenspoek, M. C. *Journal of Membrane Science* **1998,** *150*, 1-8.

82. M. Druin, J. L., S. Plovan Novel Open-Celled Microporus Film. 3801404, 1972.

83. Gore, R. Process for producing porous products. 3953566, 1976.

84. Gore, R. Very highly stretched polytetrafluoroethylene and process therefor. 3962153, June 8, 1976, 1976.

85. vandeWitte, P.; Dijkstra, P. J.; vandenBerg, J. W. A.; Feijen, J. *Journal of Membrane Science* **1996,** *117*, 1-31.

86. Peppas, N. A.; Hilt, J. Z.; Khademhosseini, A.; Langer, R. *Advanced Materials* **2006,** *18*, 1345-1360.

87. Lee, K. Y.; Mooney, D. J. *Chemical Reviews* **2001,** *101*, 1869-1879.

88. Peppas, N. A.; Huang, Y. *Pharmaceutical Research* **2002,** *19*, 578-587.

89. Drury, J. L.; Mooney, D. J. *Biomaterials* **2003,** *24*, 4337-4351.

90. Lavik, E. B.; Klassen, H.; Warfvinge, K.; Langer, R.; Young, M. J. *Biomaterials* **2005,** *26*, 3187-3196.

91. Stenzel, K. H.; Miyata, T.; Rubin, A. L. *Annual Review of Biophysics and Bioengineering* **1974,** *3*, 231-253.

92. Song, E.; Kim, S. Y.; Chun, T.; Byun, H. J.; Lee, Y. M. *Biomaterials* **2006,** *27*, 2951-2961.

93. Blacher, S.; Maquet, V.; Schils, F.; Martin, D.; Schoenen, J.; Moonen, G.; Jerome, R.; Pirard, J. P. *Biomaterials* **2003,** *24*, 1033-1040.

94. Soten, I.; Ozin, G. A. *Current Opinion in Colloid & Interface Science* **1999,** *4*, 325-337.

95. Gates, B.; Yin, Y. D.; Xia, Y. N. *Chemistry of Materials* **1999,** *11*, 2827-2836.

96. ChemWare, K., Polymer Analysis - Solubility and solvents for dissolution. In *http://home.planet.nl/~skok/database/solubility/*, Zeist, Netherlands, 2002.

97. Miller-Chou, B. A.; Koenig, J. L. *Progress in Polymer Science* **2003,** *28*, 1223-1270.

98. Mark, J., *Physical Properties of Polymers Handbook*. Woodbury, New York, 1996.

99. Murray, C. B.; Kagan, C. R.; Bawendi, M. G. *Annual Review of Materials Science* **2000,** *30*, 545-610.

100. Nakao, S. *Journal of Membrane Science* **1994,** *96*, 131-165.

101. Lin, Y. S.; Burggraaf, A. J. *Journal of the American Ceramic Society* **1991,** *74*, 219-224.

102. Dunn, B.; Zink, J. I. *Chemistry of Materials* **1997,** *9*, 2280-2291.

103. Kaneko, K. *Journal of Membrane Science* **1994,** *96*, 59-89.

104. Paredes, J. I.; Martinez-Alonso, A.; Tascon, J. M. D. *Microporous and Mesoporous Materials* **2003,** *65*, 93-126.

105. Manabe, S.; Shigemoto, Y.; Kamide, K. *Polymer Journal* **1985,** *17*, 775-785.

106. Manabe, S.; Kamata, Y.; Iijima, H.; Kamide, K. *Polymer Journal* **1987,** *19*, 391-404.

107. Zeman, L.; Denault, L. *Journal of Membrane Science* **1992,** *71*, 221-231.

108. Zeman, L. *Journal of Membrane Science* **1992,** *71*, 233-246.

109. Dietz, P.; Hansma, P. K.; Inacker, O.; Lehmann, H. D.; Herrmann, K. H. *Journal of Membrane Science* **1992,** *65*, 101-111.

110. Fritzsche, A. K.; Arevalo, A. R.; Moore, M. D.; Ohara, C. *Journal of Membrane Science* **1993,** *81*, 109-120.

111. Fritzsche, A. K.; Arevalo, A. R.; Moore, M. D.; Weber, C. J.; Elings, V. B.; Kjoller, K.; Wu, C. M. *Journal of Applied Polymer Science* **1992,** *46*, 167-178.

112. Fritzsche, A. K.; Arevalo, A. R.; Connolly, A. F.; Moore, M. D.; Elings, V.; Wu, C. M. *Journal of Applied Polymer Science* **1992,** *45*, 1945-1956.

113. Fritzsche, A. K.; Arevalo, A. R.; Moore, M. D.; Elings, V. B.; Kjoller, K.; Wu, C. M. *Journal of Membrane Science* **1992,** *68*, 65-78.

114. Nanotechnology, P., Polymer. In *Safari*, http://www.pacificnanotech.com/polymers_single.html, Ed. 2002-2006.

Chapter 3

Colloid-Templated Multi-sectional Porous Polymeric Fibers

In Chapter 3, the fabrication method for porous polymeric fibers (PPFs) is reported. In the first section, multi-sectional colloidal assemblies are fabricated in a microcapillary by alternating dips into colloidal solutions of varying size. Subsequently, infiltration with curable polymer and washing with suitable solvents results in porous fibers with a cylindrical cross section. Along the length of the fiber, alternating sections with controlled length of pores and pore size distributions exist. These fibers present interesting materials for neural scaffolding, catalysis, and possibly photonics, if produced with a high degree of crystallinity. The surface pores and bulk porosity of the fibers are characterized by variable pressure Scanning Electron Microscopy (vp-SEM). Careful analysis shows that the surface pores vary with the colloidal template diameter and polymer infiltration time.

3.1 Introduction

Ordered, three-dimensional porous polymeric materials (PPMs) have generated immense interest in recent years for their potential applications in membrane technology,[1] biological science,[2] catalysis,[3] and photonics.[4,5] PPMs with micro- and nano-scale pore sizes are effective and distinctive materials for optics, scaffolding, and separation because of their ordered structure and periodicity and their increased surface area-to-volume ratio. Various PPM fabrication methods such as biotemplating,[6] emulsion droplet templating,[7] and colloidal templating[8] have been explored.

Although two-dimensionally templated tunable PPMs have been fabricated,[9] three-dimensionally (3D) templated PPMs with controlled thickness and alternating pore structures have not been explored. 3D structures such as, for example, fibers with sections of controlled length and porosity could serve as interesting materials for designer photonic structures and neural scaffolding. Colloidal templating (CT) offers a promising approach for tuning the pore structure of PPMs. Colloid-templated PPMs have predefined spherical pores and a well-defined pore distribution, i.e., porosity, determined by the colloidal packing. In addition, CT offers alternative geometries such as rectangular, spherical, and cylindrical geometries that suit the needs of many applications.[10-15] The pore characteristics of PPMs fabricated using CT may be altered by the size and the packing order of the colloidal templates used.[4,8,16-18] CT is a powerful, yet inexpensive, and adaptable method for large-scale production of PPMs with a high degree of control over pore characteristics.[6]

3.2 Experimental Details

Materials. Sulfate-terminated polystyrene (PS) colloids with 8% (w/v) of 2.5 ± 0.1 and 4% (w/v) of 10 ± 0.7 μm diameter in aqueous form were purchased from Invitrogen. A polymethylmethacrylate (PMMA) capillary of 50 ± 2.5 μm diameter in a spool of 1 m was purchased from Paradigm Optics. (Heptadecafluoro-1,1,2,2-Tetra-Hydrodecyl) Trichlorosilane was purchased from Gelest. Chloroform was purchased from Fisher

Scientific. UV curable polyurethane liquid pre-polymer NOA 60 was purchased from Norland Optics. De-ionized (DI) water was obtained from a Millipore Milli-Q unit. Anhydrous stabilized Tetrahydrofuran (THF) and Certified ACS Grade Toluene were purchased and used as is from Acros Chemical and Fisher Scientific, respectively.

Glass Slide Fluorination. Plain microscope slides are placed into a staining dish that is filled with a solution formed using 10 μL (Heptadecafluoro-1,1,2,2-Tetra-Hydrodecyl) Trichlorosilane and 20 mL Chloroform. Microscope slides are submersed under the solution for approximately 3 hours. Treated slides are removed from the solution and left to dry in ambient condition for 1 hour. Slides are stored up to 7 days before retreatment.

Fiber Preparation. PMMA microcapillaries (from Paradigm Optics) with circular cross sections and an inner-to-outer diameter ratio of 50/100 μm are used as assembly frame and cut to 20 mm length using a scalpel knife. A 10 μL droplet of the 10 μm colloidal solution is placed onto the bottom end of the 20 mm long PMMA capillary fixed on a fluorinated glass slide. After 20 minutes, the capillary is moved to a new fluorinated glass slide and the bottom end of the capillary is placed into a 10 μL droplet of DI water to complete and keep the assembly hydrated. Once the completion of the assembly is confirmed with optical microscopy (20 min), the capillary is placed onto a new fluorinated glass slide. The process is repeated once with 2.5 μm and once with 10 μm colloids resulting in a multi-sectional colloidal crystal. The bottom end of the PMMA capillary containing the multi-sectional assembly is fixed onto a clean glass slide. 10 μL of NOA 60 are placed at the bottom end and allowed to infiltrate the colloidal assembly. After 24 hours of infiltration, the pre-polymer is cured under 365 nm long-wave UV light (from Spectroline A14-VS) for 2 hours. The cured *microcapillary/colloid/polymer* matrix is placed into a beaker with THF for 15 mins to dissolve and remove the PMMA capillary and the PS templating colloids. Repeated solvent dips and washes are performed as needed.

Imaging. Optical images are taken using the Olympus Vanox Microscope and scanning electron microscope images are taken using the Zeiss EVO-40 instrument in variable-pressure mode (P = 35-40 Pa). Variable-pressure SEM allows imaging of non-conducting materials without the requirement for gold coating enabling the analysis of surface pores.

3.3 Preparation of Porous Polymeric Fibers

A typical multi-sectional porous polymeric fiber (PPF) fabrication experiment is divided into three essential steps shown in Figure 3.1. The first step, *colloidal assembly*, involves the assembly of colloidal templates into a colloidal crystal inside a microcapillary. The second step, *infiltration*, utilizes an optically curable pre-polymer for infiltration of the colloidal crystal and formation of the PPF backbone. The last step, *solvent washing*, involves dips into organic solvents to remove the microcapillary and the colloidal templates resulting in a PPF.

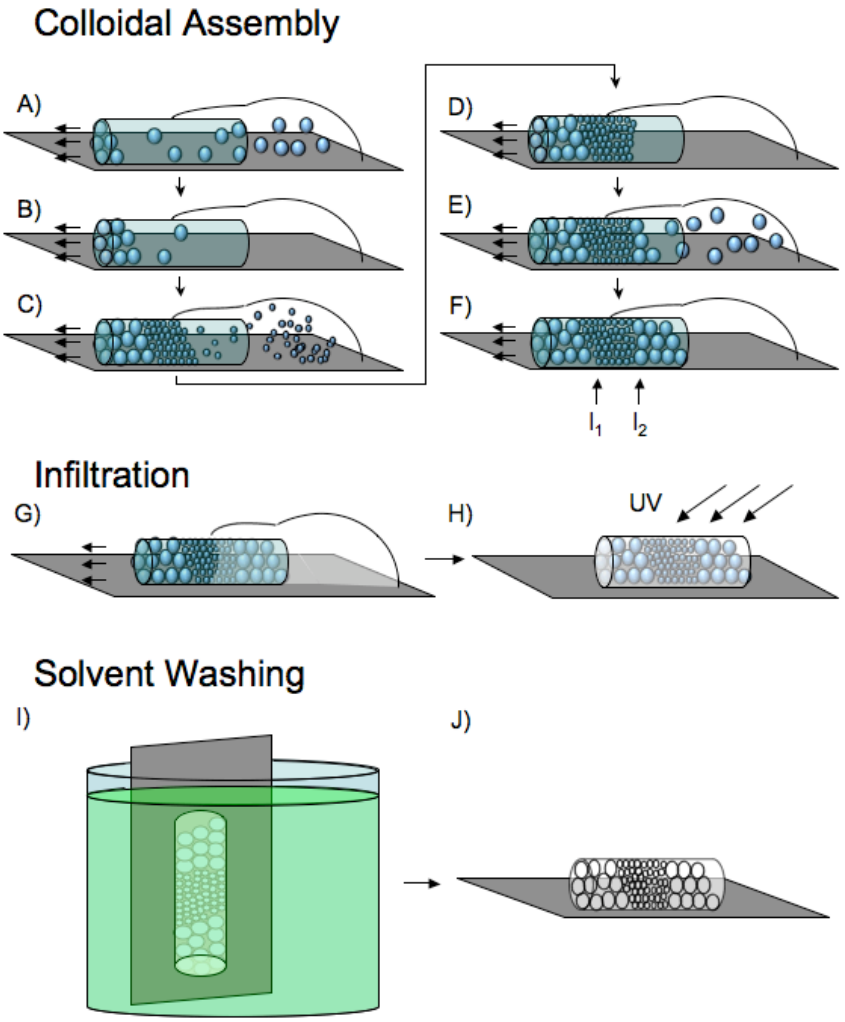

Figure 3.1 Schematic of process for fabrication of multi-sectional porous polymeric fiber (PPF). Top Panel: Colloidal Assembly - A) Colloidal solution of type A is placed at the bottom end of the microcapillary resulting in the intake of the solution and initiation of colloidal crystallization at the top end. B) Partially assembled colloidal crystal (type A) is moved into a DI water droplet to complete the assembly and to keep the assembly hydrated. C) Hydrated colloidal assembly of type A is moved into a colloidal solution of type B initiating secondary colloidal assembly. D) Secondary colloidal assembly is allowed to fully assemble and to stay hydrated in a fresh DI water droplet. E) Tertiary colloidal assembly of type A is initiated. F) Multi-sectional colloidal assembly within a microcapillary exhibiting interfaces I_1 and I_2 (see text); Middle Panel: Infiltration - G) A droplet of liquid pre-polymer is placed on the bottom end. H) Fully pre-polymer infiltrated colloidal assembly is UV cured; Bottom Panel: Washing - I) Cured *microcapillary/colloid/polymer* matrix is washed with solvent to dissolve microcapillary and colloidal templates. J) PPF is obtained after repeated solvent washing.

In the *colloidal assembly* step (Figure 3.1, top panel), a PMMA microcapillary with a circular cross section is cut to a desired length; the capillary serves as the colloidal assembly frame. The capillary is fixed onto a fluorinated substrate. Next, a droplet of the colloidal solution *A* with a predetermined concentration of polymeric colloidal particles is placed at one end of the capillary, hereafter referred to as the bottom end, and encapsulates the end of the capillary completely. The increased hydrophobicity of the fluorinated substrate leads to minimal spreading of the droplet and reduces evaporation of the colloidal solution applied. An immediate intake of colloidal solution at the bottom end results from the surface interaction between the solution and the capillary as reviewed in Chapter 2.[19] The meniscus of the colloidal solution is trapped at the opposite end of the capillary, hereafter referred to as the top end, and forms a capillary *wall/colloidal solution/air* interface. At the top end, the solvent starts to evaporate, initiating colloidal crystal formation (Figure 3.1A). Continuous colloidal crystal growth occurs as long as the droplet at the bottom end provides colloidal solution to the assembly system at a rate of $v_{assembly}$ = 0.4 mm/min.

Colloidal packing in cylindrical templates can be understood and predicted using the aspect ratio dependence reviewed in Chapter 2 based on sphere packing models developed by numerous researchers.[20,21] Especially, Mueller's model numerically simulates packing of monosized spheres in a cylindrical container by vertically stacking spheres implementing Bennett, Layer, and Alternate models. The model simulates six different aspect ratios ranging from 3.96 to 20.3 and predicts random packing for all of the ratios in this range. The experiments reported here use sulfate-terminated PS particles with diameters of 2.5 ± 0.1 μm (4%) and 10 ± 0.7 μm (7%) in capillaries with a 50 μm inner diameter resulting in aspect ratios of 20 and 5, respectively. Consequently, random packing is expected for the colloidal assemblies. In addition, the packing order and the crystalline quality of the assemblies are affected by the size distribution of the colloids.[22]

The polydispersity of the larger colloids (7%) is expected to result in assemblies with inferior quality compared to those obtained with the smaller monodispersed colloids (4%).

Once the desired length of the assembly of colloid *A* has been obtained, the bottom end of the capillary is moved into a droplet of particle-free DI water to facilitate transport of residual particles to the crystal and to keep the assembly hydrated (Figure 3.1B). Hydration of the assembly is critical in the transition from one colloid size to the next. In 80% of the experiments in our study when partial or complete drying of the colloidal assembly is allowed, formation of air pockets and/or the inability of the subsequent colloidal solution to re-wet the already formed colloidal assembly are observed and result in disorder and/or substantial void formation at the interfaces. Possible causes for the incomplete assembly wetting may be an increased hydrophobicity of the assembled polystyrene particles compared to bulk polystyrene and the formation of nanobubbles on the colloid surface reported by Ge et. al.[23] and Simonsen et. al.,[24] respectively.

The hydrated colloidal assembly matrix is then moved from the DI water droplet into a droplet of colloidal solution *B* with colloids of smaller diameter (Figure 3.1C). The colloidal particles with the smaller diameter assemble into a colloidal crystal section with an identical outer geometry dictated by the inner diameter of the capillary following the initial assembly. A repetition of the assembly process (Figures 3.1 A and B) with alternating colloidal solutions (Figures 3.1 C-F) results in a multi-sectioned cylindrical colloidal assembly within the capillary schematically shown in Figure 3.1F. Once the colloidal crystal with the desired length and number of sections has been fabricated, the assembly is dried under ambient conditions and placed onto a clean fluorinated substrate for further processing. As shown in Figure 3.1F, two types of interfaces, I_1 and I_2, are formed in the colloidal assembly with varying colloid sizes. I_1 describes the interface formed when switching from a large colloid (d ≥ 5 μm) to a small colloid (d < 5 μm), whereas I_2 describes the opposite transition from a small to a large colloid. The major difference between I_1 and I_2 is the angle of the interface with respect to the capillary cross section, i.e., the angle of I_1 is greater than that of I_2. The rationale for the observed difference in interface angle is the sedimentation of colloids with diameters larger than 5 μm within the length of the capillary.

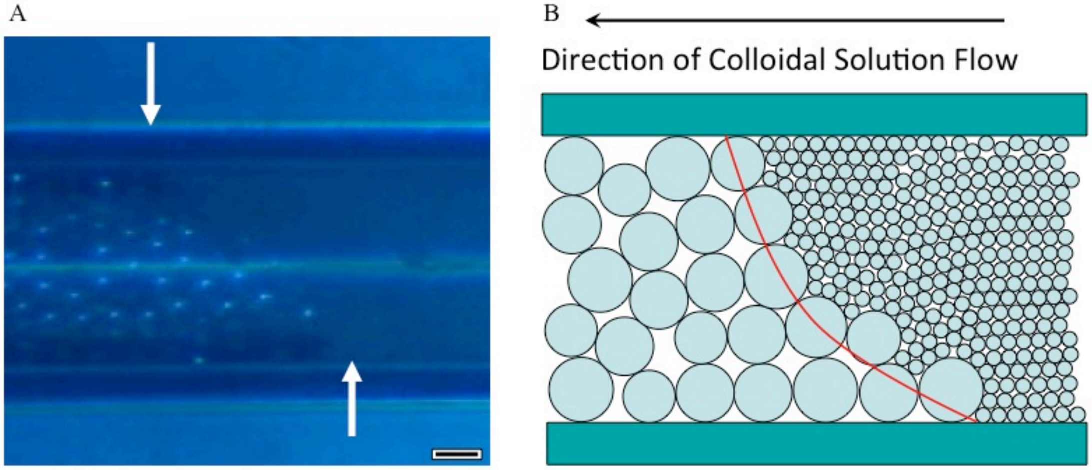

Figure 3.2 Side view of cylindrical colloidal assembly. A) Side view of interface I1 between assembly of 10 μm and 2.5 μm PS colloids in a 50 μm inner-diameter PMMA capillary using an optical microscope. Arrows indicate the top and bottom positions of interface I1 inside the PPMA capillary. Scale bar 10 μm. B) Schematic of interface I1 formed by transition from a large colloid to a small colloid.

Figure 3.2 shows an optical microscope image and a schematic depiction of interface, I_1, formed by the transition from large (d = 10 μm) to small colloids (d = 2.5 μm) inside a 50 μm (i.d.) capillary. Despite considerable effort to separate the colloidal assembly from the PMMA capillary, intact multi-sectional colloidal assemblies without capillary could not be obtained due to the brittle nature of the colloidal assembly. More specifically, during the solvent washing step needed to remove the capillary, the colloidal assemblies disassemble at both interfaces and lose their cylindrical geometry. Neither sintering of the particles nor careful washing procedures helped to overcome this problem. The colloidal assembly shown in Figure 3.2A has been assembled from the left to the right inside the capillary, i.e., the assembly is started with 10 μm colloids followed by 2.5 μm colloids yielding a type I_1 interface. The angle of the interface is 40º with respect to the capillary cross section. Formation of the interface angle is explained by colloidal sedimentation of the larger colloids ($d > 5$ μm). Sedimentation occurs during the assembly process along the length of the capillary and is responsible for the concentration of colloids near the lower side of the capillary leading to the angled interface, I_1. In contrast, interface, I_2, obtained when switching from smaller to larger colloids (Figure 3.1F) is much less angled because small ($d < 5$ μm) and submicron colloids exhibit negligible gravitational effects.[11,25] Figure 3.2B sketches the two-dimensional cross section of the interface I_1 formed at the transition from large to small colloids. The exact nature and shape of the interface could not be determined because isolation of the intact colloidal assembly from the capillary could not be achieved. However, tests with colloid sizes of 1, 2.5, 5, 8, 10, and 16 μm reveal an increased I_1 interface angle with increasing particle size. Note, the I_1 interface angle for larger colloids ($d > 5$ μm) can be improved by performing the assembly on a vibrational stage or by using a vertical assembly geometry. A detailed optical microscope image is depicted in Figure 3.3 with the I_1 and I_2 interfaces visible.

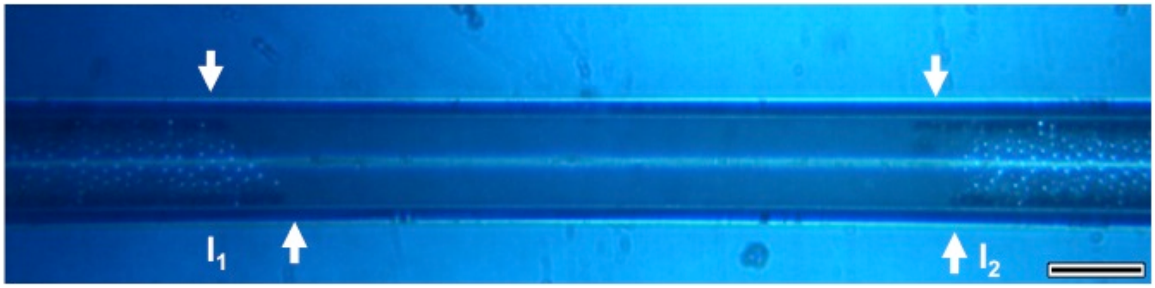

Figure 3.3 Optical microscope image of 50 mm PMMA capillary filled from left to right with 10 µm, 2.5 µm and 10 µm showing tilted interface I_1 and less angled interface I_2. White arrows indicate the interfaces at the upper and lower side of the fiber. Scale bar 50 µm.

In the *infiltration* step depicted in Figure 3.1 (middle panel), a droplet of ultra-violet (UV) curable polyurethane (PU) liquid pre-polymer is placed at the bottom-end of the capillary (Figure 3.1G). Subsequently, the liquid pre-polymer infiltrates the multi-sectioned colloidal assembly due to capillary forces (Figure 3.1H). The complete infiltration time depends on the surface area and volume to be infiltrated.[26] Experimentally, the completeness of pre-polymer infiltration into the colloidal assembly can be determined indubitably under an optical microscope due to refractive index matching. Non-infiltrated colloidal assemblies in air have a large refractive index mismatch (n_{PMMA} = 1.49, n_{PS} = 1.59, n_{air} = 1)[27,28] causing the colloidal assemblies to appear *white*. In contrast, pre-polymer infiltrated colloidal assemblies turn transparent due to the matching of the refractive indices (n_{PMMA} = 1.49, n_{PS} = 1.59, n_{PU} = 1.54).[27,28] Infiltration of the pre-polymer is completed within 24 hours and the infiltrated colloidal assembly is cured under a 365 nm UV light for 2 hours.

In the *solvent washing* step (Figure 3.1, bottom panel), the cured *microcapillary/colloid/polymer* matrix is moved to and fixated on a clean substrate for the organic solvent treatment, which leads to the formation of a porous structure. The substrate-mounted matrix is immersed in an organic solvent to dissolve and remove both the PMMA microcapillary and the templating PS colloids (Figure 3.1I). THF is selected for the initial solvent wash because of its ability to dissolve PMMA and PS polymers with a minimal sample exposure time. A 15 min dip into THF removes the PMMA capillary and the PS templating particles. Removal of PMMA is evidenced by a pronounced change in the rigidity of the fiber from stiff to highly flexible and free floating. This observation is supported by the Young's Moduli of PMMA (E = 3.1-3.8 GPa),[29] PS (3.2-3.4 MPa),[27] and PU (E = 19.3 MPa).[28] If the change in rigidity is not observed after the initial 15 min dip, additional dips into THF are performed. In the final washing step, the PPF is rinsed with 10 μL of toluene to remove residual PS, PMMA, and THF and dried under ambient conditions (Figure 3.1J).[30]

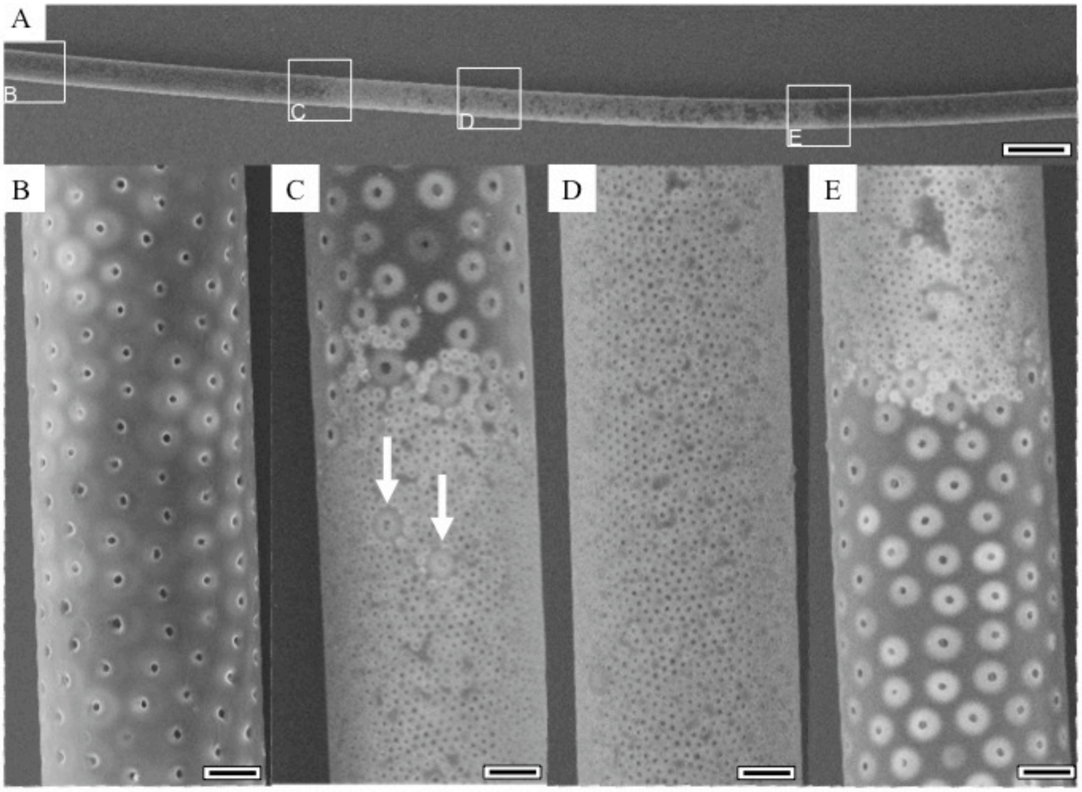

Figure 3.4 Scanning Electron Microscope (SEM) images of porous polymeric fiber (PPF) with three sections and two alternating pore sizes (10 and 2.5 μm). A) Large area view of cylindrical PPF. Scale bar 100 μm. Boxes indicate positions of areas magnified along the fiber. B) Top end of PPF templated with 10 μm colloids. Scale bar 10 μm. C) Top view of interface, I_1, between sections templated with 10 and 2.5 μm colloids. Arrows indicate 10 μm particles in 2.5 μm section (see text). Scale bar 10 μm. D) Porous section templated with 2.5 μm colloids. Scale bar 10 μm. E) Top view of interface, I_2, between sections templated with 2.5 and 10 μm colloids. Scale bar 10 μm.

The resulting PPF retains the cylindrical shape of the capillary (Figure 3.4) with pores of the size and shape of the templating colloids. Figure 3.4A shows the vp-SEM image of a typical multi-sectional PPF obtained after solvent washing with a total length of 24.6 mm and three alternating sections of 8.5, 0.9, and 15.2 mm length templated with 10 μm, 2.5 μm, and 10 μm colloids, respectively. The PPF shown in Figure 3.4A exhibits a uniform diameter of 49.9 ± 0.3 μm along the length of the sample. Measurements on a total of seven samples yield an average fiber diameter of 49.7 ± 2.1 μm. Comparison of the inner-diameter of the capillary (50.0 ± 2.5 μm) supplied by Paradigm Optics with the average fiber diameter (49.7 ± 2.1 μm) indicates negligible volume shrinkage during curing. For closer inspection of the surface pore structure in each section and in the interface region, higher magnification images are shown in Figures 3.4 B - E. Figure 3.4B shows the top-end of the PPF that has been fabricated using 10 μm PS colloids. A top view of the interface, I_1, between the 10 and 2.5 μm PS colloid-templated sections is depicted in Figure 3.4C. The width of the interface I_1 is approximately 28 μm and is caused by the sedimentation of the 10 μm colloidal templates (see above). Figure 3.4D depicts the fully formed PPF section templated by 2.5 μm PS colloids. Figure 3E shows a top view of the narrow interface, I_2, with a width of 10 μm oriented almost perpendicular to the fiber cross section formed by the transition from 2.5 to 10 μm PS colloidal templates. As predicted by Mueller's theory,[20] all sections show random packing. In Figures 3.4 C and E, a minute amount of colloidal mixing is observed near the interfaces. Arrows in Figure 3.4C indicate the positions of 10 μm pores in the 2.5 μm pore sections. This observation is accounted for by the detachment of residual colloids from the walls of the capillary at the bottom-end as the colloidal solution is switched to a new colloidal size.

Average surface pore sizes of 38% and 25% for templating colloid diameters of 2.5 and 10 μm, respectively, are determined using vp-SEM. Surface pore size analysis is performed using only pores that are parallel to the imaging plane, i.e., in the center of the fiber, to avoid errors due to variation in depth. Surface pore size measurements are performed on seven samples with an average length of 1.9 ± 0.2 cm. Each imaging section is 500 μm long and templated by either 2.5 or 10 μm PS colloids. The average surface pore sizes are measured to be 0.9 ± 0.1 μm and 2.5 ± 0.3 μm, respectively. The surface pore size within each sample varies from 0.7 to 1.1 μm and 2.2 to 3.1 μm for 2.5 and 10 μm PS templating colloids, respectively. Interestingly, the measured surface pore sizes are much smaller than those observed in planar assemblies (1/2 of the templating colloid diameter) obtained with similar colloidal sizes and infiltrating polymers.[26,31] The discrepancy in surface pore size can be rationalized by the longer infiltration times (hours vs. minutes) used for the PPFs.

Figure 3.5 shows three higher magnification vp-SEM images of the interfaces I_1 and I_2. Figure 3.5A shows a cross-section of an I_2 interface for a fiber from the batch shown in Figure 3.4. Porosity throughout the fiber is observed. Figures 3.5 B and C depict the I_2 and I_1 interfaces, respectively, of samples fabricated utilizing 10 and 2.5 μm colloidal templates with a shorter period (14 vs 24 hours) for the *infiltration* step (Figure 1; middle panel). The average surface pore sizes of the sample shown in Figure 3.5C are 3.4 ± 0.3 μm and 1.1 ± 0.1 μm, respectively, which correspond to 44% and 34% of the templating colloid size.

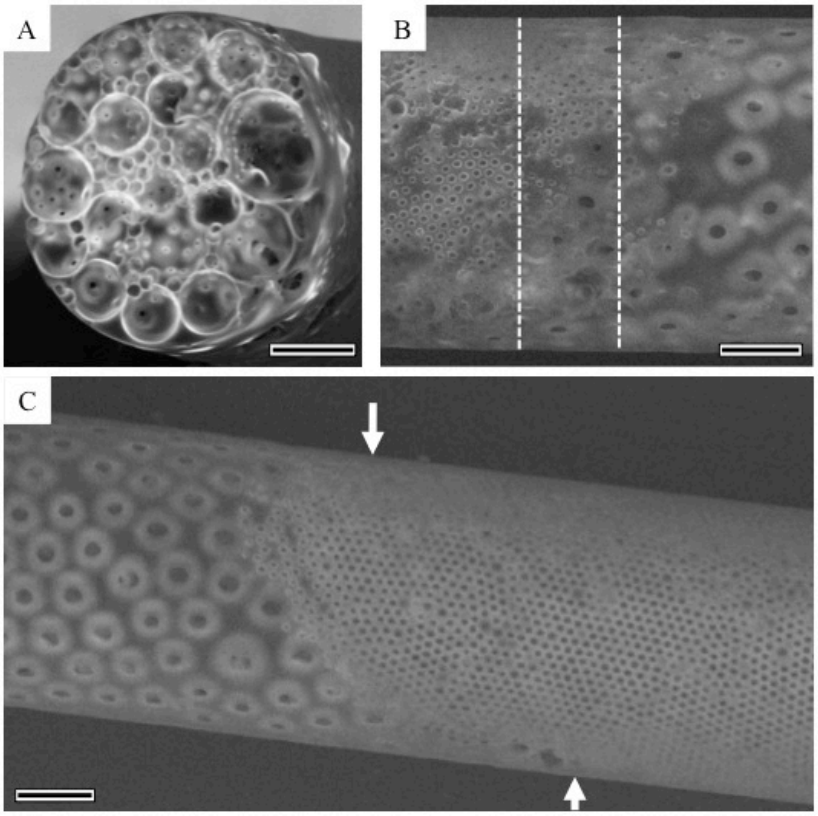

Figure 3.5. SEM images of fiber cross section and interfaces I_1 and I_2. A) Fiber cross section at interface I_2. B) Side view of interface, I_2, between sections templated with 2.5 and 10 µm colloids (dashed lines indicate interface region). C) Side view of interface, I_1, between sections templated with 10 and 2.5 µm colloids. The two arrows indicate the top and bottom position of the interface. All scale bars 12 µm.

The observed increase in the surface pore size can be rationalized by the time-dependent capillary phenomena and wetting process,[26] i.e., shorter infiltration time leads to less wetting and larger pores. Interestingly, the larger surface pores in the 10 µm colloidal-templated section reveal pores in the next layer.

Figure 3.5C enables a closer, indirect inspection of the type I_1 interface region which is caused by the sedimentation of 10 µm particles during colloidal assembly (see above). The arrows indicate the position of the interface at the upper and lower side of the fiber. At the interface, small pores formed by 2.5 µm colloids are positioned near and in between the larger pores formed by 10 µm colloids. This observation can be explained by the packing of 2.5 μm colloids into the uneven interface formed by the sedimented 10 μm colloids. Note, Descartes' circle theorem and the Soddy circles estimate the colloid size limit below which infiltration of smaller colloids into the section of the larger colloids occurs, Equation 1.[32]

$$d_{\text{small}} = \frac{d_{\text{large}}}{(3+2\sqrt{3})} \tag{3.1}$$

The theorem predicts a colloid size limit of d_{small} = 1.55 μm for a colloidal crystal section of 10 μm particles. Thus, the intercolloidal spacing in the 10 μm templated section is much less than 2.5 μm preventing the smaller particles (2.5 μm) from accessing the interstitial spaces.

In contrast to the fiber shown in Figure 3.4 and the prediction made by Mueller's theory,[20] the samples obtained with shorter infiltration time (Figures 3.5 B and C) show regional close packing. Possible reasons for the observed close packing are (i) the size distributions of the colloids used, (ii) the pre-polymer infiltration time, and (iii) the volume fraction of the colloidal solutions. The samples shown in Figures 3.5 B and C are fabricated with particles from a different batch. While each batch of colloids is reported with a similar average colloid size, the dispersity of the colloids varies from batch to batch resulting in different particle size distributions. In addition, the samples are prepared with different infiltration times resulting in larger surface pores in the samples shown in Figures 3.5 B and C. The larger pores may influence the perception of packing. Lastly, day-to-day variations in laboratory humidity are likely to affect the evaporation rate, which in turn influences the effective volume fraction in the droplet of colloidal solution placed at the bottom end of the capillary. In addition, Velev et. al.[8] and Wang et. al.[33] report the onset of concurrent nucleation, high friction, and impurities as possible reasons for the formation of polycrystalline domains with different orientation in planar and cylindrical geometries, respectively.

Considerations beyond the synthesis process and the characterization of the PPFs reported here concern the extent of scalability of the synthetic protocol. In the following, we give a brief discussion as to the limitations that should be considered for scale up (length of fiber, fiber and pore diameter) and fiber material choice. The length of the PPF is limited only by the amount of time allotted for the colloidal assembly, the pre-polymer infiltration, and the washing steps. All times reported here are for a 20 mm PPF length. Longer PPFs will require longer times. The diameter chosen for the PPF is affected by the intensity of the UV source (I_{UV}) and therefore the ability to cure the pre-polymer (e.g., $d_{PPF} = 50$ μm, $I_{UV} = 730$ μW/cm^2 at 15 cm from source, $t_{cure} = 2$ hours). A larger diameter results in a need for a higher UV intensity and longer curing time. The size of the colloids used is determined by the packing and porosity desired for the PPF as well as the type of transitions between sections (e.g., $d_{large} = 10$ μm, $d_{small} > 1.55$ μm). Last but not least, the type of polymer used for the infiltration step depends on (i) solvent compatibility, i.e., the templating colloid must be soluble in a solvent that does not dissolve the polymer and (ii) viscosity, i.e., a higher viscosity will lead to a longer infiltration time.

3.3 Summary

The described method allows the controlled assembly of multi-sectioned, three-dimensional colloidal crystals and the subsequent generation of porous polymeric fibers. The fabrication method is advantageous because it can be easily adjusted to make materials which can address specific experimental requirements by varying the aspect ratio (i.e., capillary and colloid diameter), the material of the templating particles and capillary, the length of the segments, and the infiltrating pre-polymer.

REFERENCES

1. Ulbricht, M. *Polymer* **2006,** *47*, 2217-2262.
2. Karageorgiou, V.; Kaplan, D. *Biomaterials* **2005,** *26*, 5474-5491.
3. Vankelecom, I. F. J. *Chemical Reviews* **2002,** *102*, 3779-3810.
4. Xia, Y. N.; Gates, B.; Yin, Y. D.; Lu, Y. *Advanced Materials* **2000,** *12*, 693-713.
5. Stein, A.; Schroden, R. C. *Current Opinion in Solid State & Materials Science* **2001,** *5*, 553-564.
6. Hoa, M. L. K.; Lu, M. H.; Zhang, Y. *Advances in Colloid and Interface Science* **2006,** *121*, 9-23.
7. Imhof, A.; Pine, D. J. *Nature* **1997,** *389*, 948-951.
8. Velev, O. D.; Lenhoff, A. M. *Current Opinion in Colloid & Interface Science* **2000,** *5*, 56-63.
9. Li, J.; Zhang, Y. *Chemistry of Materials* **2007,** *19*, 2581-2584.
10. Miguez, H.; Yang, S. M.; Ozin, G. A. *Langmuir* **2003,** *19*, 3479-3485.
11. Moon, J. H.; Kim, S.; Yi, G. R.; Lee, Y. H.; Yang, S. M. *Langmuir* **2004,** *20*, 2033-2035.
12. Hong, S. H.; Moon, J. H.; Lim, J. M.; Kim, S. H.; Yang, S. M. *Langmuir* **2005,** *21*, 10416-10421.
13. Yake, A.M.; Snyder, C.E.; Velegol, D. *Langmuir* **2007,** *23*, 9069-9075.
14. Velegol, D. *J. Nanophotonics* **2007,** *1*, 1-25.
15. Yan, F.; Goedel, A. *Advanced Materials* **2004,** 1*6*, 911-915.
16. Waterhouse, G. I. N.; Waterland, M. R. *Polyhedron* **2007,** *26*, 356-368.
17. Gates, B.; Qin, D.; Xia, Y. N. *Advanced Materials* **1999,** *11*, 466-469.
18. Lee, S. K.; Yi, G. R.; Yang, S. M. *Lab on aChip* **2006**, *6*, 1171-1177.
19. Hiemenz, P.; Rajagopalan, R. *Principles of Colloid and Surface Chemistry*; 3rd ed.; Marcel Dekker: NY, 1997; p 650.

20. Mueller, G. E. *Powder Technology* **1997,** *92*, 179-183.

21. Mueller, G. E. *Powder Technology* **2005,** *159*, 105-110.

22. Rengarajan, R.; Mittleman, D.; Rich, C.; Colvin, V. *Physical Review E* **2005,** *71*, 016615

23. Ge, H. L.; Song, Y. L.; Jiang, L.; Zhu, D. B. *Thin Solid Films* **2006,** *515*, 1539-1543.

24. Simonsen, A. C.; Hansen, P. L.; Klosgen, B. *Journal of Colloid and Interface Science* **2004,** *273*, 291-299.

25. Kim, B. M.; Qian, S.; Bau, H. H. *Nano Letter* **2005,** *5*, 873-878.

26. Jiang, P.; Hwang, K. S.; Mittleman, D. M.; Bertone, J. F.; Colvin, V. L. *Journal of American Chemical Society* **1999,** *121*, 11630-11637.

27. Brandrup, J. I., E.H.; Grulke, E.A.; Abe, A.; Bloch, D.R. *Polymer Handbook*; 4th ed.; John Wiley & Sons: NY, 2005.

28. *Technical Data Sheet - Norland Optical Adhesive*; Norland Product Inc.

29. Ishiyama, C.; Higo, Y. *Journal of Polymer Science Part B-Polymer Physics* **2002,** *40*, 460-465.

30. Stoye, D.; Freitag, W. *Paints, coatings, and solvents*; Wiley-VCH Verlag GmbH: Weinheim, 1998; p 431.

31. Gates, B.; Yin, Y. D.; Xia, Y. N. *Chemistry of Materials* **1999,** *11*, 2827-2836.

32. Coxeter, H. S. M. *Introduction to Geometry*; 2nd ed.; John Wiley & Sons: NY, 1969; p 13 -16.

33. Wang, H. Z.; Li, X. Y.; Nakamura, H.; Miyazaki, M. P.; Maeda, H. *Advanced Materials* **2002**, *22*, 1662-1666.

Chapter 4

Colloidal Delivery and Template System

In Chapter 4, a polymeric catalytic membrane reactor (CMR) is fabricated using alternating assemblies of surface-anisotropic (*sa*-) and plain (*p*-) polystyrene (PS) colloids as template. We report the preparation of TiO_2 *sa*-PS colloids by physical vapor deposition of titanium onto a colloidal monolayer in an oxygen-rich environment and employ the modified colloids as a means to deliver the TiO_2 catalyst to the CMR pores. *sa*-PS and *p*-PS colloids are assembled into alternating cylindrical sections inside a microcapillary followed by infiltration and curing of a liquid polymer precursor in the interstitial space of the assembly. Subsequent organic solvent treatment results in a cylindrical porous CMR with embedded TiO_2 caps. TiO_2 cap embedment, composition and surface morphology, surface pore structure, and cross-sectional integrity are analyzed using variable-pressure scanning electron microscopy, transmission electron microscopy, and X-ray photoelectron spectroscopy.

4.1 Introduction

Process intensification (PI) promises new modes of enhancement in reaction engineering by drastically improving the technique and operation of reactive separation.[1] Novel and innovative technology provides a pathway for process improvement by reducing equipment volume, processing time, energy consumption, and ultimately operational costs.[2] A notable PI is a Catalytic Membrane Reactor (CMR) where the unit operations of separation and reaction are combined into one spacial and temporal unit. CMRs offer numerous advantages in unit operations including (i) a chemical equilibrium shift brought on by continuous removal of a product from a reaction mixture to enhance yield; (ii) decreased product inhibition and increased overall reaction rate by continuous removal of a product; (iii) reduced side reactions by lower operating temperatures; and (iv) facilitated separation of reactants and products through membrane separation.[3, 4]

Polymeric CMRs, unlike metallic or inorganic CMRs, are being widely explored for various processes due to their economic efficiency and tailorable properties.[3, 5] Despite their advantageous process enhancement, polymeric CMRs are limited by the operating conditions, i.e., most often they are inoperable at an operating temperature above 250°C. However, even with this limitation, polymeric CMRs have numerous applications in volatile organic compound (VOC) degradation, hydrogenation, and other low-temperature catalytic reactive operations.[6]

Application, performance, and efficiency of a polymeric CMR depend on the distribution of the selected catalyst and the porous structure of the CMR.[7] These properties may be addressed and tailored by employing polymeric colloids in the fabrication of a CMR. For example, three-dimensional colloidal assemblies have been widely applied to template and synthesize ordered porous materials.[8] On the other hand, anisotropic surface-modification of colloids has gained immense interest due to the wide range of modifications available.[9, 10] Combining colloidal templating and anisotropic surface modification techniques yields a *surface-anisotropic colloidal delivery and* *template system* (*sa*-CDTS) for CMR synthesis, where the catalyst material distribution and porous structure are precisely controlled.

One of the many functional catalyst materials available that may be utilized in a CMR is Titanium (Ti) and its oxides (Ti_xO_y).[3, 11] Amongst multiple oxidation states of Ti_xO_y (x=1,2 y=1-3), TiO_2 is the principle component of all oxides.[12] TiO_2 has been reported to form on the surface of bulk Ti within milliseconds of exposure to air.[13] With prolonged exposure to oxygen and increased transport of Ti from the sub-oxide layer to the surface, a natural 10 nm thin TiO_2 layer is formed.[12-15] In addition to the naturally forming TiO_2, many processes including thermal plasma,[16] electrochemical,[14] and sputter deposition[17] as well as electric-arc physical vapor deposition[18] have been developed to induce the formation and deposition of TiO_2 films. Further, TiO_2 is extensively researched for its high photocatalytic activity at low temperature and economic efficiency in comparison to rare metal and other metal-oxide catalysts.[12, 19, 20] The research previously published focuses on utilizing the anatase phase of TiO_2 as it is the more catalytically active phase.[20] However, recently other phases have been explored including rutile, brookite, and amorphous, as well as the combination of different phases, and the doping of TiO_2 with different elements to form heterogeneous TiO_2 catalysts with tailored photocatalytic properties.[21-24]

4.2 Experimental Details

Materials. Sulfate-terminated polystyrene (PS) colloids with 2.5 ± 0.1 μm diameter and 8% (w/v) concentration in aqueous form were purchased from Invitrogen. A polymethylmethacrylate (PMMA) capillary of 50 ± 2.5 μm inner diameter (i.d.) on spools of 1 m was purchased from Paradigm Optics. Titanium sponge with diameters ranging from 2 to 12 mm was purchased from Aldrich. Ultra-violet (UV) light curable polyurethane liquid pre-polymer NOA 60 was purchased from Norland Optics. De-ionized (DI) water was obtained from a Millipore Milli-Q unit. Concentrated sulfuric acid and NOCHROMIX were purchased from Acros Chemical and Godax Laboratories, respectively. Mechanical grade silicon wafers were purchased from University Wafers. Anhydrous stabilized tetrahydrofuran (THF) and Certified ACS Grade toluene were purchased and used as is from Acros Chemical and Fisher Scientific, respectively. A custom blend of a 3:1 Ar:O_2 mixture was synthesized by and purchased from Airgas Inc.

Preparation of the Anisotropic Colloidal Delivery System. 100 μL of a PS colloidal solution are washed *three* times with 1000 μL of DI-water by ultra-sonication followed by centrifugation. The supernatant water is extracted to remove surfactants and to obtain a 16% (w/v) concentrated colloidal solution. 10 μL of the concentrated colloidal solution are placed between two acid-cleaned microscope glass slides mounted at an angle on a motorized stage PHD 2000 (Harvard Apparatus). The trapped colloidal solution is dragged (a modified Prevo et. al. process)[25] at a speed of 6 mm/min by the motion of the top glass slide. Monolayers with sub- to close-packed colloids are obtained and subsequently used for the deposition of TiO_2 by physical vapor deposition (PVD).[11] Approximately, 0.02 ± 0.01 g of titanium sponge is placed in the 3-strand tungsten wire basket (Ted Pella No. 76) inside the PVD unit (Cressington 308). With monolayer samples placed on a stage underneath the basket (sample-to-source distance is approximately 15 cm), the PVD chamber is pumped until a pressure of 5 x 10^{-4} Pa is reached. A 3:1 Ar:O_2 gas mixture is used to purge the evaporator chamber and then consistently leaked into the chamber to reach an evaporation pressure of 0.5 Pa. An average TiO_2 deposition rate of 0.3 nm/sec is used to obtain a nominal thickness of 30 ± 3 nm. In addition to the monolayer deposition, TiO_2 films are deposited under equivalent conditions on both 1 and 9 cm^2, acid-cleaned silicon wafers for X-ray spectroscopic and diffraction analysis (see below).

Surface Enhancement. The TiO_2-capped colloids on the glass slides are submerged under 200 mL of DI water and ultra-sonicated (40 kHz) for 15 min to lift off the colloids. A dilute suspension with a concentration of less than 0.01% w/v is obtained. The suspension is concentrated to 20 mL of 0.1% (w/v) by repeated centrifugation and supernatant removal. For external surface enhancement of the TiO_2 cap, 0.21 g of 4-aminobutanoic acid (ABA) is added to the 0.1% (w/v) colloidal suspension resulting in a 100 mM concentration. The ABA colloidal suspension is allowed to interact with the TiO_2 surface for approximately 24 hrs. The ABA colloidal suspension is then centrifuged to remove the supernatant, which contains the excess ABA. DI water is added to the sediment and the ABA-modified colloids are resuspended. The final ABA-modified colloidal suspension of 1% (w/v) is prepared for colloidal assembly by an identical process of centrifugation and removal of supernatant.

Fabrication of TiO_2 Loaded CMRs. Applying the protocol developed by Song et. al.,[8] cylindrical colloidal assemblies with alternating plain and TiO_2-capped colloidal assembly sections are obtained. The interstitial spaces formed by the multi-sectional assemblies are infiltrated with the UV curable pre-polymer NOA 60 for approximately 48 hours. Pre-polymer infiltrated multi-sectional assemblies are cured under 365 nm UV light for 2 hours at 730 $\mu W/cm^2$ (Spectroline A14VS) and an additional 30 mins at 8,000 μW/cm^2 (Dreve Polylux500). The cured matrix is subsequently treated with repeated 5 min dips in THF and washes with toluene. The PMMA capillary and colloids are removed during the solvent dissolution process leaving the TiO_2 caps behind in the pores of the hardened, cylindrical CMR.

Imaging and Spectroscopy. Scanning Electron Microscope (SEM) and High-Resolution SEM (HR-SEM) images are obtained with Carl Zeiss EVO 40 and Supra 55 SEMs, respectively. Both SEMs are equipped with variable-pressure (vp) mode and EDAX X-ray energy dispersive spectroscopy (EDS) units. The vp mode available on the EVO 40 and Supra 55 SEMs allows imaging of non-conductive samples without coating the samples with a conducting surface layer (Au or C) by admitting air or nitrogen into the vacuum chamber at a chamber pressure ranging from 35 to 40 Pa. The accelerating voltage used ranges from 10 – 13 kV and 15 – 20 kV for the EVO 40 and Supra 55, respectively.

For X-ray photoelectron spectroscopy (XPS), a 30 ± 3 nm thin film of TiO_2 is deposited onto a silicon wafer under the same conditions used for deposition on the colloidal monolayer. The XPS spectra of the thin coatings are recorded with a PHI 5500 spectrometer equipped with a hemispherical electron energy analyzer, a multichannel detector, and an Al K_α monochromator X-ray source running at 15 kV and 23.3 mA. The binding energy (BE) is internally referenced to the adventitious carbon C 1s peak at 284.6 eV.[26] High-resolution spectra are acquired with a pass energy of 23.5 eV and a BE resolution of 0.05 eV.

4.3 Surface Anistropic Colloids and Resulting CMRs

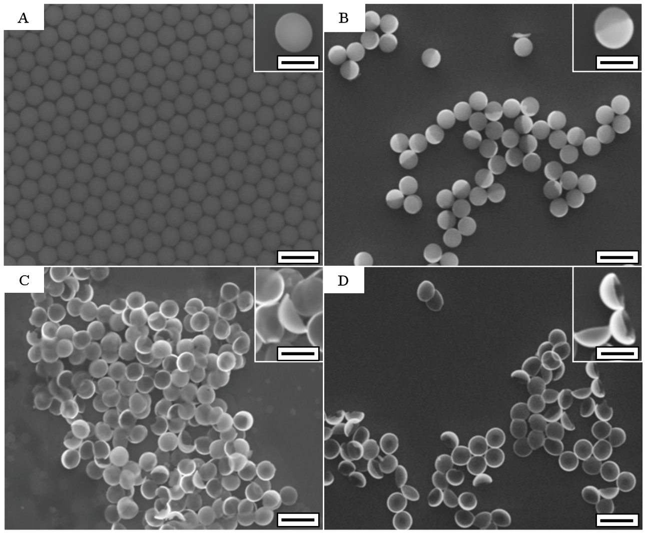

Figure 4.1 vp-SEM images of colloids and TiO_2 caps. (A) 2.5 µm *p*-PS colloids assembled into close-pack monolayer. Inset: Higher magnification single *p*-PS colloid image. (B) TiO_2 *sa*-PS colloids. Inset: Image of a single TiO_2 *sa*-PS colloid showing a bright coating. (C) TiO_2 caps collected after solvent treatments. Inset: Higher magnification image of an aggregate of caps. (D) TiO_2 caps obtained after 550°C calcination. Inset: Higher magnification image of three caps. Scale bars in all images and insets are 4 µm and 2 µm, respectively.

TiO_2 Surface Anisotropic Colloids and TiO_2 Caps. PVD on a colloidal monolayer results in the partial modification of the PS surface and removal of the PS core results in stable TiO_2 caps (Figure 4.1). Figure 4.1A and its inset show images of a close-packed monolayer of plain PS (*p*-PS) colloids with 2.5 ± 0.1 µm diameter and an isolated *p*-PS colloid, respectively. Both images show spheres with a uniform surface contrast. The images in Figure 4.1B and its inset show surface-anisotropic PS (*sa*-PS) colloids drop-casted onto a silicon wafer and an isolated *sa*-PS colloid, respectively. Spheres with bright hemispherical or half-moon shaped areas on the colloid surface are discernable in both images. The brighter region is the TiO_2-deposited region on the colloids, whereas the darker region is the unmodified PS surface of the colloids. Figure 4.1C and its inset show an aggregate of TiO_2 caps collected after solvent treatment using THF. Randomly orientated TiO_2 caps with no obvious damage due to the solvent treatment are observed in both images. Figure 4.1D and its inset depict hemispherical TiO_2 caps obtained after calcination of drop-casted *sa*-PS colloids at 550°C.[27] Some of the caps in Figures 4.1 B-D show some unevenness in the rim due to the onset of shadowing inherent to the close packing of the colloids during TiO_2 deposition.[28]

Table 4.1 TiO_2 EDS compositional data of clean wafer, *p*- and *sa*-PS colloids, solvent-treated and calcinated caps, and TiO_2 thin films. All EDS measurements are based on a total weight percentage of 100 wt %.

Samples	C (%)	Si (%)	Ti (%)	O (%)	Ratio (Ti:O)
Clean Wafer (reference)	<0.24	100.00	<0.10	<0.06	N/A
p-PS Colloids	97.26	2.74	<0.10	<0.06	N/A
sa-PS Colloids	93.36	0.50	1.90	4.24	1:2.23
Solvent Treated Caps	<0.24	89.48	3.21	7.31	1:2.28
Calcinated Caps	<0.24	58.50	12.82	28.68	1:2.24
Film	<0.24	89.20	3.40	7.40	1:2.18

The surface compositions of *p*- and *sa*-PS colloids, solvent-treated and calcinated TiO_2 caps, and TiO_2 thin films are measured using EDS. Table 4.1 lists the weight percent compositions measured for the five different types of specimens and the EDS data for a cleaned silicon wafer as reference. The values shown are the average of five measurements per specimen. The last column shows the ratio of titanium to oxygen signal. Comparison of the Ti:O data for *sa*-PS colloids, solvent-treated and calcinated TiO_2 caps, and TiO_2 thin films reveals that all four Ti:O ratios are ~1:2.2 and agree within 2%. The variation of the absolute values for titanium (Ti at 4.5 eV) and oxygen (O at 0.5 eV) from specimen to specimen is largely due to the different titanium oxide thickness in each type of specimen measured. All EDS analyses are performed on a cleaned silicon wafer, which does not show any traceable carbon, titanium, or oxygen peaks.

Table 4.2. XPS binding energy (eV) data for Ti $2p_{3/2}$, O 1*s*, and C 1*s* taken from NIST database[26] calibrated with respect to adventitious carbon (*Adv.* C 1*s 284*.8 eV).

Samples	Ti $2p_{3/2}$ (eV)	O 1*s* (eV)	C 1*s* (eV)
TiC[a]	454.9	N/A	281.7
TiO[b]	454.6	N/A	N/A
Ti_2O_3[c]	457.8	529.6	N/A
TiO_2[b]	458.9	530.2	N/A
TiO_2 Film[d]	458.9 ± 0.3	530.5 ± 0.5	N/A

[a] Galuska, A. et al.[26, 29]; [b] Gonbeau, D. et al. [26, 30]; [c] Werfel, F. et al.[26, 31]; [d] This work.

High-resolution XPS (HR-XPS) analysis is performed on five TiO_2 thin films (d = 30 ± 3 nm) on silicon wafers. Table 5.2 shows reference values taken from the National Institute of Standards and Technology database[26] for the Ti $2p_{3/2}$, O 1*s*, and C 1*s* XPS peak positions of titanium carbide (TiC) and various titanium oxides (TiO, Ti_2O_3, and TiO_2), as well as values measured for the freshly prepared TiO_2 thin films. All XPS values are calibrated with respect to adventitious carbon (C 1*s*) at a binding energy of 284.8 eV. The averages obtained for the freshly prepared thin film samples are 458.9 ± 0.3 eV for Ti $2p_{3/2}$ and 530.5 ± 0.5 eV for O 1*s*. These Ti $2p_{3/2}$ and O 1*s* binding energies are in a good agreement with the values listed for TiO_2 and clearly differ from the values expected for partially oxidized forms of titanium (e.g., TiO and Ti_2O_3) confirming the effective formation of TiO_2 when titanium is vapor deposited in a 3:1 Ar:O_2 mixture. In addition, no XPS signal is detected in the range where the Ti $2p_{3/2}$ for TiC is expected indicating that the vapor deposition and solvent treatment do not lead to TiC formation on the TiO_2 catalyst.

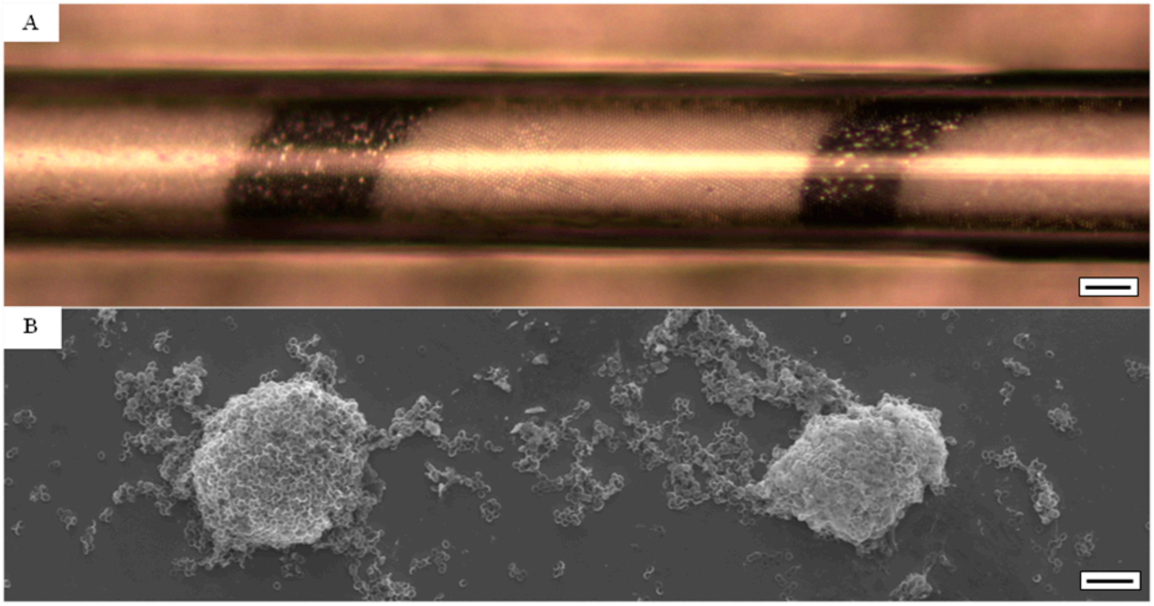

Figure 4.2 (A) Optical microscope image of a dried multi-sectional colloidal assembly fabricated using *p*-PS and TiO_2 *sa*-PS colloids. The dark segments with varying contrast depict regions of assembled TiO_2 *sa*-PS colloids. Scale bar 15 μm. (B) SEM image of the multi-sectional assembly depicted in (A) after calcinations at 550°C. Two piles of calcinated caps at 130 μm distance are observed. Scale bar 15 μm.

Fabrication of the CMR via TiO_2 Surface Anisotropic Colloidal Delivery System. The actual shape of the CMR is determined by the geometric confinement defined by the initial template used for the colloidal assembly. A cylindrical geometry is chosen as CMR template (Figure 4.2). Figure 4.2A shows an optical microscope image of a multi-sectional colloidal assembly in a 50 ± 2.5 μm (i.d.) PMMA capillary. The image depicts a colloidal assembly region with five alternating sections of *p*-PS and *sa*-PS colloids of the same size. Starting from left to right, alternating sections of 77 (*p*), 48 (*sa*), 140 (*p*), 31 (*sa*), and 77 (*p*) μm lengths are successively assembled inside the capillary. The five sections are distinguished by their color. The *sa* sections are dark and show a varying contrast along the length of the section indicating a random orientation of the caps, whereas the *p* sections exhibit a uniform white color throughout the sections. Figure 4.2B shows an SEM image (same scale) of the assembly shown in Figure 4.2A after calcination at 550°C. During calcination, the PS colloidal templates and PMMA capillary decompose into H_2O and CO_2, while the TiO_2 caps are left behind. Two distinguishable piles of TiO_2 caps and a distribution of caps in between the piles are observed. The distance between the piles (130 μm) is comparable to the distance in the original assembly (140 μm). The distribution of caps in between and around the piles is likely to result from the instability of the cap assembly during the escaping of gas formed as part of the decomposition process.

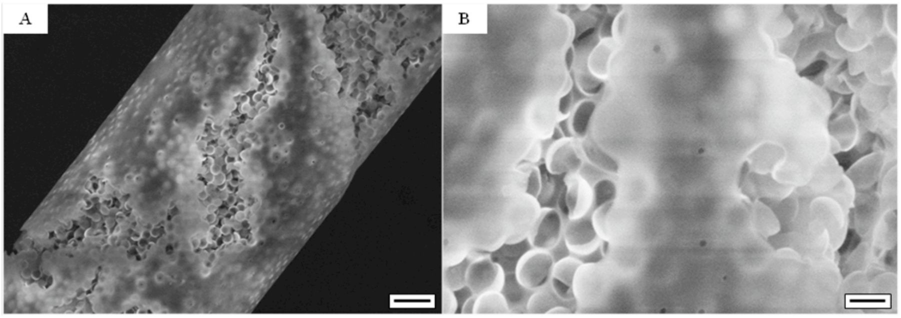

Figure 4.3 SEM images of *sa*-PS templated CMR region with voids after infiltration, curing and solvent treatment. (A) Region of CMR with multiple voids resulting from incomplete infiltration of liquid pre-polymer. Scale bar 8 µm. (B) Higher magnification image of a void region showing intact TiO_2 caps inside the CMR. Scale bar 2 µm.

CMRs with Bare TiO_2 Caps. After infiltration, curing, and solvent treatment of a colloidal assembly as shown in Figure 4.2A,[8] CMRs fabricated using *sa*-PS and *p*-PS colloids show voids on the surface of the CMR section templated using the *sa*-PS colloids, while sections templated with *p*-PS particles are well formed. Figure 4.3A shows a section of a multi-section CMR templated with *sa*-PS colloids. Several regions of incomplete polymer filling, i.e., voids, are observed on the CMR surface, while the cylindrical shape and diameter of the CMR remains consistent with the i.d. of the microcapillary template. Figure 4.3B depicts a high-magnification image of a void region, where the random orientation of the TiO_2 caps resulting from the CDTS is visible. No damage of the TiO_2 caps inside the CMR as a result of polymer infiltration, curing, and template removal is observed.

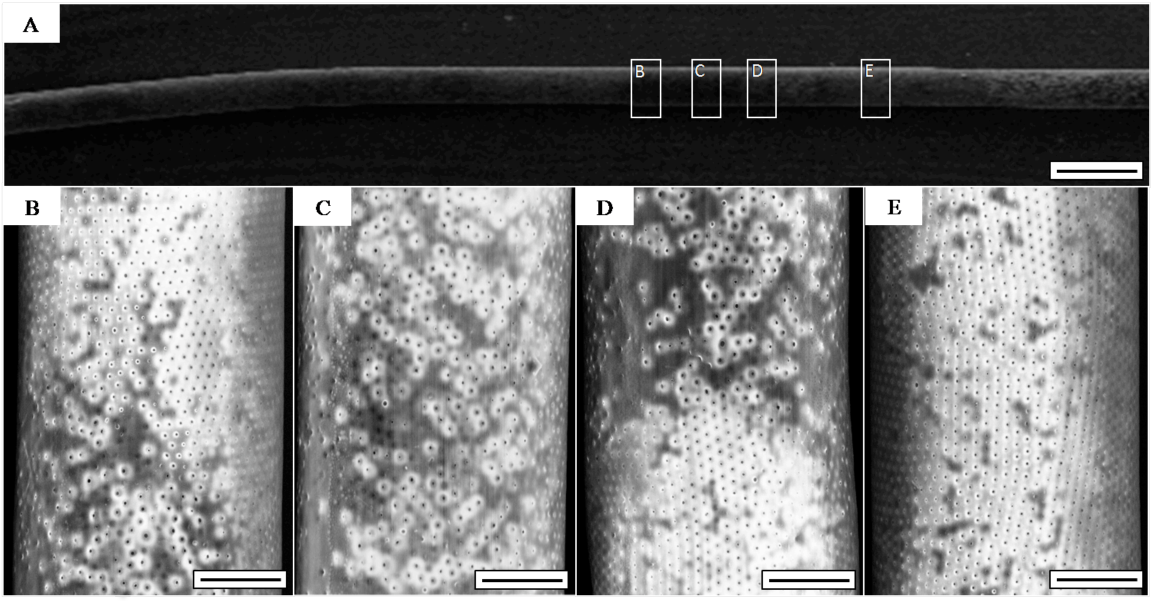

Figure 4.4 SEM images of a fully infiltrated CMR with three sections. (A) Large scale view of CMR. Scale bar 100 µm. (B) CMR region templated by *p*-PS colloids (Top) and surface-enhanced *sa*-PS colloids (Bottom). Scale bar 14 µm. (C) CMR region templated with surface-enhanced *sa*-PS colloids. Scale bar 14 µm. (D) CMR region templated by surface-enhanced *sa*-PS colloids (Top) and *p*-PS colloids (Bottom). Scale bar 14 µm. (E) CMR region templated with *p*-PS colloids. Scale bar 14 µm.

CMRs with Surface Enhanced TiO_2 Caps. Increased wettability of the pre-polymer and the *sa*-PS colloids ensures complete infiltration of the colloidal template. In Figure 4.4, a fully infiltrated, cylindrical polymeric CMR is depicted that has been synthesized utilizing ABA surface-enhanced TiO_2 CDTS. Figure 4.4A depicts a large area view of a 1.8 mm section of a 1.5 cm long polymeric CMR fiber with catalytic sections synthesized using plain and surface-enhanced TiO_2 CDTS. High magnification images of several regions of the CMR are depicted in Figures 4.4B through 4.4E. Figure 4.4B shows the CMR's first interface synthesized using *p*-PS (top-half) and surface enhanced *sa*-PS colloids (bottom-half). Surface pores in the region templated by *p*-PS colloids exhibit uniform pores indicating a close-packed arrangement of the colloids, whereas the section of the CMR templated using surface-enhanced *sa*-PS colloids shows an irregular pore arrangement and varying surface pores sizes, but no void formation as observed for unmodified *sa*-PS colloids (Figure 4.3). Figure 4.4C shows a CMR region templated by surface-enhanced *sa*-PS colloids. An irregular arrangement of surface pores and a distribution of pore sizes comparable to that in the bottom half of Figure 4.4B are observed throughout the section, but again no voids are formed. In Figure 4.4D, the second interface between sections templated with surface-enhanced *sa*-PS (top half) and *p*-PS colloids (bottom half) is shown. Figure 4.4E shows a region with a well-ordered arrangement of pores and evenly distributed pores resulting from a close-packed *p*-PS colloidal template. The length of each section shown is approximately 77 μm.

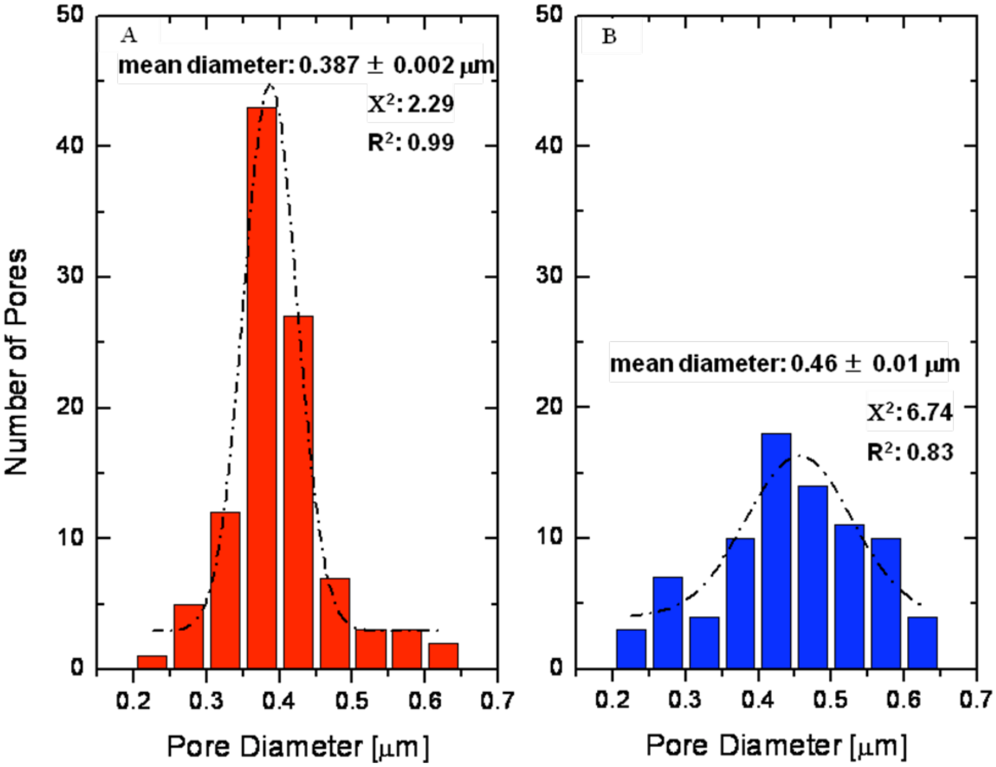

Figure 4.5 Surface pore diameter size distribution of CMR regions. (A) Surface pore diameter distribution of CMR regions templated by *p*-PS colloids. Dash-dotted line indicates Gaussian fit of the distribution with $\chi^2 = 2.29$ and $R^2 = 0.99$. (B) Surface pore diameter distribution of CMR regions template by surface-enhanced *sa*-PS colloids. Dash-dotted line indicates Gaussian fit of the distribution with $\chi^2 = 6.74$ and $R^2 = 0.83$.

Surface Pore Size Analysis. Figure 4.5 shows the surface pore diameter distribution obtained from five CMRs that have been fabricated using *p*-PS and surface-enhanced *sa*-PS colloids. Due to the curvature of the CMR, only the surface pores along the center (± 10 μm) of the CMR are measured. Each section measured is approximately 500 μm long. Figure 4.5 shows the distribution of surface pore diameters measured for the CMRs templated by *p*-PS colloids (Figure 4.5 A) and *sa*-PS colloids (Figure 4.5B). The surface pore diameters vary between 0.2 and 0.65 μm. Both distributions are fit with a Gaussian function (dash-dotted line). For the *p*-PS templated section the distribution is narrow and Gaussian-like (X^2 = 2.29 and R^2 = 0.99) with an average pore size of 0.387 ± 0.002 μm, while the distribution of surface pore diameters in the section templated by surface enhanced *sa*-PS colloids is much broader and not well fit by a Gaussian function (X^2 = 6.74 and R^2 = 0.83) with an average pore size of 0.46 ± 0.10 μm.

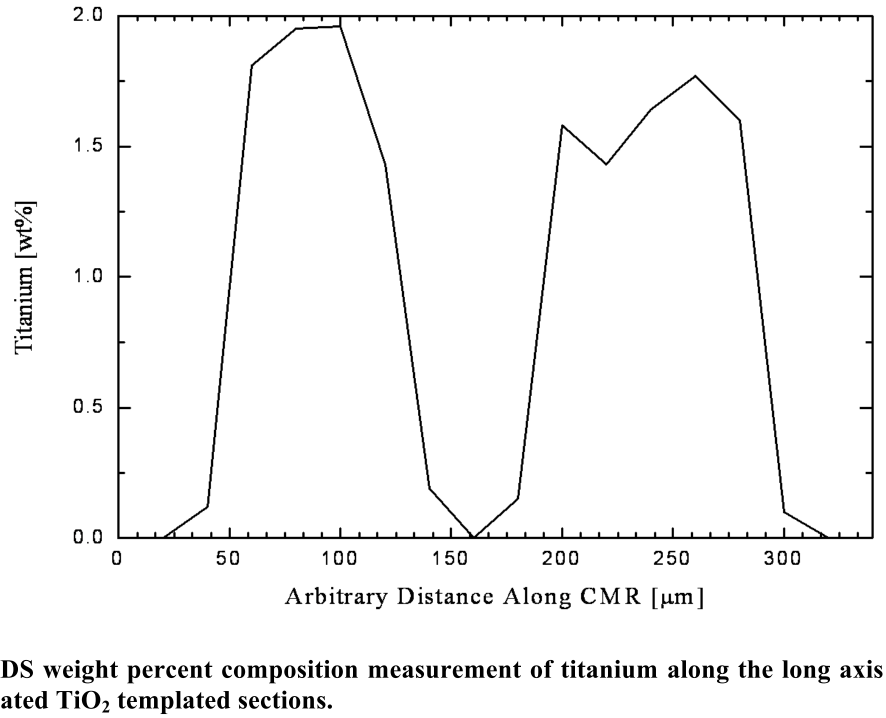

Figure 4.6 EDS weight percent composition measurement of titanium along the long axis of a CMR with two isolated TiO_2 templated sections.

EDS Characterization of Fibers. EDS measurements give insight into the width of the interfaces between *p*-PS and *sa*-PS templated sections by measuring the amount of titanium and oxygen in each section. Figure 4.6 shows a graph of the weight percent composition of Ti along the length of a multi-sectional CMR with alternating segments as shown in Figure 4.4. The percent composition is based on the Ti-K band data obtained with EDS. The fiber composition is analyzed every 20 μm starting approximately 40 μm prior to the interface depicted in Figure 4.4B. The effective electron beam spot size is estimated to be ≤ 3 μm diameter. This estimate is obtained by measuring the size of a burned area on a sample resulting from prolonged exposure of the sample to the electron beam and EDAX electron flight simulation. The changes in the weight percentage observed between the 20-60, 120-160, 160-200, and 280-320 μm points show a gradual increase and decrease in titanium weight percentage indicating that the interfaces have a width of less than 40 μm in good agreement with the interface width (28 μm) observed previously.[8] The maximum percent compositions of Ti for the two Ti regions are 1.86 and 1.75 wt%.

4.4 Discussion

The CDTS methodology enables the control of various characteristics and properties of a CMR that affect the reactive separation process such as reactor shape and size, pore structure, pore size distribution, and catalyst distribution within the CMR.[3, 4] In the following section, we will discuss the overall assembly and structure of the CMR, the catalyst cap distribution and orientation in the CMR, and the catalyst cap composition and structure.

The shape and size of the CMR are determined by the chosen application and the experimental set up it is used in. Once the outer geometric dimensions of the CMR are determined, obtaining a desired pore structure over a defined length is the next crucial characteristic that needs to be controlled for an effective CMR.[3] A complete fiber with surface pores and defined TiO_2-loaded sections fabricated using CDTS is shown in Figure 4.4. The complete formation of a fiber is achieved through surface enhancement of the TiO_2 caps by reaction with the carboxyl group (-COOH) of the ABA prior to assembly.[32] The reactive adsorption of the carboxyl group on the TiO_2 cap allows the amine group of the ABA, located at the opposite end of the chain, to repel the colloids from each other in the suspension and facilitate the transport of the amine based polyurethane pre-polymer into the colloidal template during infiltration. As a result the colloidal template is completely infiltrated compared to the CMR fabricated by employing unmodified *sa*-PS colloids (Figure 4.3).

Interestingly, the voids found on the CMR surface in Figure 4.3 offer some insight into the internal structure of the CMR and the stability of the TiO_2 caps. After repeated exposure to organic solvents, ultra-sonication, and heat treatments during the CMR fabrication process the caps turn out to be chemical, physical, and thermodynamic stable as confirmed by the higher resolution SEM image in Figure 4.3B. The caps show no deformation or change in shape, which is in good agreement with previously reported findings.[33]

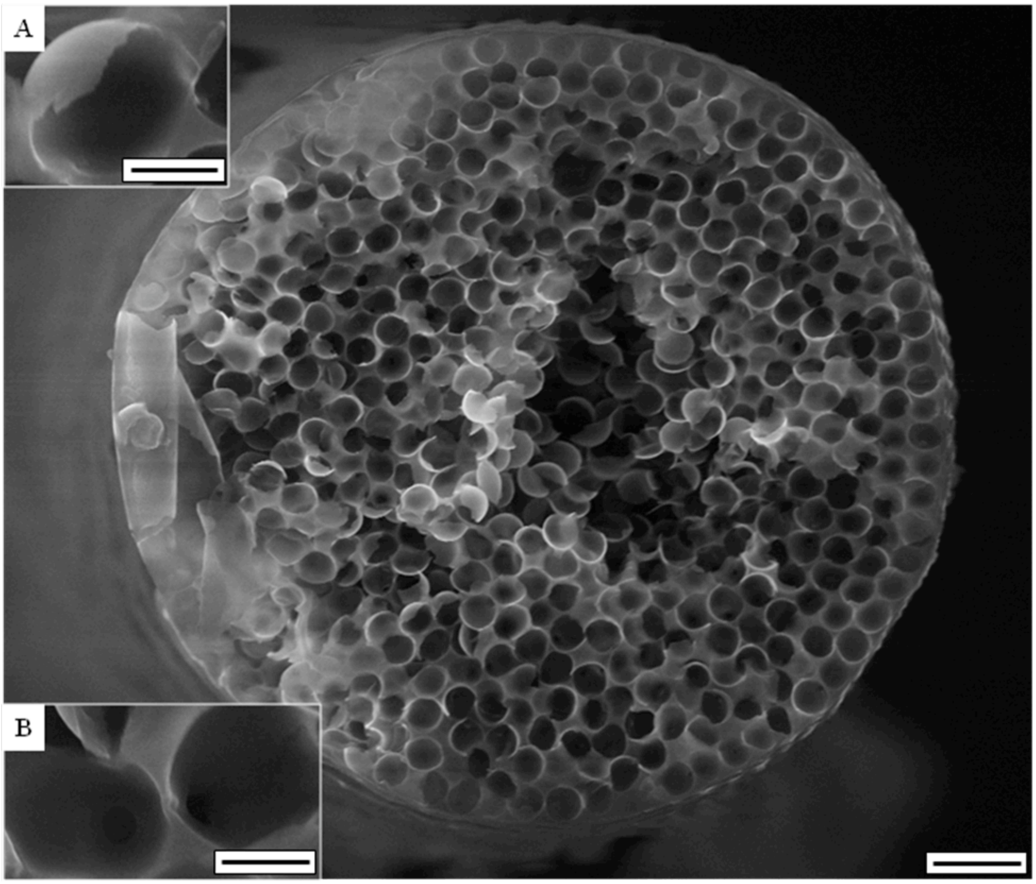

Figure 4.7 Cross-sectional view of a CMR section with TiO_2 caps. Scale bar 5 µm. Insets A and B show higher magnification images of an embedded cap and interconnecting pores, respectively. Scale bar 1 µm.

The cap stability and inner pore structure is further confirmed by cross-sectional analysis of the CMR. Figure 4.7 shows a cross-sectional SEM image of a CMR sheared under liquid N_2 along the section with the TiO_2 caps. Caps (Inset A) and pores (Inset B) are visible in the cross-sectional image indicating that the TiO_2 caps are stable and the colloidal template has been completely infiltrated leading to a porous structure throughout the fiber. In addition, the cross-sectional image reveals the random orientation of the caps within the CMR pores in good agreement with the random arrangement found before and after calcination of the multi-sectional colloidal template (Figure 4.2). Upon closer inspection, the structure of the interconnecting pores in the TiO_2 section seems to be less regular than that observed for plain colloids,[8] in good agreement with the presence and orientation of caps in the pores (Figure 4.7, Inset B). For example, if the caps of two colloids are in physical contact with each other or when a cap and an unmodified particle surface are in contact, no pore formation is expected, whereas when two unmodified particle surfaces are in contact, formation of a pore is expected.[34, 35] Further, the CMR sections fabricated using TiO_2 CDTS show a random surface pore arrangement (Figure 4.4C), while the *p*-PS colloid templated sections show ordered surface pore structures (Figure 4.4E).

The quality and composition of the cap surfaces are crucial in obtaining a catalytically active surface. TiO_2 is deposited onto the PS colloids and later exposed to solvents to remove the colloidal template. During the process, diffusion and adhesion of carbon and/or other organic compounds may occur. Therefore, the compositional and structural analysis of the caps is required. EDS analysis (Table 4.1) indicates that caps resulting from solvent treatment contain no traceable carbon residue from either the solvents or the PS colloid. Further, the low temperature of the substrate at which the deposition is performed prevents the formation of titanium carbides and diffusion of carbon into the deposited TiO_2, which occurs above 200°C.[36, 37] Note, the glass transition temperature of bulk polystyrene is $T_g = 100°C$.[38] Lastly, no thermodynamic changes are expected during the short deposition time (~1.5 mins) owing to the low thermal conductivity of TiO_2 ($k_{300K} < 1\ W\ m^{-1}\ K^{-1}$).[39] Comparison of EDS data for solvent-treated caps and the 30 nm thin TiO_2 films (Table 1), suggests that films and caps prepared under identical conditions have very similar compositions as indicated by their comparable Ti:O ratios.

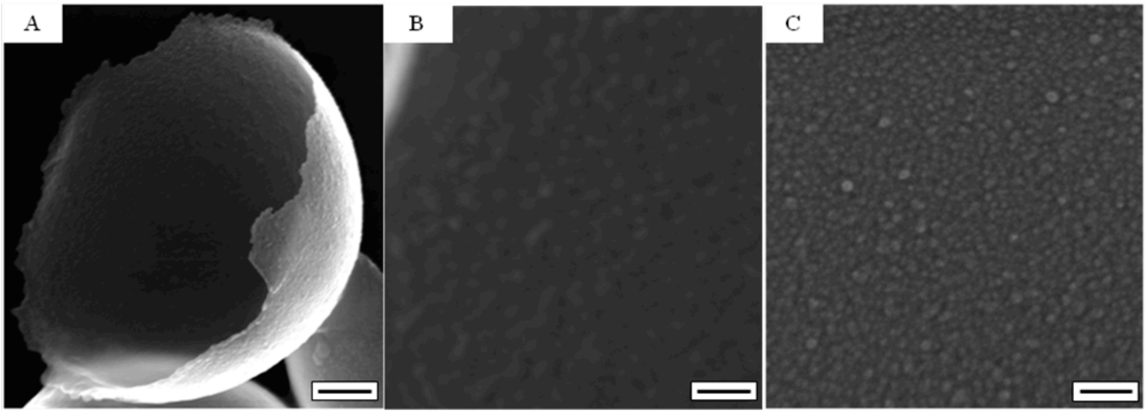

Figure 4.8 HR-SEM images of TiO_2 caps and thin films (A) Image of a solvent treated cap. Scale bar 300 nm. (B) Higher magnification image of the internal surface of the cap at 2 mm working distance (see text). Scale bar 50 nm. (C) Surface morphology of a TiO_2 thin film on a silicon wafer. Scale bar 50 nm.

The similarity between the TiO_2 caps and the TiO_2 thin film is further validated by HR-SEM imaging. The HR-SEM images of a cap and its inside surface and a TiO_2 thin film on a silicon wafer are shown in Figure 4.8. Figure 4.8A confirms clean removal of PS residues from the internal surface of the cap as suggested by the absence of a carbon signal in the EDS data of the solvent-treated caps. Figure 4.8B shows a high-resolution image of the inside surface of the cap shown in Figure 4.8A. The surface is found to be grainy with grains ranging from ~5 to ~15 nm. Note, the image appears out of focus due to the curved nature of the cap and the very short working distance (2 mm) used during the imaging. The former may result in a larger apparent size of the grains owing to the limited depth of field. Comparison of Figure 4.8B with the thin film surface (Figure 4.8C) reveals a comparable surface morphology with somewhat smaller grains ($d = 7 \pm 4$ nm). Figure 4.9 shows high-resolution XPS spectra collected on the thin films confirming TiO_2 as the composition of the thin films (Table 4.2).[21, 36]

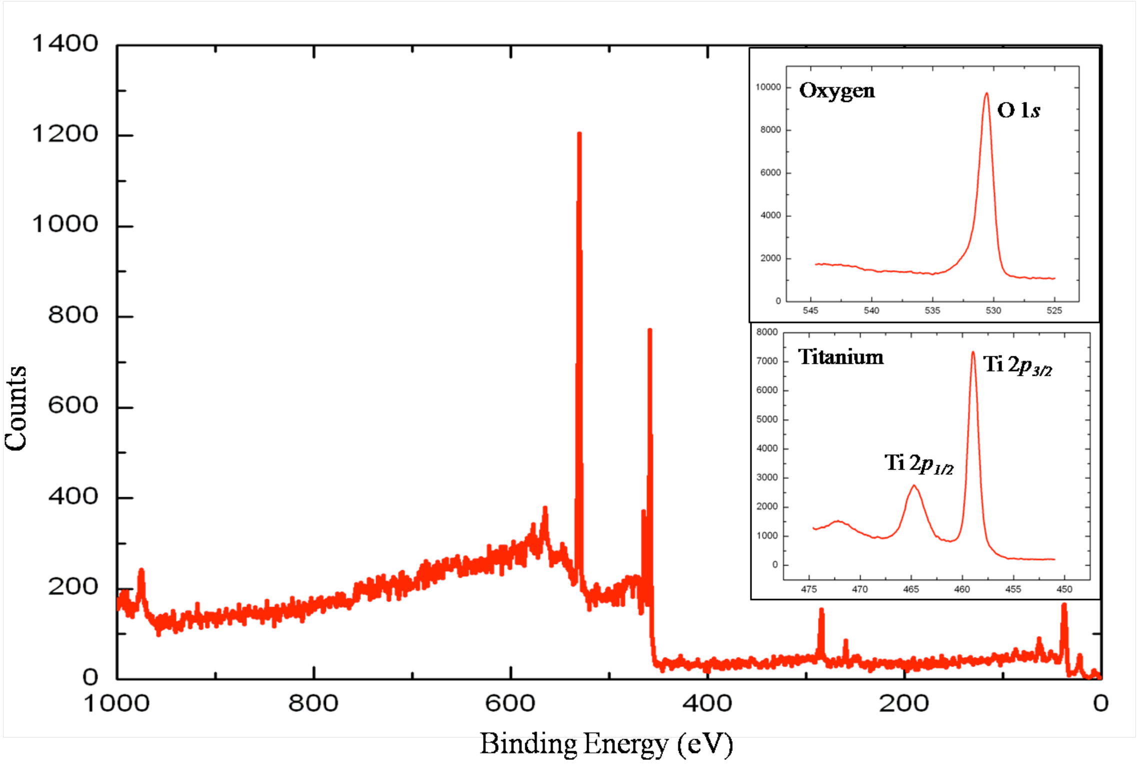

Figure 4.9 Survey XPS performed on thin film of TiO_2 deposited on clean silicon wafer. Inset: High-resolution XPS data of Oxygen and Titanium Region.

In an effort to determine the crystallinity and phase of the TiO_2 thin films, X-ray diffractometry (XRD), electron back-scatter diffractometry (EBSD) and transmission electron microscopy (TEM) are performed on the thin films. No XRD and EBSD patterns are detected that would allow an identification of the TiO_2 structure and phase. A possible rationale for this finding is that the (30 ± 3 nm) TiO_2 films used are too thin. Usually thin films with thickness greater than 500 nm are used in XRD measurements and grain domains greater than 50 nm are required for EBSD measurements.[40-42] While generally possible with our evaporation set-up, deposition of thicker TiO_2 films is complicated by the small size of the tungsten basket used in our PVD system. The small basket size requires reloading of the Ti sponge during evaporation of thick films, which may cause contamination of the films by exposure to air. In addition, the thickness of the films used for diffraction measurements should match the thickness of the caps used for the CMR (~30 nm) to ensure comparability. Last but not least, TEM characterization was performed on TiO_2 thin films (30 nm) evaporated on TEM grids . Comparison of the diffraction pattern of the TiO_2 thin film with that of a plain titanium film of comparable thickness suggests that the TiO_2 thin film is amorphous as shown in Figure 4.10. Interestingly, Eufinger and co-workers[40] term thin TiO_2 films that are undetectable with XRD but show a short-range ordering (<10 nm) in HR-SEM *XRD amorphous*. The TiO_2 cap and films used in this study (Figure 4.8) show TiO_2 grains ranging from 5 to 15 nm comparable to Eufinger's films. Therefore, we refer to our TiO_2 cap material as *XRD amorphous* TiO_2.

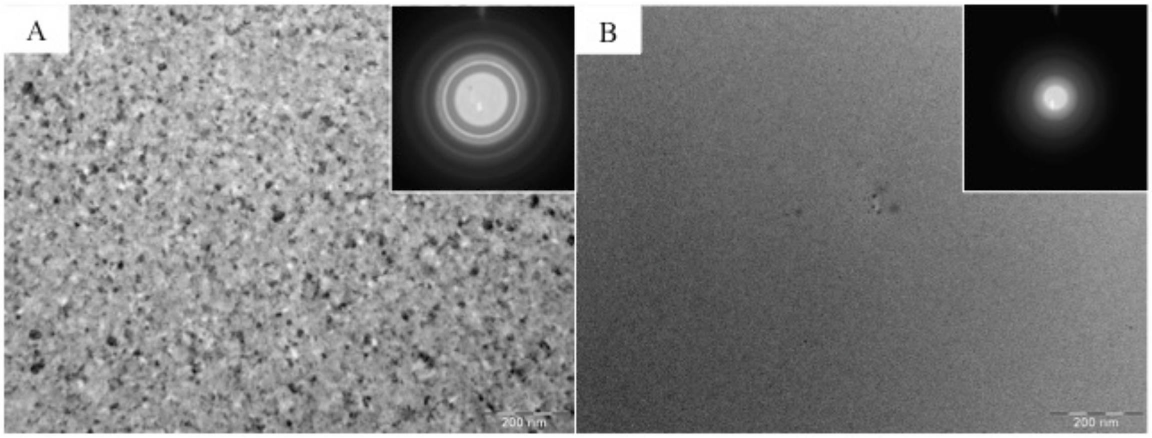

Figure 4.10 TEM images and diffraction pattern. A) TEM image of a titanium thin film on a Cu-TEM grid. Scale bar 200 nm. Inset: Electron diffraction pattern. B) Image of a TiO_2 thin film on a Cu-TEM grid. Scale bar 200 nm. Inset: Electron diffraction pattern.

Eufinger and co-workers[40] further show that short-range ordering or small grains in *XRD amorphous* TiO_2 show an enhanced charge separation compared to larger grains (>40 nm) which leads to an increased photocatalytic activity.[40, 43] The catalytic efficiency of *XRD amorphous* TiO_2 is cross-referenced with a commercially available Pilkington Active™ reference TiO_2 catalyst by Eufinger et.al.[40] It is manufactured on a glass substrate with a 15 nm thin-coating of anatase TiO_2.[44] The photocatalytic reaction rate of Pilkington Active™ is measured to be 0.34 ppm/min for ethanol breakdown. In comparison, the *XRD amorphous* TiO_2 reaction rate is measured to be 0.13 ppm/min for the same thickness.[40] The photocatalytic reaction rate for ethanol breakdown increases to 1.3 ppm/min as the deposition thickness increases to 300 nm indicating that the *XRD amorphous* TiO_2 is an effective functional catalyst.[40]

4.5 Summary

Employing CDTS, an increased precision and control of the physical characteristics and properties of multi-sectional, TiO_2-loaded Catalytic Membrane Reactors (CMRs) are achieved. The results presented above show that properties such as the reactor shape and size, pore structure, pore size distribution, and catalyst distribution within the CMR are the parameters that are controlled using CDTS. Careful analysis of the catalyst material with EDS and XPS ensures the cleanliness and correct composition of the TiO_2 catalyst. While the thinness of the catalyst caps prevents the structural characterization of TiO_2 with X-ray diffraction techniques, HR-SEM and TEM identify the catalyst as *XRD amorphous* TiO_2. The described methodology can be extended to other catalysts that can be deposited by PVD,[45] geometries accessible to colloidal assembly,[46] and types of polymer that can be infiltrated and cured.[47]

REFERENCES

1. Dittmeyer, R.; Hollein, V.; Daub, K. *Journal of Molecular Catalysis a-Chemical* **2001,** *173*, 135-184.

2. Stankiewicz, A. *Chemical Engineering and Processing* **2003,** *42*, 137-144.

3. Vankelecom, I. F. J. *Chemical Reviews* **2002,** *102*, 3779-3810.

4. Vankelecom, I. F. J.; Vercruysse, K. A. L.; Neys, P. E.; Tas, D. W. A.; Janssen, K. B. M.; Knops-Gerrits, P. P.; Jacobs, P. A. *Topics in Catalysis* **1998,** *5*, 125-132.

5. Stankiewicz, A. *Chemical Engineering Research & Design* **2006,** *84*, 511-521.

6. Ozdemir, S. S.; Buonomenna, M. G.; Drioli, E. *Applied Catalysis a-General* **2006,** *307*, 167-183.

7. Dixon, A. G. *Int. J. Chem. Reactor Eng.* **2003,** *1*, 1-35.

8. Song, J. H.; Kretzschmar, I. *Langmuir* **2008,** *24*, 10616-10620.

9. Perro, A.; Reculusa, S.; Ravaine, S.; Bourgeat-Lami, E. B.; Duguet, E. *Journal of Materials Chemistry* **2005,** *15*, 3745-3760.

10. Smoukov, S. K.; Gangwal, S.; Marquez, M.; Velev, O. D. *Soft Matter* **2009,** *5*, 1285-1292.

11. Chen, X.; Mao, S. S. *Chemical Reviews* **2007,** *107*, 2891-2959.

12. Feng, B.; Chen, J. Y.; Qi, S. K.; He, L.; Zhao, J. Z.; Zhang, X. D. *Journal of Materials Science-Materials in Medicine* **2002,** *13*, 457-464.

13. Kasemo, B. *Journal of Prosthetic Dentistry* **1983,** *49*, 832-837.

14. Quinn, R. K.; Armstrong, N. R. *Journal of the Electrochemical Society* **1978,** *125*, 1790-1796.

15. Armstrong, N. R.; Quinn, R. K. *Surface Science* **1977,** *67*, 451-468.

16. Li, Y. L.; Ishigaki, T. *Chemistry of Materials* **2001,** *13*, 1577-1584.

17. Chen, G. S.; Lee, C. C.; Niu, H.; Huang, W.; Jann, R.; Schutte, T. *Thin Solid Films* **2008,** *516*, 8473-8478.

18. Giolli, C.; Borgioli, F.; Credi, A.; Di Fabio, A.; Fossati, A.; Miranda, M. M.; Parmeggiani, S.; Rizzi, G.; Scrivani, A.; Troglio, S.; Tolstoguzov, A.; Zoppi, A.; Bardi, U. **2007**, 13-22.

19. Kwon, S.; Fan, M.; Cooper, A. T.; Yang, H. Q. *Critical Reviews in Environmental Science and Technology* **2008,** *38*, 197-226.

20. Carp, O.; Huisman, C. L.; Reller, A. *Progress in Solid State Chemistry* **2004,** *32*, 33-177.

21. Yu, J. C.; Yu, J. G.; Ho, W. K.; Jiang, Z. T.; Zhang, L. Z. *Chemistry of Materials* **2002,** *14*, 3808-3816.

22. Sibu, C. P.; Kumar, S. R.; Mukundan, P.; Warrier, K. G. K. *Chemistry of Materials* **2002,** *14*, 2876-2881.

23. Hong, X. T.; Wang, Z. P.; Cai, W. M.; Lu, F.; Zhang, J.; Yang, Y. Z.; Ma, N.; Liu, Y. J. *Chemistry of Materials* **2005,** *17*, 1548-1552.

24. Zhang, Y. H.; Ebbinghaus, S. G.; Weidenkaff, A.; Kurz, T.; von Nidda, H. A. K.; Klar, P. J.; Gungerich, M.; Reller, A. *Chemistry of Materials* **2003,** *15*, 4028-4033.

25. Prevo, B. G.; Velev, O. D. *Langmuir* **2004,** *20*, 2099-2107.

26. NIST, NIST X-ray Photoelectron Spectroscopy Database. National Institute of Standards and Technology: 2003.

27. Li, S. P.; Qin, Y. J.; Shi, J. H.; Guo, Z. X.; Yongfang, L.; Zhu, D. B. *Chemistry of Materials* **2005,** *17*, 130-135.

28. Pawar, A. B.; Kretzschmar, I. *Langmuir* **2008,** *24*, 355-358.

29. Galuska, A. A.; Uht, J. C.; Marquez, N. *Journal of Vacuum Science & Technology a-Vacuum Surfaces and Films* **1988,** *6*, 110-122.

30. Gonbeau, D.; Guimon, C.; Pfisterguillouzo, G.; Levasseur, A.; Meunier, G.; Dormoy, R. *Surface Science* **1991,** *254*, 81-89.

31. Werfel, F.; Brummer, O. *Physica Scripta* **1983,** *28*, 92-96.

32. Kalyanasundaram, K.; Gratzel, M. *Coordination Chemistry Reviews* **1998,** *177*, 347-414.

33. Love, J. C.; Gates, B. D.; Wolfe, D. B.; Paul, K. E.; Whitesides, G. M. *Nano Letters* **2002,** *2*, 891-894.

34. Gates, B.; Yin, Y. D.; Xia, Y. N. *Chemistry of Materials* **1999,** *11*, 2827-2836.

35. Velev, O. D.; Jede, T. A.; Lobo, R. F.; Lenhoff, A. M. *Chemistry of Materials* **1998,** *10*, 3597-3602.

36. Miller, S.; Berning, G. L. P.; Plank, H.; Roth, J. *Journal of Vacuum Science & Technology a-Vacuum Surfaces and Films* **1997,** *15*, 2029-2034.

37. Arvieu, C.; Manaud, J. P.; Quenisset, J. M. *Journal of Alloys and Compounds* **2004,** *368*, 116-122.

38. Cui, J. Q.; Kretzschmar, I. *Langmuir* **2006,** *22*, 8281-8284.

39. Cahill, D. G.; Allen, T. H. *Applied Physics Letters* **1994,** *65*, 309-311.

40. Eufinger, K.; Poelman, D.; Poelman, H.; De Gryse, R.; Marin, G. B. *Applied Surface Science* **2007,** *254*, 148-152.

41. Dingley, D. J.; Randle, V. *Journal of Materials Science* **1992,** *27*, 4545-4566.

42. Wilkinson, A. J.; Hirsch, P. B. *Micron* **1997,** *28*, 279-308.

43. Nam, H. J.; Amemiya, T.; Murabayashi, M.; Toh, K. *Journal of Physical Chemistry B* **2004,** *108*, 8254-8259.

44. Mills, A.; Lepre, A.; Elliott, N.; Bhopal, S.; Parkin, I. P.; O'Neill, S. A. *Journal of Photochemistry and Photobiology a-Chemistry* **2003,** *160*, 213-224.

45. Mattox, D. M., *Handbook of Physical Vapor Deposition (PVD) Processing: Film Formation, Adhesion, Surface Preparation and Contamination Control*. Noyes Publications: Westwood, NJ, 1998.

46. Zhang, J. H.; Sun, Z. Q.; Yang, B. *Current Opinion in Colloid & Interface Science* **2009,** *14*, 103-114.

47. Li, Q.; Retsch, M.; Wang, J. J.; Knoll, W. G.; Jonas, U., Porous Networks Through Colloidal Templates. In *Templates in Chemistry Iii*, 2009; Vol. 287, pp 135-180.

Chapter 5

Centrifugation-Assisted Particle Templating

5.1 Macroscopic Porous Polymeric Materials

In recent years, the development of macroscopic fabrication techniques for nano- and microscale materials has gained immense interest and attention in the science and engineering community to utilize the unique characteristics of these materials in scaled-up processes.[1-3] Many research efforts are focused on developing and establishing theoretical and experimental connections across these scales to understand the behavior and parameters required for optimal and efficient scale-up.[4] However, establishing and extending the connection from one scale to another has proven to be difficult in experimental settings.[5]

One of the research areas constantly seeking improvement in scalability of nano- and microsystems is the field of porous materials, specifically membrane and scaffold technologies. These technologies utilize the advantage of the increase in surface area-to-volume ratio to promote greater surface interactions for the chosen applications.[6] In addition, the ability to tailor the properties of materials used in the process, i.e., different bulk material, and the controlled porous network are other requirements for these areas of application.

The synthesis of macroscopic, porous materials through centrifugation-assisted particle templating (CAPT) is a promising approach to address scalability of colloidal-templating as a means for large-scale porous material fabrication. Centrifugation has been utilized since the late 1800's as an effective mechanism for many separation processes in areas such as cellular biology and particle technology.[7-11] Utilizing gravitational forces as the main driving force, centrifugation has been applied in particle technology to quickly separate different sizes and types of particles from a suspension.[10, 11] As the rotational speed of the centrifuge is increased, the effective centrifugal forces acting on the particles 'proportionally' increase allowing the particles to sediment away from the center of rotation. As an extension to the separation application, centrifugation in CAPT may further be utilized to control the extent of material infiltration into a packed material.[11] In Chapter 5, *macroscopic* porous polymeric material templating by means of infiltrating dry-packed particles in microcentrifuge (MC) tubes using CAPT is investigated.

5.2 Experimental Details

Materials. Dry polystyrene (PS) particles with a nominal diameter ranging from 200 to 300 μm (250,000 M.W.) were purchased from Polysciences, Inc. Clear Sylgard 184 Silicone Encapsulant, 2-Part Polydimethylsiloxane (PDMS), was purchased from Dow Corning. Ester-terminated Poly(ε-caprolactone) (PCL) was purchased from LACTEL Absorbables. Conical 1.5 mL polypropylene MC tubes were purchased from Fisher Scientific. Biochemical synthesis grade acetonitrile and extra dry AcroSeal 1-Methyl-2-

Pyrrolidone (NMP) were purchased from Acros chemicals. Reagent ACS grade acetone was purchased from Fisher Scientific.

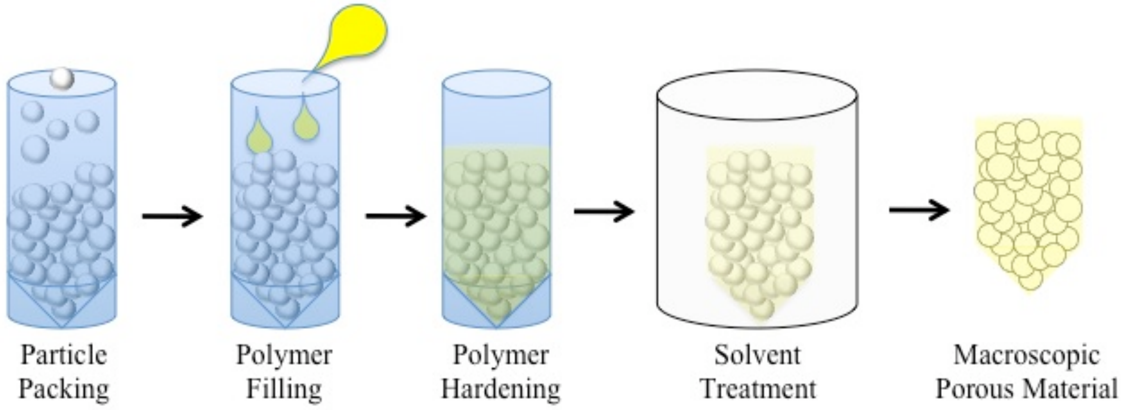

Figure 5.1 Schematic of porous material fabrication technique. From Left to Right: Dry particle packing in microcentrifuge tube; Filling of polymer via centrifugation; Polymer hardening; Solvent treatment to remove particles; Porous material after solvent washing and drying.

Preparation of Macroscopic Biodegradable Porous PCL Material. 1 to 1.5 mL of acetonitrile is pipetted into a glass vial. The solvent is heated to 45 °C and stirred using a Teflon coated magnetic stirrer on a digital stirring hotplate (Fisher). 0.02 ± 0.01 g (Ohaus Balance) of PCL pellets are dissolved/suspended in acetonitrile. The PCL pellets are dissolved into a highly viscous mixture within approximately 20 min. While the PCL solution is being prepared, 1.00 ± 0.05 mL (~1.05g) of PS particles are loosely packed into a MC tube as shown in Figure 5.1. The MC tube containing the particles is tapped from the sides and top to increase the packing density (see below). Next, the viscous polymer solution is poured on top of the packed particles in the MC. The solution-particle matrix is quickly placed into a Minispin MC (Eppendorf). The MC tubes are centrifuged at 13,000 RPM for 1 min to allow the solution to penetrate the interstitial spaces of the packed particles. After centrifugation, the tubes are placed inside a freezer (-13 °C) for approximately 2 to 4 hrs for the PCL to harden. Prior to solvent treatment, excess PCL at the top of the packed particles is removed by cutting with a sharp scalpel. The hardened

PCL/Particle matrix is placed into 15 mL of acetone at -13 °C and stored inside a freezer. The acetone partially dissolves PS and allows the remaining PS to flow out of the matrix. Every 1 to 2 hrs the matrix is taken from the acetone bath to remove the PS residue from the outer surface. Approximately, 10 repeated steps of PS removal are required to obtain the macroscopic, porous PCL material.

Preparation of Macroscopic Porous PDMS Material. 0.5 ± 0.1 g of Sylgard (PDMS) base is placed into a plastic weighing boat. 0.05 ± 0.01 g of curing agent is added to the base and hand-mixed for approximately 5 minutes. The mixture is placed into a vacuum desiccator connected to a diaphragm pump. The vacuum chamber is allowed to pump on the desiccator for approximately 20 mins to extract air bubbles trapped inside the clear PDMS mixture. While the air bubble extraction is underway, 1.00 ± 0.05 mL (~1.05g) of PS particles are loosely packed into a MC tube as shown in Figure 5.1. The MC tube containing the particles is tapped from the sides and top to increase the packing density. Once all air bubbles have been removed from the PDMS mixture, the mixture is pipetted into the MC tube with the packed particles. The PDMS/particle matrix is centrifuged at a specific RPM (0, 1000, or 2000) in the MC for 2 mins. The PDMS-infiltrated packed particles are placed in an oven where the PDMS network is allowed to harden for 2 to 4 hrs. As in the PCL procedure, excess PDMS at the top of the packed particles is removed using a sharp scalpel. The hardened PDMS/particle matrix is placed in 10 to 15 mL of NMP at room temperature. NMP dissolves the PS particles embedded in the matrix with minimal swelling of the PDMS. The NMP bath is exchanged every 4 to 6 hrs to ensure the fastest rate of PS dissolution. The step is repeated 3 to 4 times to result in the macroscopic porous PDMS material. The NMP treatment is followed by repeated washes with acetone to ensure complete removal of the PS and NMP from the porous PDMS structure.

Imaging. Prior to imaging, both porous materials are placed in an evacuated desiccator for 30 mins to ensure complete removal of the solvents used during washing. To ensure quickest solvent removal and reduce uneven drying caused by surface interactions between the porous materials and the supporting surface, the macroscopic porous materials are placed on two parallel glass rods that have been fixed at a specific distance to each other using a tape. After complete drying, scanning electron microscope (SEM) images are obtained using the Carl Zeiss EVO 40 equipped with variable-pressure (VP) mode. The accelerating voltage used ranges from 10 – 13 kV with chamber pressures ranging from 35 to 45 Pa.

5.3 Characterization of Macroscopic Porous PCL & PDMS

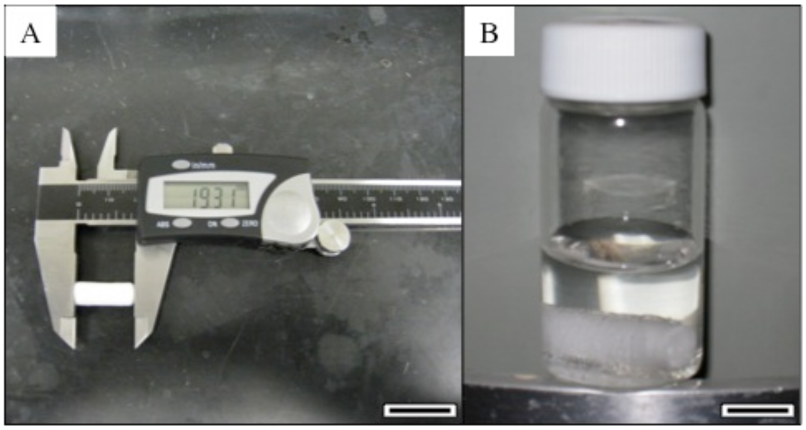

Figure 5.2 Photographs of PCL/particle matrix. (A) PCL/particle matrix after removal of the MC tube. Scale bar 2 cm. (B) Hardened PCL/particle matrix after 2 hours of soaking in acetone at -13 °C. Scale bar 1 cm.

PCL Macroscopic Porous Material. A hardened PCL/particle matrix with a cylindrical geometry having an outer diameter equivalent to the inner diameter of the MC tube results when PCL is infiltrated into the dry particle packing at 13,000 RPM. Figure

5.2A shows an image of the templated PCL/particle matrix immediately after the MC tube is removed. The nominal length of the matrix including the excess PCL at the top is measured to be 19 ± 3 mm using a digital caliper. The matrix depicted in Figure 5.2A is uniformly colored and shaped throughout its length. The image in Figure 5.2B shows the PCL/particle matrix after 2 hrs of acetone treatment inside a glass vial at -13 °C. The PS slowly starts to flow out of the PCL/particle matrix surface owing to the dissolving effect of the acetone on polystyrene. Surface pores are not visible at the scale of the images in Figure 5.2.

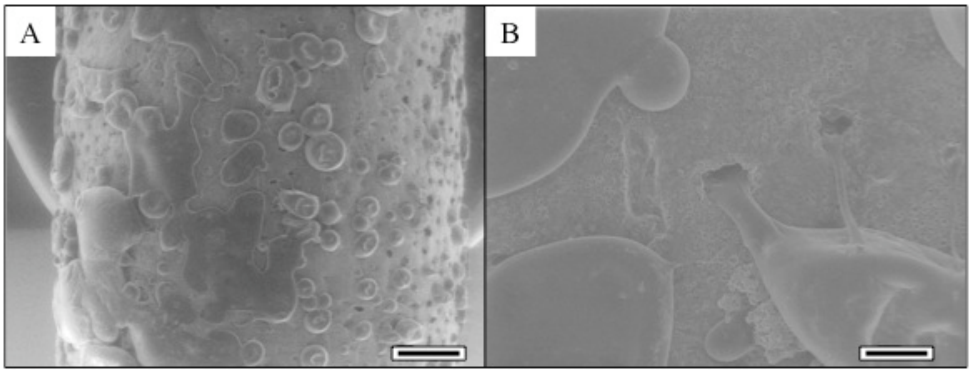

Figure 5.3 SEM images of PCL/particle matrix after 2 hr treatment. (A) Large-scale view of the matrix. Scale bar 1000 µm. (B) Higher magnification of a porous region. Scale bar 200 µm.

The local effect of acetone treatment at low temperatures is shown in Figure 5.3. Figure 5.3A shows an SEM image of the PCL surface where the PS has sipped through the surface pores and hardened as the acetone evaporated from the PCL material during preparation for imaging. The flowing PS is frozen into globules on the surface of the PCL. Figure 5.3B depicts a higher resolution image of pores in the PCL surface. It is evident from Figure 5.3B that the PS flows out of the pores when treated in acetone. The excess of PS collecting at the bottom of the glass vial is removed and weighed yielding approximately 0.20 ± 0.04 g indicative of a 40% removal of embedded PS from the matrix after 2 hours.

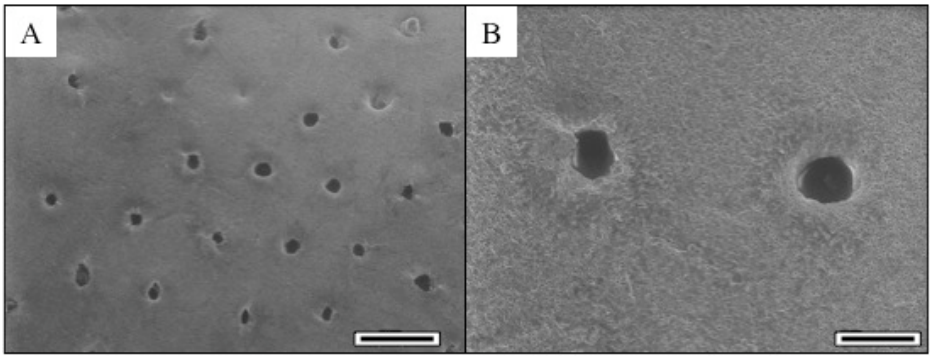

Figure 5.4 SEM images of porous PCL surface after 24 hrs of acetone treatment. (A) Large-scale view of the PCL surface. Scale bar 300 µm. (B) Higher magnification of two pores. Scale bar 100 µm.

Figure 5.4 shows two higher magnification SEM images of the PCL/particle matrix shown in Figure 5.3 after an additional 22 hrs of acetone treatment at -13 °C. More prevalent surface pores are visible in Figure 5.4A. The average surface pores measured are 64 ± 17 µm in diameter calculated using measurements from 30 different surface pores. Some surface pores have not been formed, yet, due to residual PS left in the matrix. Figure 5.4B shows two pores separated by approximately 300 µm. The left and right pores are measured to be 50 and 67 µm, respectively. A rough surface morphology of the PCL around the two pores is visible at this magnification.

Radially-sliced macroscopic porous PCL material (Figure 5.5) is imaged using SEM to investigate the internal pore structure. Owing to the mechanical properties of PCL, the outer surface of the PCL has been deformed inward around the edge of the material cross section (bottom of image) and appears to have been smeared across the cross section during cutting. As a result, indentations from the templating particles are barely visible in the image. However, residual interconnecting pores formed by neighboring particles can be identified throughout the cross section in Figure 5.5 and are measured to be on average 56 ± 16 µm in diameter.

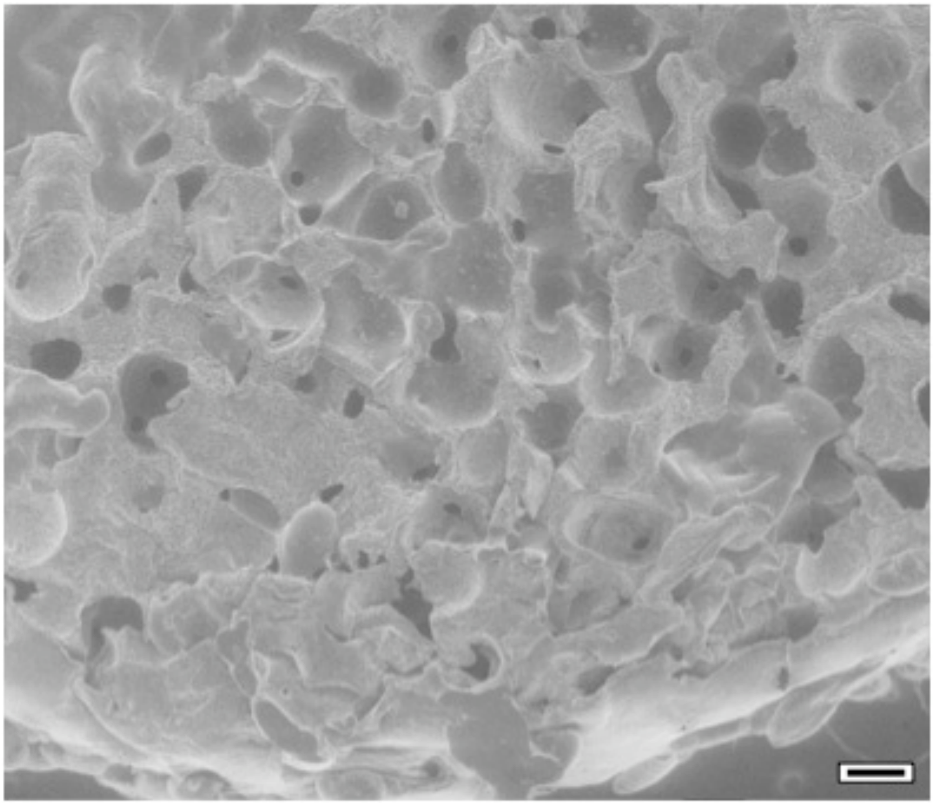

Figure 5.5 SEM images of radially-sliced macroscopic, porous PCL after 24 hr acetone treatment. Scale bar 200 µm.

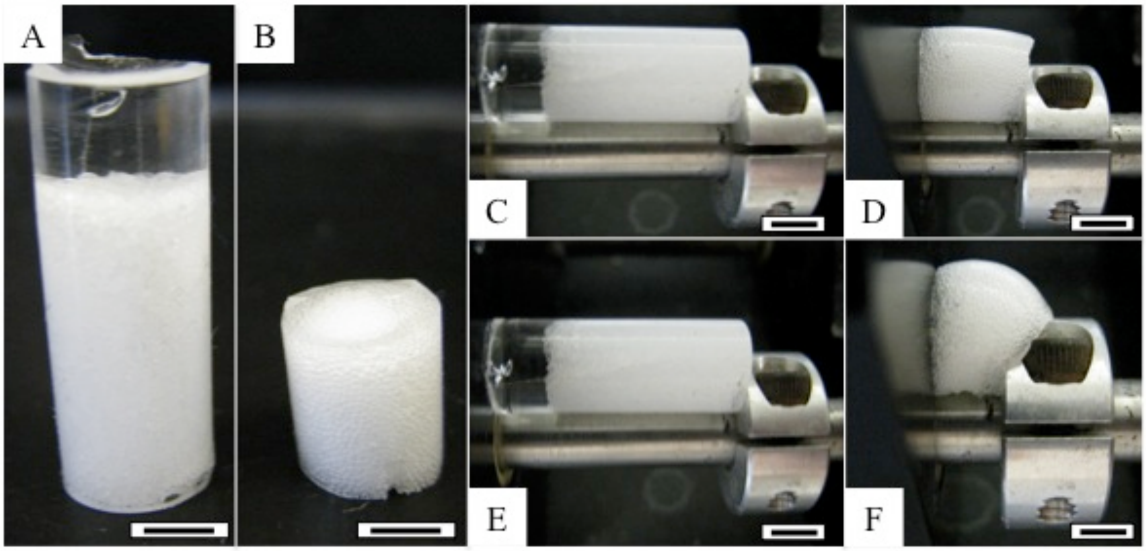

Figure 5.6 Photographs of PDMS/particle matrix and macroscopic porous PDMS material. (A) PDMS/particle matrix after removal from MC tube. (B) Sliced macroscopic porous PDMS material. (C) Uncompressed PDMS/particle matrix. (D) Uncompressed macroscopic porous PDMS material. (E) Compressed PDMS/particle matrix. (F) Compressed macroscopic porous PDMS material. Note, force applied in (E) and (F) are identical (see text). All scale bars approximately 1 cm.

PDMS Macroscopic, Porous Material. Similar to the macroscopic, porous PCL material discussed in the previous section, templated macroscopic, porous PDMS material with an opaque cylindrical shape results from MC tube templating as depicted in Figures 5.6 A and B. The optically transparent nature of the bulk PDMS (clear polymer at the top of Figure 5.6A) is masked by refractive interference brought on by the embedded particles (bottom of Figure 5.6A) and pore formation (Figure 5.6B). In addition, the presence of interconnecting pores in the PDMS templated by the packed particles gives the macroscopic, porous PDMS material a *spongy* character allowing the compression of the porous PDMS material as shown in Figures 5.6D (uncompressed) and 5.6F (compressed). In contrast to the compressible porous PDMS material, the PDMS/particle matrix cannot be compressed visibly as shown in Figures 5.6C (uncompressed) and 5.6E (*compressed*) when the same force is applied.

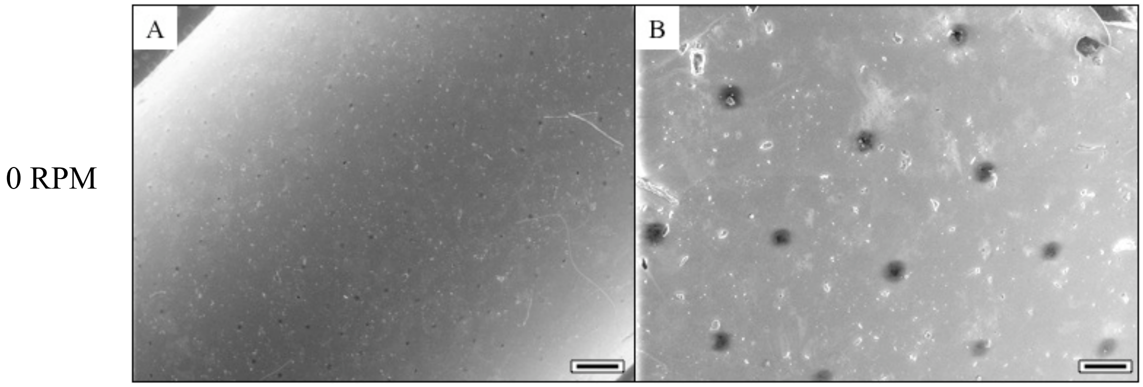

Figure 5.7 SEM images of the porous PDMS surface obtained by gravitationally infiltration (GI) at 0 RPM and 24 hr treatment in NMP. (A) Large-scale view of the surface. Scale bar 500 µm. (B) Higher magnification of surface pores. Scale bar 100 µm.

Gravitationally-infiltrated (GI), porous PDMS material templated using PS particles is shown in Figure 5.7. The GI-PDMS material shows pores on the entire length of the surface with a nominal pore size diameter of 37.5 ± 12.5 µm. Figure 5.7A shows a low magnification image with surface pores present. White lines and spots are artifacts introduced to the system as a result of material handling. The higher resolution image in Figure 5.7B reveals pores that are spaced approximately 300 ± 19 μm apart in good agreement with the size of the particles utilized as templates.

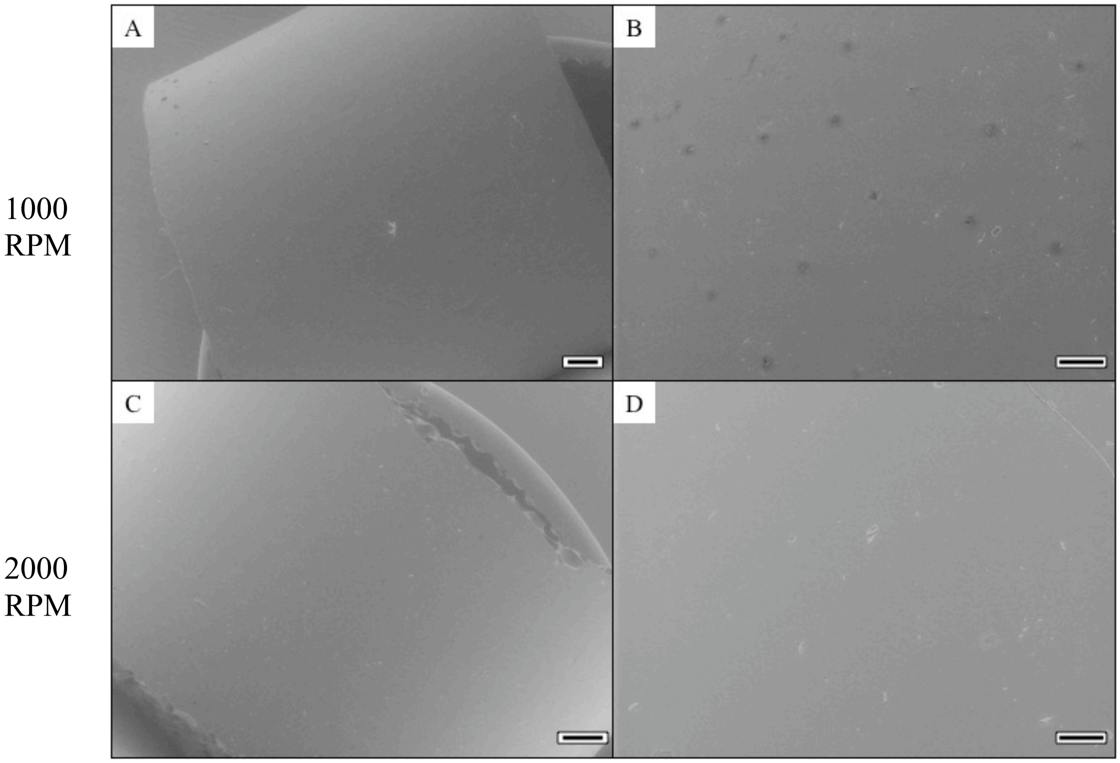

Figure 5.8 SEM images of the surface of macroscopic, porous PDMS materials obtained with centrifugation at varying RPMs after 24 hr NMP treatment. (A) Large-scale view of the surface fabricated using 1000 RPM. Scale bar 500 μm. (B) Higher magnification of surface pores from Figure A. Scale bar 200 μm. (C) Large-scale view of the surface fabricated using 2000 RPM. Scale bar 500 μm. (D) Higher magnification of pore-free surface from Figure C. Scale bar 150 μm.

The effect of centrifugation on the surface pore formation is shown in Figure 5.8. Figures 5.8 A and B show the images of surface pores fabricated via centrifugation-enhanced infiltration of uncured PDMS into packed particles in MC tubes at 1000 RPM. A smaller number of surface pores is observed in comparison to the porous GI-PDMS material in Figure 5.7. In addition, the average distance between the neighboring pores has increased to 386 ± 159 μm with an average pore size of approximately 30.2 ± 5.5 μm in diameter. In Figures 5.8 C and D, the surface of the porous PDMS material shows limited to no pores when uncured PDMS is infiltrated at 2000 RPM.

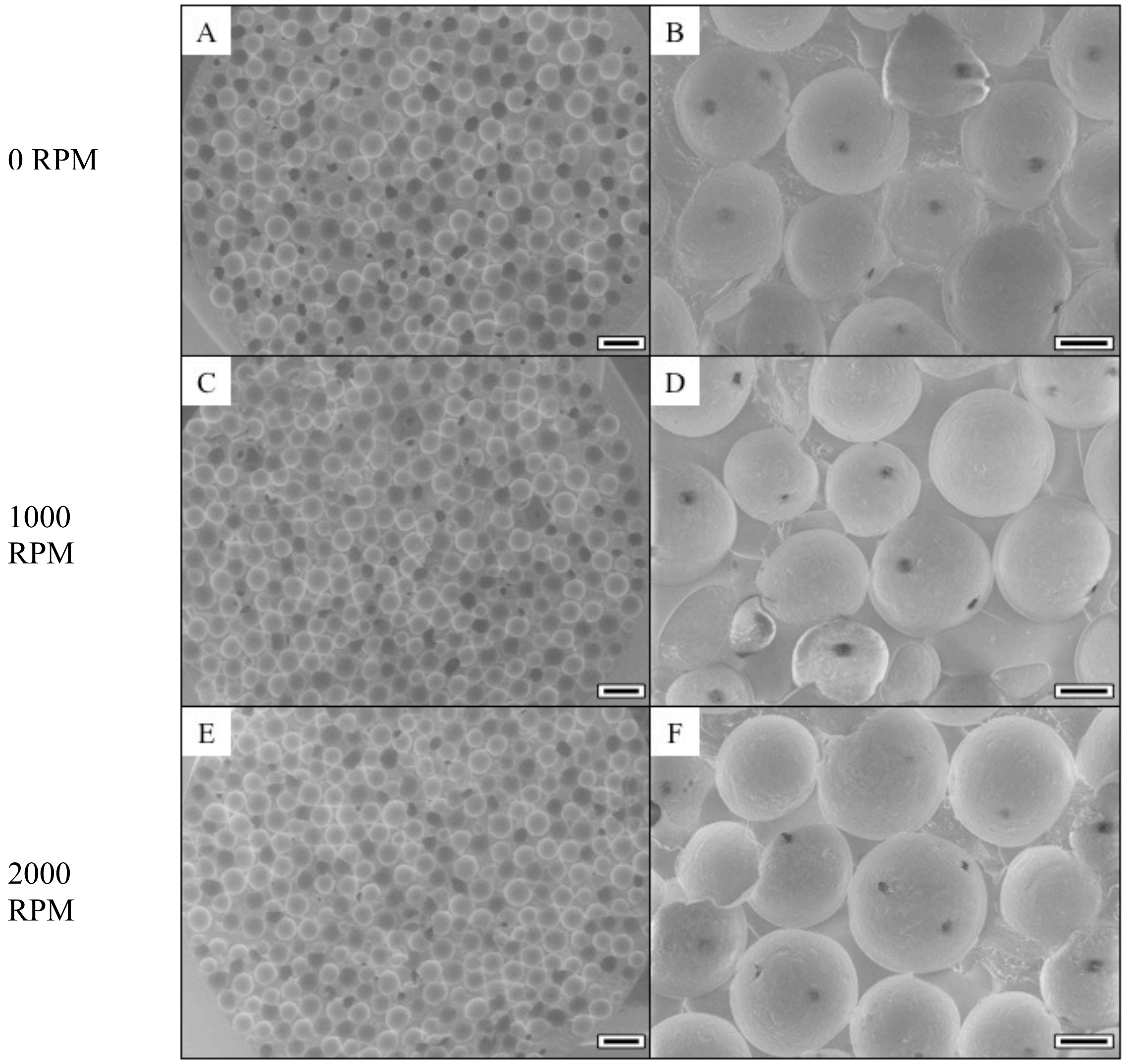

Figure 5.9 SEM images of porous PDMS cross-sections after 24 hr NMP treatment. (A) Large-scale view of the cross-sectional image of GI material. Scale bar 500 µm. (B) Higher magnification of pores from Figure A. Scale bar 150 µm. (C) Large-scale view of the cross-sectional image of porous PDMS material centrifuged at 1000 RPM. Scale bar 500 µm. (D) Higher magnification of pores from Figure C. Scale bar 150 µm. (E) Large-scale view of the cross-sectional image of porous PDMS material centrifuged at 2000 RPM. Scale bar 500 µm. (F) Higher magnification of pores from Figure E. Scale bar 150 µm.

The internal pore structure of porous PDMS materials fabricated at 0, 1000, and 2000 RPM is revealed in Figure 5.9. Figures 5.9 A, C, and E are large-scale images of the 0, 1000, and 2000 RPM materials, respectively. Across all images, a consistent pore structure templated by loosely packed PS particles with randomly arranged spherical pores is observed. The variance in the sizes of the spherical pores is attributed to the position of the cross-sectional cut and the particle size distribution as observed in the corresponding higher magnification images in Figures 5.9 B, D, and F.

Between 15 to 17 completely and partially spherical pores are shown in the higher magnification images with a constant scan area of 1125 µm by 1500 µm. The size of the interconnecting pores formed between particles is measured in a number of scanned images to elucidate the effect of RPM on interconnecting pore sizes. The interconnecting pore sizes of the 0, 1000, and 2000 RPM centrifuged materials are determined to be 15.5 ± 13.7 µm, 11.3 ± 12.0 µm, 21.6 ± 11.3 µm, respectively. Each pore size measurement is the result of averaging 30 to 45 pore size measurements at the center of the respective macroscopic, porous materials.

5.4 Discussion

Centrifugation-assisted particle templating (CAPT) enables expeditious fabrication of macroscopic porous materials with the ability to tailor various characteristics and properties including dimensions, bulk material, and pore sizes. In the following, the synthesis process and structural characterization of macroscopic porous PCL and PDMS materials are discussed.

Prior to the start of the synthesis process for macroscopic porous materials, suitable complementary bulk and templating materials must be determined based on the chemical and physical requirements of the application. For the potential application in scaffold and separations engineering, the optimal materials to use are PCL (Poly(ε-caprolactone)) and

PDMS (Polydimethylsiloxane), respectively. PCL is an U.S. FDA (Food and Drug Administration) approved biodegradable material with an excellent biocompatibility allowing minimal chemical, physical, and biological interferences and a multitude of tissue engineering applications.[12] For separations, PDMS is chosen for its low material cost in conjunction with the desired chemical inertness and physical characteristic.[13, 14]

Dry, spherical PS particles are a complementary templating material to be employed for both bulk materials. PS particles are resistant to acetonitrile when it is required during the dissolve/suspend of PCL at 45 °C and are unaffected by the base and the curing agent encountered during PDMS preparation. Further, acetone and NMP used for the removal of the PS template from the bulk PCL and PDMS specimens, respectively, do not react with the respective bulk materials resulting in macroscopic porous PCL and PDMS materials.

Once compatible materials have been determined, dry particle packing and bulk material infiltration characteristics must be understood. The packing characteristics of particles in cylindrical confinement have been of keen interest to the chromatography community especially in the application of High-Performance Liquid Chromatography (HPLC).[15-17] Packing of dry particles in a cylindrical confinement has been extensively studied in various simulations and experiments with respect to the aspect ratio dependence reviewed in Chapter 2. Applying the understandings from earlier studies, the particle packing used in the preparation of macroscopic porous material is predicted to be random for an MC tube diameter *(D)*-to-particle diameter *(d)* ratio of 40 to 1. In addition, random packing of particles is promoted due to the wide particle size distribution with a large number of particles in the diameter range of 200 to 300 μm. The spherical imprints in the cross sections (Figures 5.5 and 5.9) show a wide range confirming the large particle size distribution of the templating particles.

Surface and interconnecting pores resulting from the CAPT process are another set of characteristics that define the properties of the macroscopic, porous materials. Both materials discussed in this study are made by processes utilizing centrifugation as the means for infiltration of the bulk material into the interstitial spaces of the packed particles subsequently affecting the pore formation. The effective centrifugal force or gravity (g) must be understood to correlate pore formation and size to the rotational speed of the centrifuge.

$$LF = \frac{(2\pi N)^2}{r} \tag{5.1}$$

Equation 5.1 correlates the effective centrifugal force in gravity to the RPM of the centrifuge. LF is the effective centrifugal force, N is the RPM used, and r is the radius of the centrifuge.

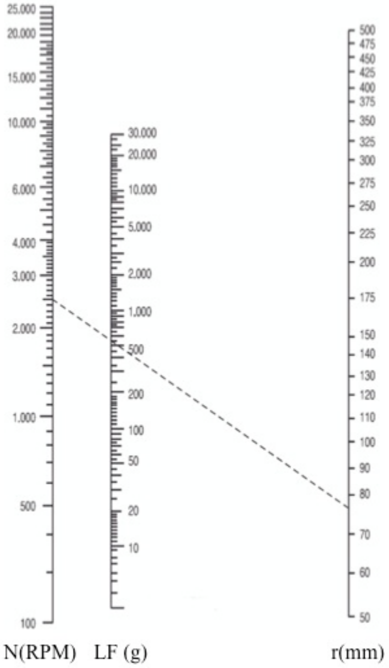

Figure 5.10 Nomograph – a correlation graph linking RPM and effective centrifugal force.

Utilizing Equation 5.1, the Nomograph (a correlation graph) is charted in Figure 5.10. For the macroscopic porous PCL material, viscous PCL solution is poured on top of the packed particles and centrifuged at 13,000 RPM. The effective centrifugal force is determined to be 11,356 gravitational force (g) using the Nomograph and the centrifuge radius of 60 mm. The surface and interconnecting pore sizes obtained with this effective centrifugal force are measured to be 64 ± 17 and 56 ± 16 μm in diameter, respectively. The surface pore sizes are larger in comparison to the interconnecting pores confirming previously reported findings.[6, 18] The effect of varying the centrifugal force on the pore sizes can be observed in the experiments with the macroscopic porous PDMS material. The RPM is varied from 0 to 1000 to 2000 RPM resulting in centrifugal forces of 1 g, 56 g, and 224 g, respectively. Although the pore sizes of the interconnecting pores remain relatively consistent with increasing RPM, the surface pores of the porous PDMS material obtained with centrifugation at higher RPMs diminish with increasing RPM as observed in Figures 5.7 and 5.8 leading to a completely enclosed porous material at 2000 RPM. The difference in effective centrifugal forces needed for infiltration of PCL and PDMS is attributed to the materials characteristics of the infiltrating polymer and solvent interactions in the system. For PCL, the viscosity of the infiltrating suspension is high due to the low amount of acetonitrile used and therefore requires a higher effective centrifugal force (i.e., 11,356 g) to achieve infiltration and formation of the macroscopic material. In comparison, the infiltrating PDMS mixture has a lower viscosity than the PCL mixture and infiltrates the packed PS particles at much lower effective centrifugal forces. Two factors are responsible for the complete encasement at 2000 RPM. The lower viscosity in the PDMS system leads to the quick infiltration by the PDMS polymer. In addition, the lower density of the PDMS compared to PS (ρ_{PDMS} = 0.84 g/cm^3 vs. ρ_{PS} = 1.05g/cm^3)[19] allows a phase separation leading to particle sedimentation at the bottom of the MC tube. In the case of PCL, much higher centrifugal forces is needed for the infiltration due to higher observed viscosity, however, the higher density of PCL (1.15 g/cm^3)[20], in comparison to PS, prohibits the complete enclosure even at higher centrifugal forces complete enclosure is not expected.

Lastly, to ensure the transport of the solvent during the PS dissolution process especially in the case of the completely enclosed PDMS system, the excess bulk polymer from the top of the respective polymer/particle matrices is removed exposing a region with embedded particles on both ends of the materials to the respective solvents. This process is further enhanced by the swelling of PDMS in NMP. The PDMS swelling allows the NMP to penetrate the outer PDMS layer and reach the PS particles for dissolution. The swelling of the PDMS also facilitates the solvent-induced flow of the polystyrene out of the polymer/particle matrix. Once the washing is completed, the macroscopic porous PDMS material is placed in an evacuated desiccator, where excess solvent is removed leading to contraction of the PDMS material to its original dimensions given by the inner shape of the MC tube.

5.5 Summary

Employing the CAPT technique allows an expedited fabrication of macroscopic porous materials with tailored bulk materials and pore sizes. We have shown that utilizing a combination of complementary materials macroscopic porous materials can be synthesized in a timely fashion using centrifugation. In addition, the effect of centrifugation on surface and interconnecting pore sizes has been explored and shows that surface pore size decreases with increasing RPM, while interconnecting pore size and number are not affected. The described methodology can be extended to other geometries, bulk materials, and complementary materials to fabricated macroscopic porous materials for new applications.

REFERENCES

1. Hammond, P. T. *Advanced Materials* **2004,** *16*, 1271-1293.

2. Shimomura, M.; Sawadaishi, T. *Current Opinion in Colloid & Interface Science* **2001,** *6*, 11-16.

3. Ikkala, O.; ten Brinke, G. *Chemical Communications* **2004**, 2131-2137.

4. Graham-Brady, L. L.; Arwade, S. R.; Corr, D. J.; Gutierrez, M. A.; Breysse, D.; Grigoriu, M.; Zabaras, N. *Probabilistic Engineering Mechanics* **2006,** *21*, 193-199.

5. Garcia, R.; Martinez, R. V.; Martinez, J. *Chemical Society Reviews* **2006,** *35*, 29-38.

6. Xia, Y. N.; Gates, B.; Yin, Y. D.; Lu, Y. *Advanced Materials* **2000,** *12*, 693-713.

7. Beams, J. W. *Reviews of Modern Physics* **1938,** *10*, 0245-0263.

8. Schneider, W. C.; Hogeboom, G. H. *Cancer Research* **1951,** *11*, 1-22.

9. Waage, E. V.; Rabinovi.Bs. *Chemical Reviews* **1970,** *70*, 377-387.

10. Sharma, V.; Park, K.; Srinivasarao, M. *Materials Science & Engineering R-Reports* **2009,** *65*, 1-38.

11. Philipse, A. P. *Current Opinion in Colloid & Interface Science* **1997,** *2*, 200-206.

12. Thomas, V.; Dean, D. R.; Vohra, Y. K. *Current Nanoscience* **2006,** *2*, 155-177.

13. Vankelecom, I. F. J. *Chemical Reviews* **2002,** *102*, 3779-3810.

14. Ulbricht, M. *Polymer* **2006,** *47*, 2217-2262.

15. Jung, S.; Ehlert, S.; Mora, J. A.; Kraiczek, K.; Dittmann, M.; Rozing, G. P.; Tallarek, U. *Journal of Chromatography A* **2009,** *1216*, 264-273.

16. Ehlert, S.; Roesler, T.; Tallarek, U. *Journal of Separation Science* **2008,** *31*, 1719-1728.

17. Muller, C. R.; Holland, D. J.; Sederman, A. J.; Mantle, M. D.; Gladden, L. F.; Davidson, J. F. In *Magnetic Resonance Imaging of fluidized beds*, 2008; pp 53-62.

18. Jiang, P.; Hwang, K. S.; Mittleman, D. M.; Bertone, J. F.; Colvin, V. L. *Journal of the American Chemical Society* **1999,** *121*, 11630-11637.

19. Cui, J. Q.; Kretzschmar, I. *Langmuir* **2006,** *22*, 8281-8284.

20. Marrazzo, C.; Di Maio, E.; Iannace, S.; Nicolais, L. *J. Cell. Plast.* **2008,** *44*, 37-52.

Chapter 6

Towards Designer Photonic Crystals

6.1 Photonic Crystals

The field of *Photonics* was introduced to the science community in the late 1960's with the intent to use light to perform traditional operations that fell within the domain of electronics. Unlike traditional electronics, photonics operations offer significant advantages including speed (speed of light vs. electrons), multiplicity (increased wavelengths), and no electromagnetic interference. Modern photonics investigates the development of photonic materials to harvest, control, and implement these favorable characteristics in many fundamental and technological applications.

The term, Photonic Materials or Crystals (PhC), refers to a class of macroscopic materials in a periodic arrangement with different dielectric constants that affect the propagation of electromagnetic waves (EM) through the material.[1, 2] In such a case where the emission source is located inside the PhC, the spontaneous emission of light can be altered through the PhC environment leading to a modification of the radiative decay rates. In the Wigner-Weiskopf approximation, the radiative decay rate is described by Fermi's golden rule that takes into account the local density of states (LDOS). LDOS is the number of electromagnetic modes available at a specific location of the emitter into which photons can be emitted. A PhC presents a *bandgap* in which photons of specific frequencies are not allowed to propagate in certain directions.[3, 4] Consequently an emission with a frequency that lies in the bandgap will have a smaller number of allowed photon modes to decay into, leading to a modification of the decay rate. While control of spontaneous emission has been observed in one (1D) and two-dimensional (2D) PhCs, the effect of such a modification is expected to be the largest in three-dimensional (3D) systems (Figure 6.1). The control of spontaneous emission in a 3D system is essential for a variety of applications including miniature lasers, light emitting diodes,[5, 6] single photon sources for quantum information,[7, 8] and solar energy harvesting.[9]

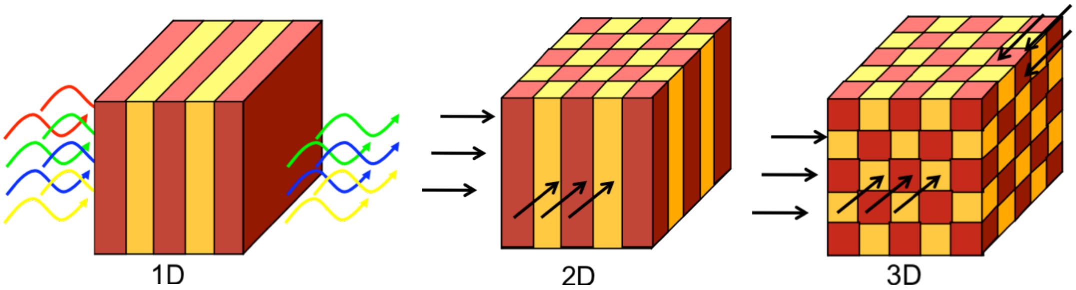

Figure 6.1 Schematic representation of the 1D, 2D, and 3D periodic structures with respective directional photonic modification.

In Chapter 6, the preliminary work on designer 3D photonic materials based on colloidal assembly is presented. This work is a collaborative project with Mr. Harish Natarajan and Professor Vinod Menon at Queens College.[10] The first section summaries the work completed on 3D planar fluorescent colloidal assemblies with emphasis on the fabrication technique and photonic characterization to understand the effect of an ordered structure on the spontaneous emission. The subsequent section describes the preliminary work performed on the fabrication of multi-sectional *fluorescent* 3D colloidal assemblies in cylindrical microcapillaries. Last but not least, magnetically-enhanced colloids are introduced as possible building blocks for future designer photonic crystals.

6.2 Fluorescent 3D Planar Colloidal Assembly

6.2.1 Experimental Details

Materials. Red fluorescent (300 nm) and green fluorescent (500 nm) polystyrene (PS) suspensions were purchased from Duke Scientific. Mechanical grade (100) silicon wafers were purchased from University Wafer.

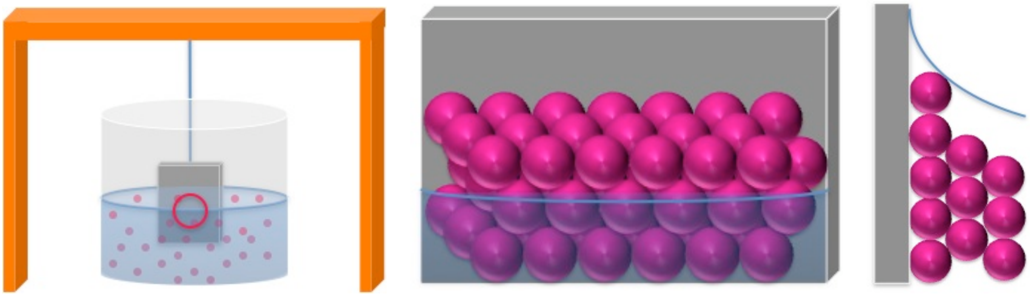

Figure 6.2 Schematic of the fluorescent 3D planar colloidal assembly. (Left) Assembly setup; (Center) Front view of the assembly indicated by the red-circled area in the set up schematic; (Right) Cross-sectional view of the assembly.

Fluorescent 3D Planar Colloidal Assembly. Excess surfactant is extracted from the stock solution through washing of the colloidal suspension. 1 mL of fluorescent colloidal solution of 1% (w/v) is removed from the stock solution into a microcentrifuge (MC) tube with 1.5 mL of de-ionized (DI) water. The diluted solution is ultra-sonicated for 5 mins followed by centrifugation at 13,000 RPM for 5 to 10 mins in a MC (Eppendorf) to sediment the colloids from the solution. Once the sedimentation is confirmed, the supernatant is extracted from the MC tube. The washing procedure is repeated *three times* to obtain a 1% (w/v) concentration of the colloidal solution. The prepared colloidal solution is transferred to a PMMA vessel where additional DI water is added to formulate 3 mL of a 0.3% (w/v) concentrated solution. An acid-cleaned silicon wafer is positioned at the center of the solution for the convective assembly of colloids onto the silicon wafer

(Figure 6.2). The solution is placed into an oven at 50 to 70 °C to accelerate the drying and assembly process.

Reflectivity and Fluorescent Measurements. Angle-resolved reflectivity measurements are carried out to determine the band structure of the 3D assemblies. Light from a halogen white light source is shone onto the colloidal assembly. The reflected light is collected by a CCD-based fiber-coupled spectrometer (Ocean Optics). The steady-state and time-resolved photoluminescence (PL) spectra of the fluorescent colloids, extracted dye, colloidal assemblies, and crushed assemblies are obtained using Fluoromax3 (Horiba) with a monochromatic mercury light source and a monochromator. Both setups utilized in the measurements are shown in Figure 6.3.

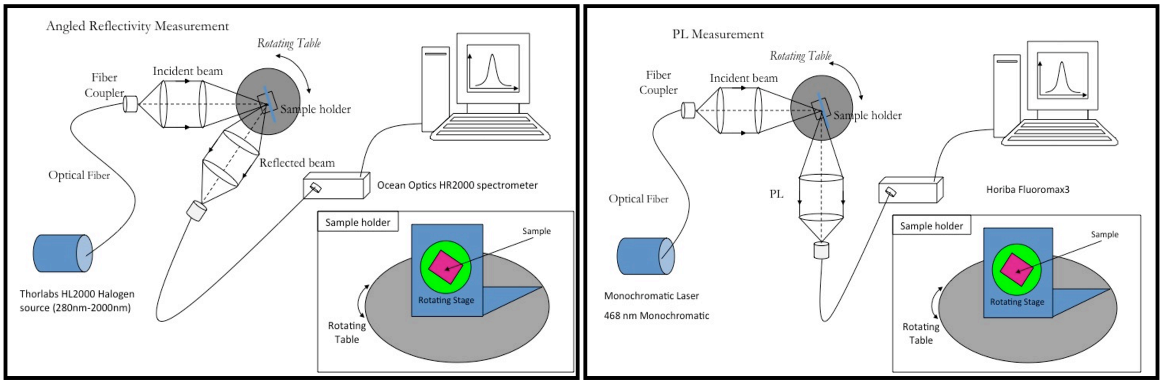

Figure 6.3 Schematic representations of Reflectivity and Fluorescence measurement setups. (Left) The optical fiber for collection is positioned at a desired angle for measurement. (Right) Fluorescence measurement is performed at a 90° angle.

6.2.2 Results and Discussion

Approximately 2 to 4 hours of drying of the colloidal solution in the oven allows formation of 3D colloidal assemblies. Figure 6.4 shows Scanning Electron Microscope (SEM) images of fluorescent 300 and 500 nm planar 3D colloidal assemblies dried at 70 and 50 °C, respectively. Figures 6.3 A and B depict top and cross-sectional views of the fluorescent 300 nm particle planar assembly. Cross section of the assembly is obtained

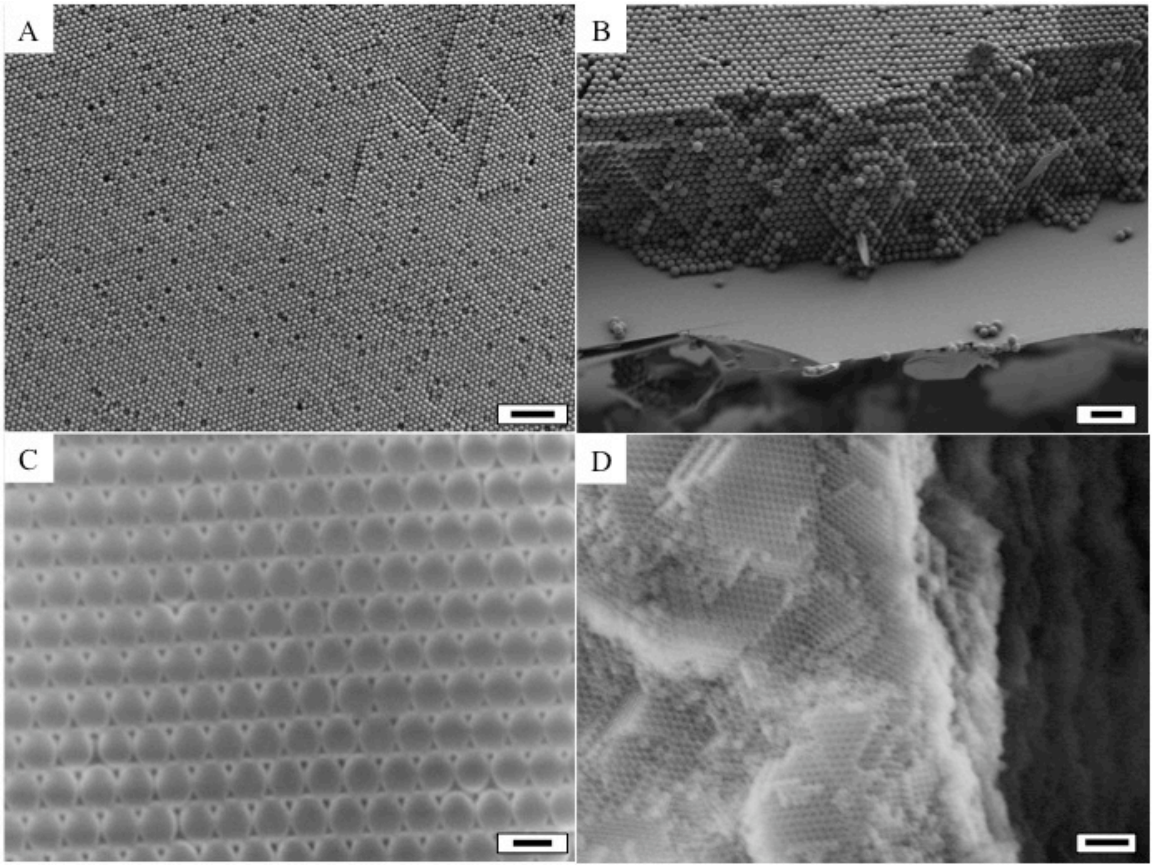

Figure 6.4 Scanning Electron Microscope (SEM) images of 300 nm red fluorescent and 500 nm green fluorescent colloidal assemblies or PhCs. (A) High-resolution SEM image of 300 nm particle assembly from the top. Scale bar 2 μm. (B) Cross-sectional image of 300 nm particle assembly. Scale bar 1 μm. (C) High-resolution cross-sectional SEM image of 500 nm particle assembly. Scale bar 0.5 μm. (D) SEM image of 500 nm particle assembly from the top. Scale bar 2 μm.

by cleaving the silicon substrate. From the images, a uniform face centered cubic (FCC) close-packed arrangement of colloids is observed giving rise to the desired photonic properties. In addition, point defects and grain boundaries are visible in the images. Figures 6.4 C and D show high-resolution and cross-sectional SEM images of fluorescent 500 nm planar colloidal assemblies or PhCs. Similar to Figures 6.4 A and B, both images show the (111) plane of an FCC close-packed arrangement. The cross-sectional image in Figure 6.4D is taken by stamping the colloidal assembly onto a double-sided conducting tape. fewer defects are observed in the 500 nm particle assembly likely due to the lower temperature used during drying. A lower drying temperature results in a slower drying rate allowing increased order.[11-14] However, a balance of time and desired quality of colloidal assembly must be considered for optimal result.

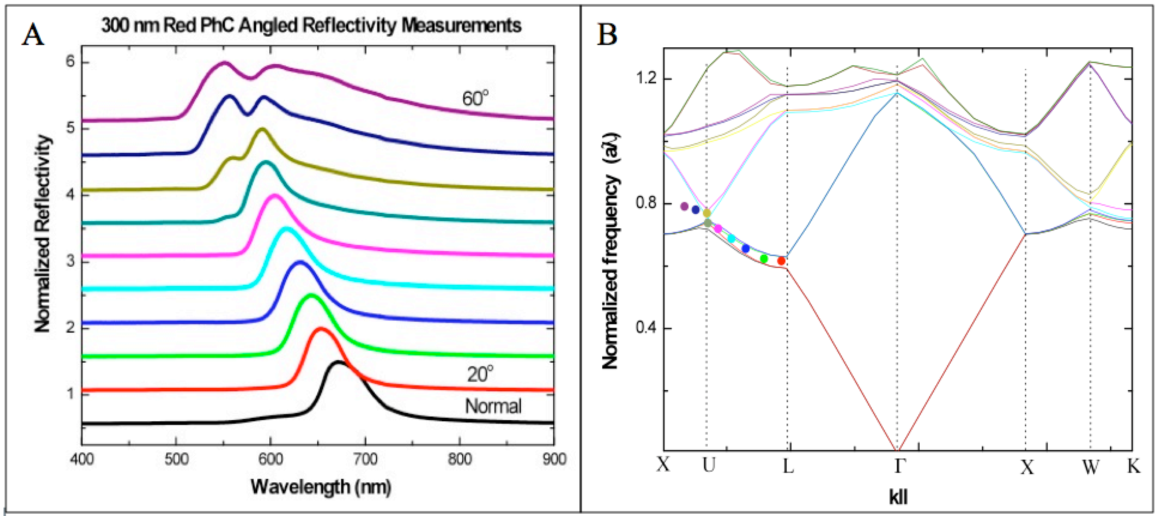

Figure 6.5 Reflectivity data of 300 nm red fluorescent colloidal PhC. (A) Experimental angle-resolved reflectivity data – Measurements are shifted by 0.5 increments in the y direction for clarification and show 5° angle increments from 20 to 60°. (B) Calculated band structure of the PhC using Plane Wave Expansion.

Angle-resolved reflectivity measurements are performed on the fabricated colloidal PhCs to determine the band structure or band gaps as shown in Figure 6.5A. In addition, Rsoft Bandsolve is employed to confirm the experimentally obtained values by comparison to the simulated band structure shown in Figure 6.5B. Rsoft Bandsolve utilizes the plane wave expansion method to solve the *master equation* based on Maxwell's equations for the simulated band structure. The ΓL direction in Figure 6.5B corresponds to normal incidence and increasing the angle of incidence corresponds to varying $k_{||}$ from the L to the U point of the Brillouin zone.[4] Peaks in the experimental data correspond to photon energies, which are not allowed to exist within the PhC. At normal incidence, the peak is at 670 nm. The peak moves to higher energies (lower wavelengths) as the angle of incidence is increased in accordance with the shift to higher frequencies in the simulated dispersion diagram. As the angle of incidence approaches 45°, a second peak develops in the reflectivity measurements. The second peaks is caused by Bragg diffraction from the (200) plane and occurs when $k_{||}$ approaches the U point of the Brillouin zone.[15] The colored circles in the simulated data represent the corresponding reflectivity peak maximum for the various angles. It can be seen that there is an excellent agreement between the reflectivity peaks obtained from experiment and the partial bandgap predicted by the simulated band structure.

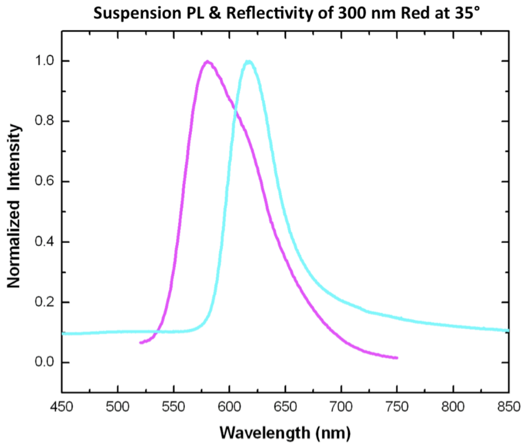

Figure 6.6 Overlay of photoluminescence trace from red 300 nm colloidal solution (purple line) and the reflectivity measurement performed on the 300 nm colloidal PhC at a 35° angle (blue line).

The steady-state PL spectrum of the red 300 nm colloidal solution and the reflectivity from the 300 nm colloidal PhC sample at an angle of incidence of 35^o are shown in Figure 6.6. It is evident that the fluorescent dye, which is sitting inside the colloids, has a very broad emission spectrum (550 – 650 nm) compared to the width of the PhC reflectivity (575 – 660 nm) at a normalized intensity of 0.3. An overlapping region between the PL spectrum and the photonic band structure is observed. As a result, the density of photon states, and in turn the radiative decay rate, inside the fluorescent colloids is expected to be reduced by the band structure of the photonic crystal.

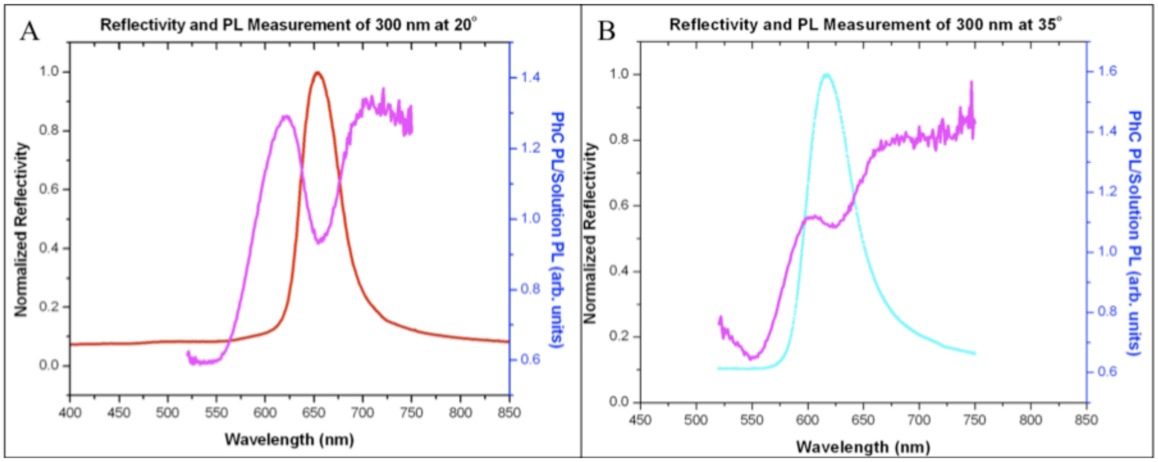

Figure 6.7 Overlay of photoluminescence traces from red colloidal solution (purple lines) and the respective reflectivity traces obtained from the 300 nm colloidal PhC at (A) 20 and (B) 35° represented by the red and blue lines, respectively.

The steady-state emission of the dye from the photonic crystal is collected as a function of angle. The data obtained is normalized with respect to the steady-state emission of the colloidal solution. The normalized PL from the colloidal PhC for different angles is compared with the corresponding reflectivity from the colloidal PhC in Figure 6.7. It is observed that there occurs a wavelength at which the intensity is suppressed, which coincides with the wavelength at which the reflectivity shows a maximum value. The observed effect is due to the presence of a partial photonic stop band or band gap that blue shifts with the angle resulting in the suppression of spontaneous emission at different spectral positions for different angles. A total inhibition of the PL is not observed due to the incomplete photonic band gap of the colloidal PhC system and hence although the available photon density of states is reduced, it is not zero. In addition to the reduction in intensity of the spontaneous emission at different angles, the overall density of states is also lowered. The decreased density of states, in turn leads to a change in the lifetime of the emitter, which is studied by time-resolved PL measurements.

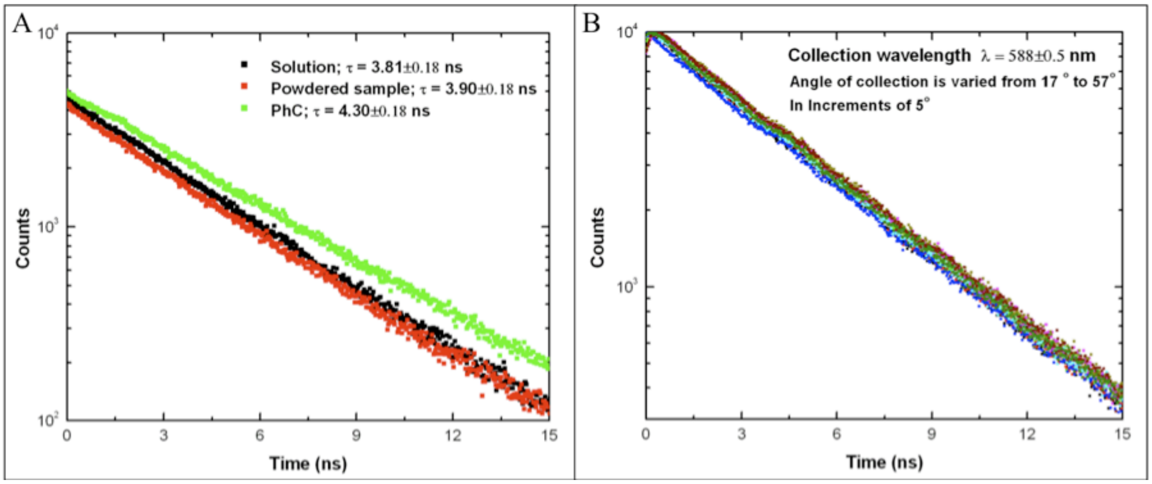

Figure 6.8 Time-resolved PL measurements. (A) Different types of fluorescent samples. (B) Angle-dependent measurements.

The radiative decay rate or lifetime is dependent on the density of states in the system. Time-resolved PL studies are carried out in order to estimate the variation in the lifetime due to a reduction in the available photon density of states as shown in Figure 6.8. Figure 6.8A shows the PL lifetimes for three different samples – colloidal solution (black), powdered colloidal PhC sample (red), and intact colloidal PhC (green). To identify whether a photonic crystal controls the emission rate requires the use of a reference system with the same nanostructure as the photonic system under investigation.[16] Here, the reference is made from the colloidal PhC sample by crushing a piece of the PhC between two clean glass slides. Reflectivity measurements (data not shown) ensure that there is no local ordering in the crushed reference sample. This observation is further supported by the fact that the solution and the reference sample show almost identical lifetimes of 3.81 ± 0.18 ns and 3.90 ± 0.18 ns, respectively. In comparison, the emitter when positioned inside the colloidal PhC sample has a lifetime of 4.30 ± 0.18 ns, which represents an enhancement of 10% compared to that of the reference sample. Angle-dependent time-resolved PL measurements shown in Figure 6.8B are also carried out on the colloidal PhC to determine if there is a change in lifetime when the collection wavelength moves from outside to inside the stop band as the collection angle is varied. The collection wavelength is set at 588.0 ± 1.5 nm. This wavelength lies outside the stop band for small collection angles (up to 25 degrees) and lies inside the stop band for angles greater than 50 degrees (Figure 6.5A). We find that the lifetime does not change as a function of angle (Figure 6.8B). A possible rationale is that the overall density of states of the system is reduced leading to the observed increase in lifetime.

6.2.3 Summary

We have shown the effect of a weak photonic band gap on the steady-state PL emission of a dye. In the colloidal PhC system investigated here, the emitters or fluorescent dyes are sitting inside the dielectric colloids and hence their locations are predefined. In comparison, many of the previous reports had the emitters positioned in random locations within the PhC owing to the fact that the dye infiltration was performed subsequent to PhC preparation. The observed enhancement of about 10% in the lifetime found in the 300 nm particle PhC system is high for a system having such a small refractive index contrast of 0.57. We are able to show that the modification in the steady-state PL is mapped directly to the reflectivity for different angles. There is no dependence of lifetime on the angle of collection.

6.3 Fluorescent 3D Cylindrical Colloidal Photonic Crystal

6.3.1 Experimental Details

Materials. A green-fluorescent 500 nm polystyrene (PS) particle suspension was purchased from Duke Scientific. The white, colloidal suspensions of 300 and 500 nm PS colloids were purchased also from Duke Scientific. Polyimide-coated silica capillaries with an inner diameter of 2 μm were purchased from Polymicro Inc.

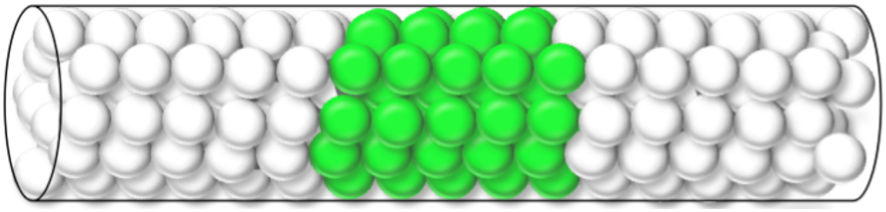

Figure 6.9 Schematic representation of the fluorescent 3D cylindrical colloidal assembly.

Fluorescent Multi-sectional Cylindrical Colloidal PhC. Prior to performing the colloidal assembly, the polyimide-coated silica capillaries are heat-treated in a furnace at 550 °C to remove the polyimide coating. In addition, the inner surface of the bare silica capillaries is etched with 1M NaOH to increase roughness for increased friction between the colloids and the internal surface of the capillaries.[17] The process of multi-sectional colloidal assembly is performed as described in Chapter 3. 500 nm green-fluorescent PS colloids are assembled in between two sections of plain white non-fluorescent PS colloids (300 and/or 500 nm) inside a 2 μm treated silica microcapillary as depicted in Figure 6.9.

Transmission Photoluminescence Measurement. The experimental setups employed for the photonic characterization are identical to those used for the planar PhC measurements (Figure 6.3) with a minor adjustment. As all the measurements are made using colloidal assemblies inside a microcapillary, the optical fiber collecting the signal is custom synthesized and connected to a *Nikon* microscope 100x optics for optimal light collection. In addition, the solid-state laser emitting at 467 nm with a pulse rate of 1 MHz and a pulse width of 50 ps is used at a perpendicular angle to the fluorescent assembly inside the capillary to excite the fluorescent molecules contained within the PS colloids.

6.3.2 Results and Discussion

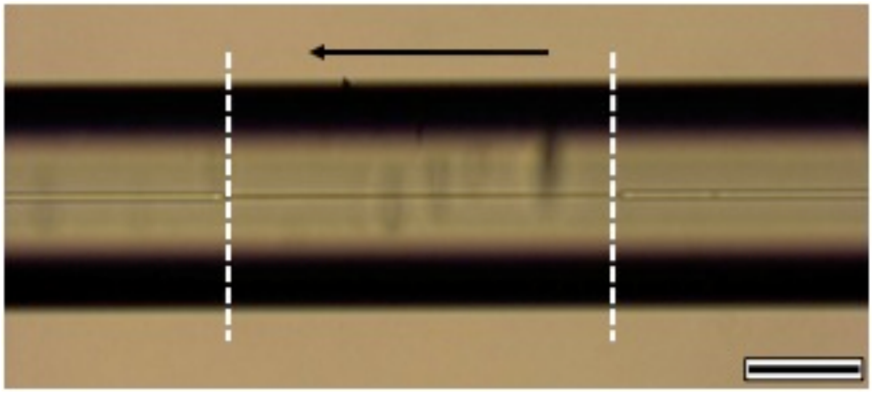

Figure 6.10 Optical microscope image of 500 nm colloidal PhC assembled inside a 2 μm inner diameter silica capillary. The *dark* center region between the two white dashed lines depicts position of the colloidal PhC. The black arrow indicates the direction of the solution flow. Scale bar 25 μm.

The imaging of a 500 nm colloidal PhC inside the silica microcapillary is difficult with traditional optical microscopy. In Figure 6.10, contrast imaging is performed to determine the presence of the colloidal PhC inside the microcapillary. It is possible to observe a *wave-like* particle motion inside the microcapillary during the onset of colloidal infiltration and assembly. The colloidal PhC is confirmed by continuous growth of the dark contrast region highlighted by the dashed white lines in Figure 6.10 with the *wave-like* particle motion terminating at the end of the dark contrast region.

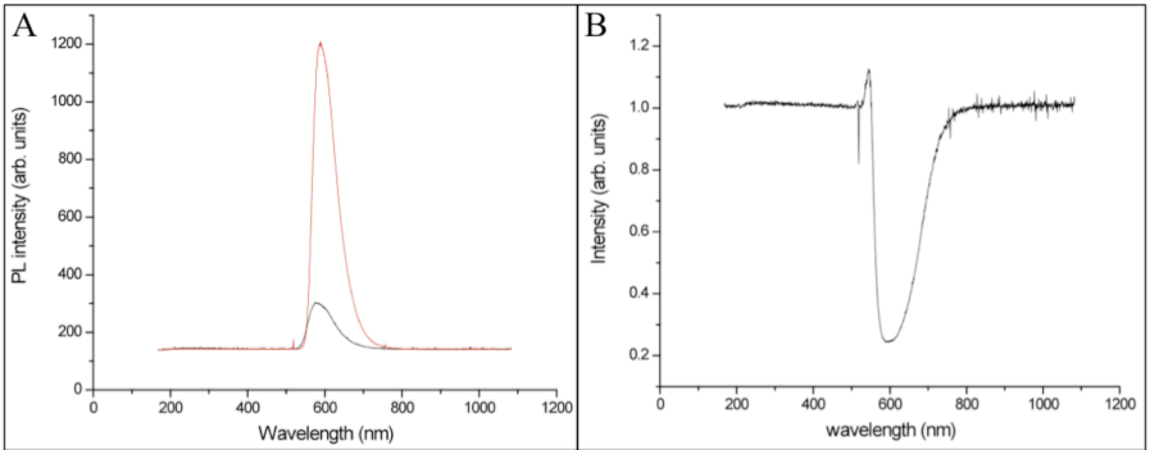

Figure 6.11 (A) PL measurements on 500 nm green PS colloids in suspension (red line) and colloidal assembly inside the silica microcapillary (black line). (B) Normalized PL intensity obtained from the comparison of the two measurements in A.

Preliminary results from the PL measurements indicate potential ordering of the 500 nm fluorescent colloids inside the 2 μm treated silica microcapillaries. Figure 6.11 shows the PL comparison between colloids in suspension and assembled colloids. The reduced PL intensity and width of the peak suggest potential local short-range ordering. As the aspect ratio between the inner diameter of the capillary and the colloids is 4 to 1, local short range ordering may be present due to the wall effect as discussed in Chapter 2.[18, 19] Major problems encountered with the assembly and photonic characterization of submicron-sized particles in 2 μm silica microcapillaries are: (i) slipping of the colloidal assembly during drying, (ii) capillary entrance blockage, and (iii) colloidal jamming in the capillary due to high influx of colloids.

6.3.3 Summary

Preliminary results of the multi-sectional fluorescent cylindrical colloidal assemblies inside silica capillaries show that it is possible to obtain an assembly with a local short-range order. The short-range ordered assembly is confirmed during the assembly process using transmission PL measurements. In order to obtain the desired long-range ordered assembly, more research into addressing the problems encountered during assembly (see above) is necessary. A possible approach using magnetically addressable particles is presented in the next section.

6.4 Magnetically-Enhanced Colloids for Controlled PhC Formation

The directed assembly of colloids is needed to obtain long-range ordered colloidal PhC within the cylindrical confinement for designer photonic materials. PS colloids are surface modified using physical vapor deposition (PVD) of Fe and Fe_xO_y similar to the TiO_2 surface-anisotropic (*sa-*) colloids introduced in Chapter 4. The ferro- or ferri-magnetic properties are desired because of the resulting enhancement of the particle-particle interactions. Further, the enhancement leads to superior addressability and stability of the assembled structures in comparison to structures assembled with other types of directed assemblies such as dieletrophoretic assembly.[20] In addition, compared with other magnetic materials, including cobalt and nickel, Fe and Fe_xO_y are the most cost-efficient materials. To investigate and understand the magnetic interactions of Fe and Fe_xO_y *sa*-PS colloids, the directed assembly of colloids in DI-water is studied in the presence of a magnetic field.

6.4.1 Experimental Details

Materials. Sulfate-terminated PS colloids with 8% (w/v) of 2.5 ± 0.1 μm in aqueous solution were purchased from Invitrogen. Iron wire with a 100 μm diameter on a spool of 10 m was purchased from Alfa Aesar. De-ionized (DI) water was obtained from a Millipore Milli-Q unit. A 0.12 mm thick Secure-Seal self-adhesive silicon spacer with a 13 mm diameter circular well was purchased from Invitrogen. A custom blend of a 3:1 $Ar:O_2$ mixture was synthesized by and purchased from Airgas Inc. A horse-shoe magnet of unknown magnetic field was obtained from the lab of Professor Lee at the Department of Chemical Engineering.

Preparation of the Magnetically Enhanced Colloids. The preparation methods for magnetically-enhanced colloids is similar to that described for the anisotropic colloids prepared in Chapter 4 with the exception that titanium is replaced with iron. Monolayers with sub- to close-packed colloids are obtained and subsequently used for the deposition of iron (Fe) and iron oxide (Fe_xO_y) by PVD.[21] Approximately, 30 cm of iron wire is placed in the 3-strand tungsten wire coil inside the PVD unit (Cressington 308). With monolayer samples placed on a stage underneath the coil (sample-to-source distance is approximately 15 cm), the PVD chamber is pumped until a pressure of 5×10^{-4} Pa is reached. For Fe deposition, the chamber pressure is kept at low pressure during evaporation. For Fe_xO_y deposition, a 3:1 Ar:O_2 gas mixture is used to purge the evaporator chamber and then consistently leaked into the chamber at an evaporation pressure of 0.5 Pa. An average Fe_xO_y deposition rate of 0.3 nm/sec is used to obtain a nominal thickness of 50 ± 3 nm. The deposited colloids on the glass slides are submerged under 100 mL of DI water and ultra-sonicated (40 kHz) for 15 min to lift off the colloids. A dilute suspension with a concentration of less than 0.01% w/v is obtained.

Magnetic Assembly. 60 μL of the dilute suspension of colloids are placed within the confines of the Secure-Seal spacer fastened on acid-cleaned glass slides or silicon wafers. The prepared experimental cell is placed under an Olympus BX-51 optical microscope to study the assembly behavior of the colloids in a magnetic field. Once the setup has been completed, the horse-shoe magnet is placed such that the poles of the magnet are positioned on either side of the experimental cell. Optical images are taken every 30 to 60 sec using a uEye 1000 camera mounted on the microscope. Images are taken until the solution has dried completely.

Imaging and Spectroscopy. Optical images are taken using a uEye digital color camera mounted on the Olympus BX-51 optical microscope. Scanning Electron Microscope (SEM) and High-Resolution SEM (HR-SEM) images are obtained with Carl Zeiss EVO 40 and Supra 55 SEMs, respectively. Both SEMs are equipped with variable-pressure (VP) mode and EDAX X-ray energy dispersive spectroscopy (EDS) units. The VP mode available on the EVO 40 and Supra 55 SEMs allows imaging of non-conductive samples without coating the samples with a conducting surface layer (Au or C) by admitting air or nitrogen into the vacuum chamber at pressures ranging from 35 to 40 Pa. The accelerating voltages used range from 10 – 13 kV and 15 – 20 kV for the EVO 40 and Supra 55, respectively.

6.4.2 Results and Discussion

sa-PS colloids with 50% Fe surface-modification are obtained through high-vacuum PVD. As the oxidation of Fe to Fe_xO_y is inevitable in the aqueous assembly environment, a time-dependent oxidation study is performed to understand the effect of oxidation on the particle-particle interaction and the assembly behavior. Oxidation of Fe is confirmed using EDS to measure oxygen-to-iron weight percentage as a function of time. EDS measurements are normalized to the O:Fe ratio of freshly prepared Fe *sa*-PS colloids on an acid-cleaned silicon wafer as a reference. Oxidized *sa*-PS colloids are analyzed after suspension in DI-water for 5 min, 2 hrs, 24 hrs, and 48hrs. Figure 6.12 plots the O:Fe

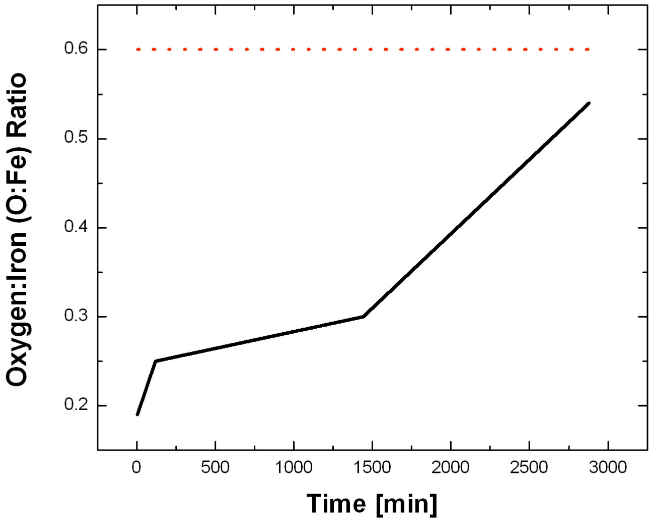

Figure 6.12 EDS measurement of the ratio taken using the weight percentage ratio of O and Fe from oxidized Fe *sa*-PS at various time. Red dashed line indicates the O:Fe of Fe_xO_y *sa*-PS colloids.

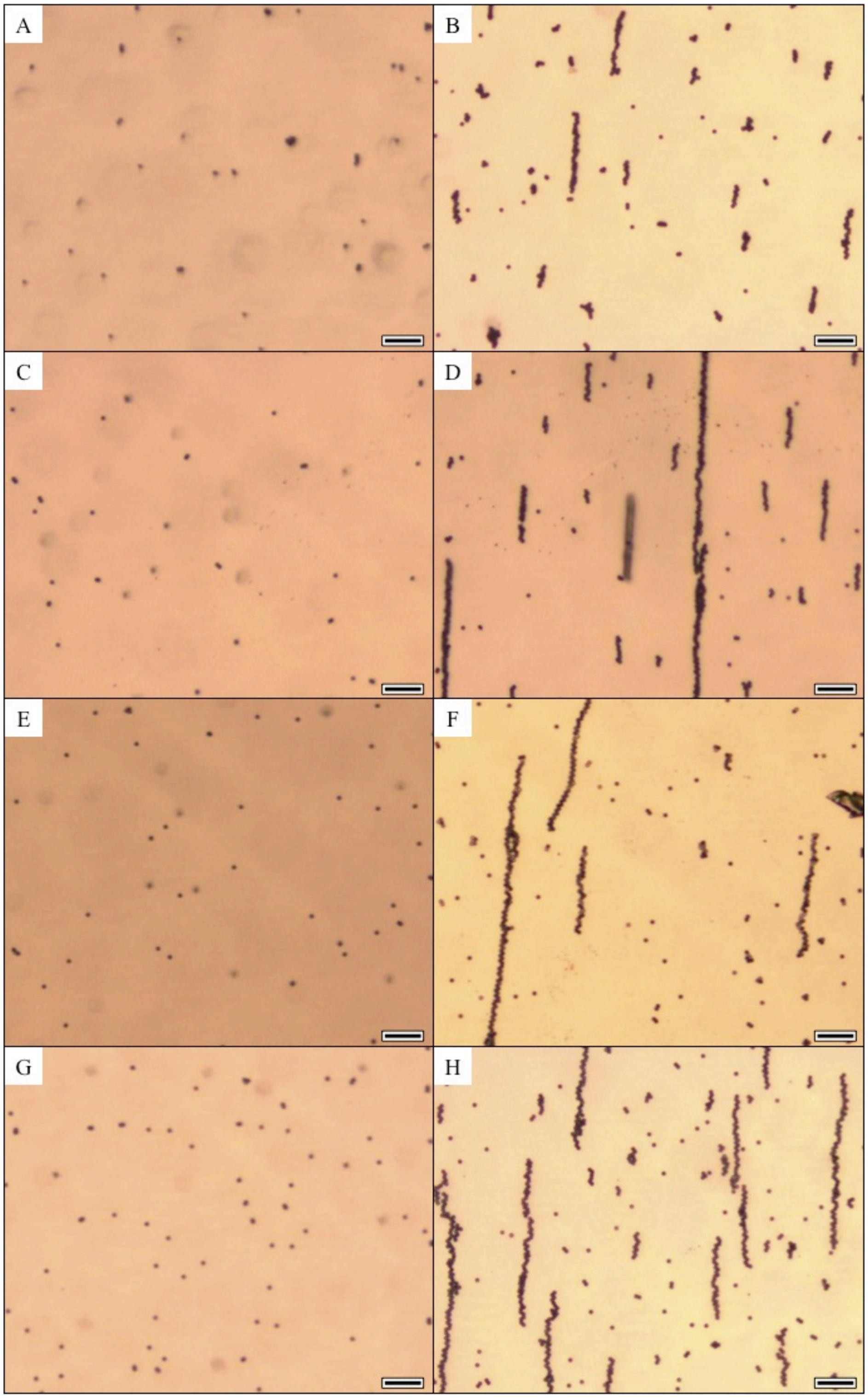

Figure 6.13 Optical microscope images of Fe and Fe_xO_y *sa*-PS colloids suspended in DI-H_2O before and after application of the magnetic field for 30 mins. (A&B) oxidized for 5 mins. (C&D) oxidized for 2 hrs. (E&F) oxidized for 24 hrs. (G&H) oxidized for 48 hrs. All scale bars 25 μm.

ratio determined with EDS as a function of time and shows that the ratio continuously increases as the *sa*-PS colloids are suspended in DI-water for longer times.

The suspended, oxidized Fe *sa*-PS colloids are introduced to a magnetic field using the horse-shoe magnet and allowed to interact. As observed in Figures 6.13 A, C, E, and G, oxidized Fe *sa*-PS colloids are dispersed and suspended in DI-H_2O through ultra-sonication prior to applying a permanent magnetic field. After applying the magnetic field for 30 mins using the horse-shoe magnetic, multiple staggered chain assemblies are obtained aligned parallel to the magnetic field lines (Figures 6.13 B, D, F, and H) in good agreement with results from dielectrophoretic assembly of gold-capped, non-magnetic Janus particles in electric fields.[22] Inspection of the images in Figure 6.13 reveals that the exact cap orientation of the colloids in the resulting chains is difficult to observe using optical microscopy. However, in contrast to the chains formed by dielectrophoresis, the chains formed in the magnetic filed stay intact after the aqueous medium is removed because the magnetic caps stay magnetic. This property allows the deposition and drying of the chains and subsequent study of their configuration and the cap orientation within the chains using high-magnification SEM images.

The resulting chain arrangements obtained after drying of the suspension are shown in Figure 6.14 with suspension time increasing from top to bottom. In the span from 5 min to 48 hrs suspension in DI water (Figures 6.14 A to D), the Fe *sa*-PS colloids undergo continuous oxidation and a change in the chain arrangement of the colloids from random-staggered (random cap direction) to ordered-staggered chains (alternating cap orientation) is observed. The observed change in the arrangements is attributed to the variation of the composition from Fe with surface oxide to Fe_xO_y (Figure 6.12). A possible rationale for

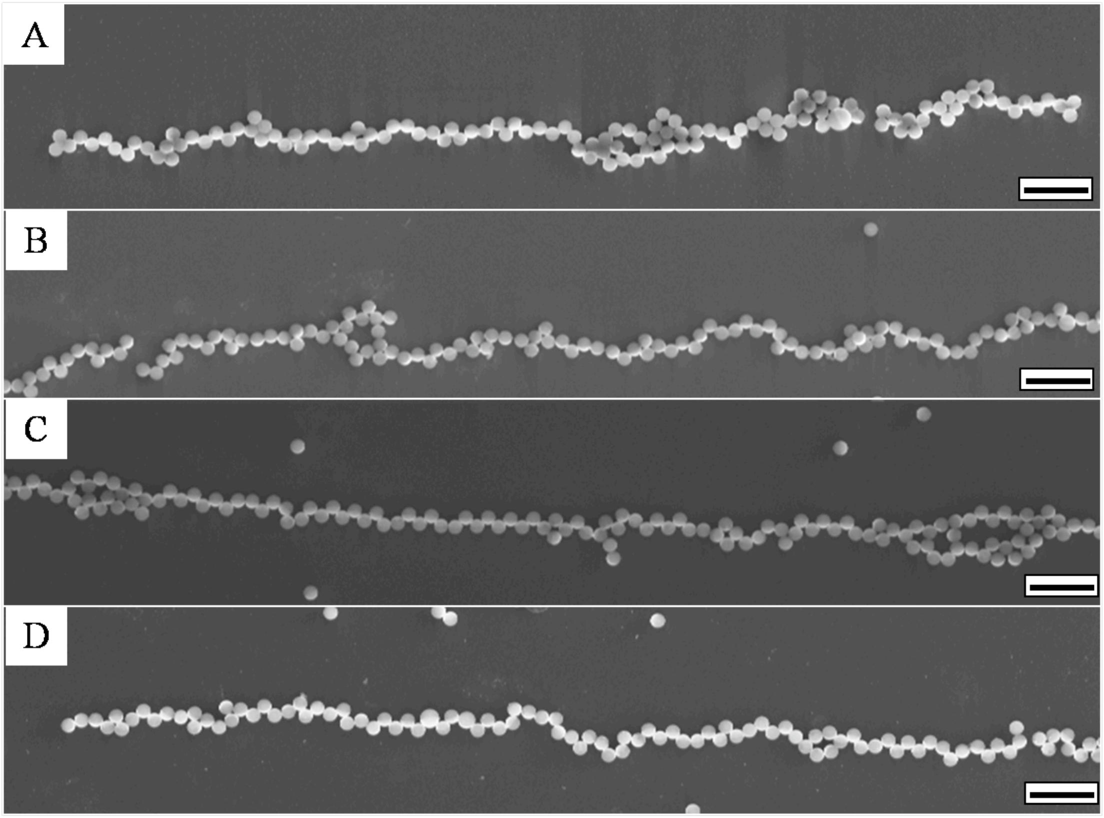

Figure 6.14 SEM images of dried magnetic chain assemblies of oxidized Fe *sa*-PS colloids at various time. (A) Chain assembly obtained after 5 min in suspension (B) Chain assembly obtained after 2 hrs in suspension (C) Chain assembly obtained after 24 hrs in suspension (D) Chain assembly obtained after 48 hrs in suspension. All scale bars 10 µm.

the observed variation in chain structure is that the ferromagnetic properties of the cap change as the degree of oxidation increases due to exposure to DI-water. For example, the maximum magnetic permeability, which measures the susceptibility of a material to a magnetic field leading to magnetization, is 5,000 and 8-10,000 for Fe and Fe_xO_y, respectively, when subjected to a 1 Tesla magnetic field.[23]

To further study the effect of oxidation on the chain arrangement, *sa*-PS colloids with completely oxidized Fe_xO_y caps are examined. Utilizing the technique developed in Chapter 4, PVD of Fe_xO_y is performed. Slow deposition of Fe in a high oxygen concentration environment results in the Fe_xO_y *sa*-PS colloids as confirmed by EDS (dotted red line in Figure 6.12). Similar to the Fe *sa*-PS colloids, the resulting colloids are suspended in DI-water and subjected to a permanent magnetic field.

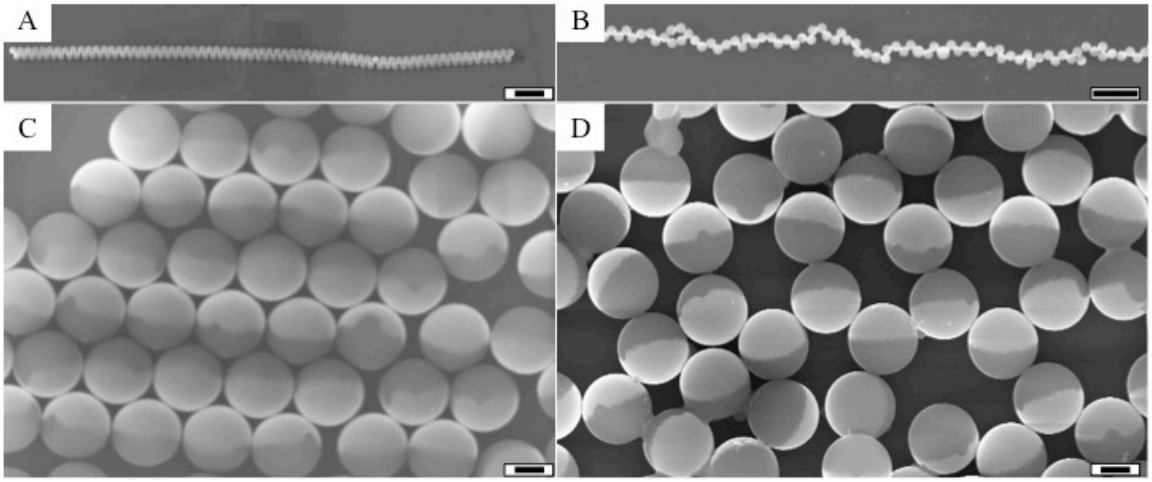

Figure 6.15 SEM images of double and stagger chain magnetic assembly of 2.5 μm PS colloids. (A) Double chain formation using Fe_xO_y surface coating. Scale bar 10 μm. (B) Staggered chain formation using oxidized Fe surface coating after 48 hrs DI-water suspension. Scale bar 10 μm. (C) Convective assembly of double chains. Scale bar 1 μm. (D) Convective assembly of staggered chains. Scale bar 1 μm.

Figure 6.14 shows the comparison between the chain arrangements obtained from Fe_xO_y *sa*-PS colloids (Figure 6.13A) and 48hrs oxidized Fe *sa*-PS colloids (Figure 6.13B). As is evident from the images, two different arrangements are obtained. Magnetic arrangements of Fe_xO_y *sa*-PS colloids result in a double chain arrangement, whereas the staggered chain arrangement is obtained in the oxidized Fe *sa*-PS colloid case. In addition to the single chain arrangement, multiple chain assemblies are of interest as 3D assembly of *sa*-PS colloids is desired. Figures 6.13 C and D are areas of packed double and staggered chains obtained by convective assembly, respectively. Close-packed and random-packed arrangements are observed for the double and staggered chain assemblies, respectively, showing the inherent stability of the chains that enables them to withstand the forces acting during convective assembly as discussed in Chapter 2.

6.4.3 Summary

A preliminary study of the directed assembly of colloids enhanced by magnetic surface-modification using Fe and Fe_xO_y is presented. Different types of interactions and chain arrangements are observed as a function of varying degrees of oxidation of the Fe surface-modification. It is likely that the variation in chain arrangement is caused by changing magnetic properties of the caps. Quantitative identification of the oxidation state of the surface-modification, which would allow the distinction between different types of iron oxide, requires the use of X-ray photoelectron spectroscopy (see Chapter 4). Tailoring the oxidation state of the cap may enable the precise control of the chain arrangement which in turn may lead to unique designer photonic structures and colloidal assemblies inside cylindrical microcapillaries.

6.5 Summary

The effect of close-packed 3D structure on photonic materials is explored. An increase in the lifetime of the emission is observed when 3D fluorescent colloidal assemblies are prepared where the light-emitting source is positioned inside the colloids comprising the PhC. In addition, preliminary work on multi-sectional fluorescent cylindrical colloidal PhC indicates that short-range ordering is possible, but requires finer control of the colloids during assembly. In order to achieve long-range ordering in desired photonic structures, utilization of magnetically enhanced *sa*-PS colloids is suggested.

REFERENCES

1. Joannopoulos, J. D.; Villeneuve, P. R.; Fan, S. H. *Nature* **1997,** *386*, 143-149.
2. Lopez, C. *Advanced Materials* **2003,** *15*, 1679-1704.
3. Lopez, C. *Journal of Optics a-Pure and Applied Optics* **2006,** *8*, R1-R14.
4. Joannopoulos, J. D.; Johnson, S. G.; Winn, J. N.; Meade, R. D., *Photonic Crystals - Molding the flow of light*. Princeton University Press: 2008.
5. Yablonovitch, E. *Physical Review Letters* **1987,** *58*, 2059-2062.
6. Painter, O.; Lee, R. K.; Scherer, A.; Yariv, A.; O'Brien, J. D.; Dapkus, P. D.; Kim, I. *Science* **1999,** *284*, 1819-1821.
7. Kim, J.; Benson, O.; Kan, H.; Yamamoto, Y. *Nature* **1999,** *397*, 500-503.
8. Michler, P.; Kiraz, A.; Becher, C.; Schoenfeld, W. V.; Petroff, P. M.; Zhang, L. D.; Hu, E.; Imamoglu, A. *Science* **2000,** *290*, 2282-2285.
9. Gratzel, M. *Nature* **2001,** *414*, 338-344.
10. Natarajan, H.; Song, J. H.; Kretzschmar, I.; Menom, V. M. *Optical Express* **2009**.
11. Chung, Y. W.; Leu, I. C.; Lee, J. H.; Hon, M. H. *Langmuir* **2006,** *22*, 6454-6460.
12. Chung, Y. W.; Leu, I. C.; Lee, J. H.; Hon, M. H. *Applied Physics a-Materials Science & Processing* **2004,** *79*, 2089-2092.
13. Kim, M. H.; Im, S. H.; Park, O. O. *Advanced Functional Materials* **2005,** *15*, 1329-1335.
14. Im, S. H.; Park, O. O. *Langmuir* **2002,** *18*, 9642-9646.
15. Galisteo-Lopez, J. F.; Palacios-Lidon, E.; Castillo-Martinez, E.; Lopez, C. *Physical Review B* **2003,** *68*.
16. Nikolaev, I. S.; Lodahl, P.; Vos, W. L. *Journal of Physical Chemistry C* **2008,** *112*, 7250-7254.
17. Cifuentes, A.; Canalejas, P.; Ortega, A.; Diez-Masa, J. C. *Journal of Chromatography* **1998**, *283*, 561-571.
18. Pickett, G. T.; Gross, M.; Okuyama, H. *Physical Review Letters* **2000,** *85*, 3652-3655.

19. Mueller, G. E. *Powder Technology* **2005,** *159*, 105-110.

20. Smoukov, S. K.; Gangwal, S.; Marquez, M.; Velev, O. D. *Soft Matter* **2009,** *5*, 1285-1292.

21. Chen, X.; Mao, S. S. *Chemical Reviews* **2007,** *107*, 2891-2959.

22. Gangwal, S.; Cayre, O. J.; Velev, O. D. *Langmuir* **2008,** *24*, 13312-13320.

23. Brown, W. F., *Magnetic Materials*. McGraw-Hill: New York, 1958.

Chapter 7

Conclusions and Future Work

7.1 Concluding Remarks

The thesis work presents an in-depth study on the fabrication of three-dimensionally (3D) templated materials with the emphasis on materials templated using nano- and micrometer sized polymeric colloids. Templated colloidal structures and the resulting porous materials possess unique characteristics and properties that are desired for applications in various fields of science and engineering. The novelty of these materials has been demonstrated.

The multi-sectional colloidal assembly inside a microcapillary is successfully performed and further employed as a sacrificial template for preparation of multi-sectional porous polymeric fibers (PPFs). The PPF fabrication technique is an effective method to obtain PPFs with desired dimensions. In addition, the technique provides a method to control the PPF pore sizes by utilization of different colloid sizes and bulk polymer infiltration time. Further, the technique is extended to incorporate surface-anisotropic colloids as templates to fabricate a porous catalytic membrane reactor (CMR). XRD amorphous titanium dioxide (TiO_2) caps deposited on colloidal carriers by physical vapor deposition of titanium in an oxygen-rich environment are assembled into multi-sectional colloidal crystal by alternating assembly of plain and surface-anisotropic TiO_2

colloids. The removal of the templating colloids after infiltration embeds the TiO_2 deposition into the polymeric porous structures of the CMR. Both processes developed offer precise control of the resulting porous structures with defined porous networks including porosity, pore sizes and shapes, and pore size distribution, which have shown to be crucial in many applications. In addition, through surface anisotropic colloidal templating, CMRs with a controlled distribution of catalyst have been synthesized successfully.

Bridging from the micro- to the macroscale, the synthesis of large-scale porous polymeric materials using centrifugation has been performed successfully and time efficient. Large micrometer-sized polymeric colloids placed in microcentrifuge tubes are centrifugally infiltrated with different types of polymeric materials such as PCL and PDMS illustrating the flexibility of the synthesis technique. PCL is attractive because it is a biodegradable polymer, while PDMS is most cost-effective for separation membranes. Controlling the speed of centrifugation reveals that the formation of surface pores is strongly dependent on the RPM number for PDMS with high RPM numbers leading to fully encapsulated axially porous polymeric tubes.

The design of unique and ordered templated 3D colloidal structures is needed for highly sophisticated photonics applications. The spontaneous emission of fluorescent emitters is controlled using a planar 3D fluorescent colloidal assembly. Further, preliminary studies of multi-sectional assembly of fluorescent colloids in silica microcapillaries indicate short-range colloidal ordering. Magnetically enhanced surface anisotropic colloids are introduced as potential precursors for long-range ordered colloidal structures.

In summary, template assisted materials engineering (TAME) is an effective method for fabricating unique and customizable 3D colloidal assemblies leading to porous polymeric materials that demonstrate wide applicability. Further, utilization of other types of colloids and polymers will extend the potential applications of templated materials beyond the current usage.

7.2 Future Work

Specific thoughts with regard to the directions for future work resulting from this thesis are:

1. Characterization studies - In determining the potential applications and effectiveness of the materials, in-depth porosity characterization techniques need to be developed. Traditional porous material characterization tools target porosity at the large scale and require large quantities of material. A novel technique for quantitative porosity measurements of nano- and microscopic materials should be developed.
2. Application studies - The PPF technique can be extended to a variety of different materials with wide ranges of pore sizes. Therefore, determination of the effectiveness and efficiency for a specific application should be studied. For example, the application of PPFs as scaffolds for bones or nerves in tissue engineering and as CMRs for volatile organic compound removal such as formaldehyde should be explored.
3. Control studies - In photonics, obtaining highly-ordered 3D colloidal structures are crucial. Therefore, the in-depth study of magnetically enhanced colloidal

assembly should be performed to obtain 3D ordered structures inside microcapillaries.

Appendix A

Acronyms and Abbreviations

Acronyms	Definitions
1D	One Dimensional
2D	Two Dimensional
3D	Three-Dimensional
ABA	4-Aminobutanoic Acid
CAPT	Centrifugation Assited Particle Templating
CDTS	Colloidal Delivery and Template System
CMR	Catalytic Membrane Reactor
CT	Colloidal Templating
DI	De-ionized
EDS	X-ray Energy Dispersive Spectroscopy
EBSD	Electron Back Scatter Diffractometry
EM	Electromagnetic Waves
FSCA	Free-Standing Colloidal Assembly
Fe_xO_y	Ferric Oxide
GI	Gravitationally Infiltrated
HPLC	High-Performance Liquid Chromatography
HR-SEM	High Resolution Scanning Electron Microscope
HR-XPS	High Resolution X-ray Photoelectron Spectroscopy
id	Inner Diameter
LDOS	Local Density Of States
MC	Micro Centrifuge
NaOH	Sodium Hydroxide

NMP	1-Methyl-2Pyrrolidone
p-PS	Plain Polystyrene
PCL	Poly(ε-caporlactone)
PDMS	Polydimethylsiloxane
PhC	Photonic Crystal
PI	Process Intensification
PL	Photoluminescence
PMMA	Polymethylmethacrylate
PPF	Porous Polymeric Fiber
PPM	Porous Polymeric Material
PS	Polystyrene
PTFE	Polytetrafluoroethylene
PU	Polyurethane
PVD	Physical Vapor Deposition
RPM	Rotations Per Minute
sa-PS	Surface Anisotropic Polystyrene
SEM	Scanning Electron Microscope
TACA	Template Assisted Colloidal Assembly
TAME	Template Assisted Materials Engineering
TEM	Transmission Electron Microscopy
THF	Tetrahydrofuran
TiC	Titanium Carbide
TiO	Titanium (II) Oxide
TiO_2	Titanium (IV) Oxide
Ti_2O_3	Titanium (III) Oxide
Ti_xO_y	Titanium Oxide
UV	Ultra-Violet
vp-SEM	Variable Pressure Scanning Electron Microscope
XPS	X-ray Photoelectron Spectroscopy
XRD	X-ray Diffractometry

References

Chapter 1

1. Xia, Y. N.; Gates, B.; Yin, Y. D.; Lu, Y. *Advanced Materials* **2000,** *12*, 693-713.

2. Yang, S. M.; Jang, S. G.; Choi, D. G.; Kim, S.; Yu, H. K. *Small* **2006,** *2*, 458-475.

3. Ulbricht, M. *Polymer* **2006,** *47*, 2217-2262.

4. Chung, T. S. *Polymers & Polymer Composites* **1996,** *4*, 269-283.

5. Karageorgiou, V.; Kaplan, D. *Biomaterials* **2005,** *26*, 5474-5491.

6. Ozdemir, S. S.; Buonomenna, M. G.; Drioli, E. *Applied Catalysis a-General* **2006,** *307*, 167-183.

7. Langer, R.; Tirrell, D. A. *Nature* **2004,** *428*, 487-492.

8. Lee, K. Y.; Mooney, D. J. *Chemical Reviews* **2001,** *101*, 1869-1879.

9. Soten, I.; Ozin, G. A. *Current Opinion in Colloid & Interface Science* **1999,** *4*, 325-337.

10. Waterhouse, G. I. N.; Waterland, M. R. *Polyhedron* **2007,** *26*, 356-368.

11. Wang, D. Y.; Mohwald, H. *Journal of Materials Chemistry* **2004,** *14*, 459-468.

12. Grzybowski, B. A.; Wilmer, C. E.; Kim, J.; Browne, K. P.; Bishop, K. J. M. *Soft Matter* **2009,** *5*, 1110-1128.

13. Rycenga, M.; Camargo, P. H. C.; Xia, Y. N. *Soft Matter* **2009,** *5*, 1129-1136.

14. Dziomkina, N. V.; Vancso, G. J. *Soft Matter* **2005,** *1*, 265-279.

15. Stein, A.; Schroden, R. C. *Current Opinion in Solid State & Materials Science* **2001,** *5*, 553-564.

16. Velev, O. D.; Lenhoff, A. M. *Current Opinion in Colloid & Interface Science* **2000,** *5*, 56-63.

17. Jiang, P.; Bertone, J. F.; Hwang, K. S.; Colvin, V. L. *Chemistry of Materials* **1999,** *11*, 2132-2140.

18. Kotov, N. A.; Liu, Y. F.; Wang, S. P.; Cumming, C.; Eghtedari, M.; Vargas, G.; Motamedi, M.; Nichols, J.; Cortiella, J. *Langmuir* **2004,** *20*, 7887-7892.

19. Jin, C. J.; McLachlan, M. A.; McComb, D. W.; De La Rue, R. M.; Johnson, N. P. *Nano Letters* **2005,** *5*, 2646-2650.

20. Singh, K. B.; Tirumkudulu, M. S. *Physical Review Letters* **2007,** *98*.

21. Song, J. H.; Kretzschmar, I. *Langmuir* **2008,** *24*, 10616-10620.

22. Yang, P. D.; Rizvi, A. H.; Messer, B.; Chmelka, B. F.; Whitesides, G. M.; Stucky, G. D. *Advanced Materials* **2001,** *13*, 427-431.

23. Yan, F.; Goedel, W. A. *Advanced Materials* **2004,** *16*, 911-915.

24. Jiang, P.; Hwang, K. S.; Mittleman, D. M.; Bertone, J. F.; Colvin, V. L. *Journal of the American Chemical Society* **1999,** *121*, 11630-11637.

25. Sedlacek, B.; Kahovec, J., *Synthetic Polymeric Membranes*. Walter De Gruyter: New York, 1987.

26. Lloyd, D., *Materials Science of Synthetic Membrane*. American Chemical Society: Washington D.D., 1985.

27. Sirkar, K.; Lloyd, D., *New Membrane Materials and Processes for Separation*. American Institute of Chemical Engineers: New York, 1988; Vol. 84.

28. Park, J.; Bronzion, J., *Biomaterials - Principles and Applications*. CRC Press: Boca Raton, 2003.

29. Vieth, W. R., *Membrane Systems: Analysis and Design*. Oxford University Press: Munich, 1988.

30. Miguez, H.; Yang, S. M.; Ozin, G. A. *Langmuir* **2003,** *19*, 3479-3485.

31. Miguez, H.; Yang, S. M.; Ozin, G. A. *Applied Physics Letters* **2002,** *81*, 2493-2495.

Chapter 2

1. Velev, O. D.; Lenhoff, A. M.; Kaler, E. W. *Science* **2000,** *287*, 2240-2243.
2. Velev, O. D.; Lenhoff, A. M. *Current Opinion in Colloid & Interface Science* **2000,** *5*, 56-63.
3. Clark, T. D.; Ferrigno, R.; Tien, J.; Paul, K. E.; Whitesides, G. M. *Journal of the American Chemical Society* **2002,** *124*, 5419-5426.
4. Grzybowski, B. A.; Wilmer, C. E.; Kim, J.; Browne, K. P.; Bishop, K. J. M. *Soft Matter* **2009,** *5*, 1110-1128.
5. Dziomkina, N. V.; Vancso, G. J. *Soft Matter* **2005,** *1*, 265-279.
6. Xia, Y. N.; Gates, B.; Yin, Y. D.; Lu, Y. *Advanced Materials* **2000,** *12*, 693-713.
7. Yan, F.; Goedel, W. A. *Advanced Materials* **2004,** *16*, 911-915.
8. Liu, Y. F.; Wang, S. P.; Lee, J. W.; Kotov, N. A. *Chemistry of Materials* **2005,** *17*, 4918-4924.
9. Kotov, N. A.; Liu, Y. F.; Wang, S. P.; Cumming, C.; Eghtedari, M.; Vargas, G.; Motamedi, M.; Nichols, J.; Cortiella, J. *Langmuir* **2004,** *20*, 7887-7892.
10. Hoa, M. L. K.; Lu, M. H.; Zhang, Y. *Advances in Colloid and Interface Science* **2006,** *121*, 9-23.
11. Chung, Y. W.; Leu, I. C.; Lee, J. H.; Hon, M. H. *Langmuir* **2006,** *22*, 6454-6460.
12. Im, S. H.; Lim, Y. T.; Suh, D. J.; Park, O. O. *Advanced Materials* **2002,** *14*, 1367-1369.
13. Kim, M. H.; Im, S. H.; Park, O. O. *Advanced Functional Materials* **2005,** *15*, 1329-1335.
14. Im, S. H.; Park, O. O. *Langmuir* **2002,** *18*, 9642-9646.
15. Zeng, F.; Sun, Z. W.; Wang, C. Y.; Ren, B. Y.; Liu, X. X.; Tong, Z. *Langmuir* **2002,** *18*, 9116-9120.
16. Chung, Y. W.; Leu, I. C.; Lee, J. H.; Hon, M. H. *Applied Physics a-Materials Science & Processing* **2004,** *79*, 2089-2092.
17. Kralchevsky, P. A.; Denkov, N. D. *Current Opinion in Colloid & Interface Science* **2001,** *6*, 383-401.

18. Dimitrov, A. S.; Nagayama, K. *Langmuir* **1996,** *12*, 1303-1311.

19. Kralchevsky, P. A.; Nagayama, K. *Langmuir* **1994,** *10*, 23-36.

20. Paunov, V. N.; Kralchevsky, P. A.; Denkov, N. D.; Nagayama, K. *Journal of Colloid and Interface Science* **1993,** *157*, 100-112.

21. Kim, B. M.; Qian, S.; Bau, H. H. *Nano Letters* **2005,** *5*, 873-878.

22. Paunov, V. N. *Langmuir* **1998,** *14*, 5088-5097.

23. Rycenga, M.; Camargo, P. H. C.; Xia, Y. N. *Soft Matter* **2009,** *5*, 1129-1136.

24. Wu, H. K.; Thalladi, V. R.; Whitesides, S.; Whitesides, G. M. *Journal of the American Chemical Society* **2002,** *124*, 14495-14502.

25. Velev, O. D.; Jede, T. A.; Lobo, R. F.; Lenhoff, A. M. *Chemistry of Materials* **1998,** *10*, 3597-3602.

26. Wang, D. Y.; Mohwald, H. *Journal of Materials Chemistry* **2004,** *14*, 459-468.

27. Miguez, H.; Yang, S. M.; Ozin, G. A. *Langmuir* **2003,** *19*, 3479-3485.

28. Miguez, H.; Yang, S. M.; Ozin, G. A. *Applied Physics Letters* **2002,** *81*, 2493-2495.

29. Yi, G. R.; Moon, J. H.; Yang, S. M. *Advanced Materials* **2001,** *13*, 1185-1188.

30. Ye, J. H.; Zentel, R.; Arpiainen, S.; Ahopelto, J.; Jonsson, F.; Romanov, S. G.; Torres, C. M. S. *Langmuir* **2006,** *22*, 7378-7383.

31. Xia, D. Y.; Li, D.; Luo, Y.; Brueck, S. R. J. *Advanced Materials* **2006,** *18*, 930-933.

32. Yang, P. D.; Deng, T.; Zhao, D. Y.; Feng, P. Y.; Pine, D.; Chmelka, B. F.; Whitesides, G. M.; Stucky, G. D. *Science* **1998,** *282*, 2244-2246.

33. Park, S. H.; Xia, Y. N. *Langmuir* **1999,** *15*, 266-273.

34. Stein, A.; Schroden, R. C. *Current Opinion in Solid State & Materials Science* **2001,** *5*, 553-564.

35. Moon, J. H.; Kim, S.; Yi, G. R.; Lee, Y. H.; Yang, S. M. *Langmuir* **2004,** *20*, 2033-2035.

36. Morrison, I.; Ross, S., *Colloidal Dispersion*. John Wiley and Sons Inc.: New York 2002.

37. Hiemenz, P.; Rajagopalan, R., *Principles of Colloid and Surface Chemistry*. 3rd ed.; Marcel Dekker: New York, 1997; p 650.

38. Kim, E.; Xia, Y. N.; Whitesides, G. M. *Journal of the American Chemical Society* **1996,** *118*, 5722-5731.

39. Kim, E.; Xia, Y. N.; Whitesides, G. M. *Advanced Materials* **1996,** *8*, 245-247.

40. Kim, B. M.; Sinha, S.; Bau, H. H. *Nano Letters* **2004,** *4*, 2203-2208.

41. Burger, R.; Fjelde, K. K.; Hofler, K.; Karlsen, K. H. *Journal of Engineering Mathematics* **2001,** *41*, 167-187.

42. Li, F.; He, J. B.; Zhou, W. L. L.; Wiley, J. B. *Journal of the American Chemical Society* **2003,** *125*, 16166-16167.

43. Ehlert, S.; Roesler, T.; Tallarek, U. *Journal of Separation Science* **2008,** *31*, 1719-1728.

44. Muller, C. R.; Holland, D. J.; Sederman, A. J.; Mantle, M. D.; Gladden, L. F.; Davidson, J. F. In *Magnetic Resonance Imaging of fluidized beds*, 2008; pp 53-62.

45. Baldwin, C. A.; Sederman, A. J.; Mantle, M. D.; Alexander, P.; Gladden, L. F. *Journal of Colloid and Interface Science* **1996,** *181*, 79-92.

46. Sederman, A. J.; Alexander, P.; Gladden, L. F. *Powder Technology* **2001,** *117*, 255-269.

47. Harris, W. F.; Erickson, R. O. *Journal of Theoretical Biology* **1980,** *83*, 215-246.

48. Erickson, R. O. *Science* **1973,** *181*, 705-716.

49. Pickett, G. T.; Gross, M.; Okuyama, H. *Physical Review Letters* **2000,** *85*, 3652-3655.

50. Mueller, G. E. *Powder Technology* **2005,** *159*, 105-110.

51. Hsieh, S. C.; Jorgenson, J. W. *Analytical Chemistry* **1996,** *68*, 1212-1217.

52. Jung, S.; Ehlert, S.; Mora, J. A.; Kraiczek, K.; Dittmann, M.; Rozing, G. P.; Tallarek, U. *Journal of Chromatography A* **2009,** *1216*, 264-273.

53. Levenberg, S.; Langer, R., *Current Topics in Developmental Biology* **2004**, *61*, 113-134.

54. Langer, R.; Tirrell, D. A. *Nature* **2004,** *428*, 487-492.

55. Ulbricht, M. *Polymer* **2006,** *47*, 2217-2262.

56. Lonsdale, H. K. *Journal of Membrane Science* **1982,** *10*, 81-181.

57. Dixon, A. G. *Int. J. Chem. Reactor Eng.* **2003,** *1*, 1-35.

58. Ozdemir, S. S.; Buonomenna, M. G.; Drioli, E. *Applied Catalysis a-General* **2006,** *307*, 167-183.

59. Vankelecom, I. F. J. *Chemical Reviews* **2002,** *102*, 3779-3810.

60. Capes, J. S.; Ando, H. Y.; Cameron, R. E. *Journal of Materials Science-Materials in Medicine* **2005,** *16*, 1069-1075.

61. Pandey, P.; Chauhan, R. S. *Progress in Polymer Science* **2001,** *26*, 853-893.

62. Sirkar, K.; Lloyd, D., *New Membrane Materials and Processes for Separation*. American Institute of Chemical Engineers: New York, 1988; Vol. 84.

63. Kesting, R., *Synthetic Polymeric Membranes*. John Wiley & Sons, Inc.: New York, 1985.

64. Lloyd, D., *Materials Science of Synthetic Membrane*. American Chemical Society: Washington D.D., 1985.

65. de Jong, J.; Lammertink, R. G. H.; Wessling, M. *Lab on a Chip* **2006,** *6*, 1125-1139.

66. Karageorgiou, V.; Kaplan, D. *Biomaterials* **2005,** *26*, 5474-5491.

67. Park, J.; Bronzion, J., *Biomaterials - Principles and Applications*. CRC Press: Boca Raton, 2003.

68. Vieth, W. R., *Membrane Systems: Analysis and Design*. Oxford University Press: Munich, 1988.

69. Dokko, K.; Akutagawa, N.; Isshiki, Y.; Hoshina, K.; Kanamura, K. *Solid State Ionics* **2005,** *176*, 2345-2348.

70. Jiang, P.; Hwang, K. S.; Mittleman, D. M.; Bertone, J. F.; Colvin, V. L. *Journal of the American Chemical Society* **1999,** *121*, 11630-11637.

71. Imhof, A.; Pine, D. J. *Advanced Materials* **1998,** *10*, 697-700.

72. Imhof, A.; Pine, D. J. *Nature* **1997,** *389*, 948-951.

73. George, S. C.; Thomas, S. *Progress in Polymer Science* **2001,** *26*, 985-1017.

74. Cui, J. Q.; Kretzschmar, I. *Langmuir* **2006,** *22*, 8281-8284.

75. Koros, W. J.; Fleming, G. K. *Journal of Membrane Science* **1993,** *83*, 1-80.

76. Chung, T. S. *Polymers & Polymer Composites* **1996,** *4*, 269-283.

77. Zsigmondy, R. Filter And Method of Producing Same. 1421341, 1922.

78. Fleische.Rl; Alter, H. W.; Walker, R. M.; Furman, S. C.; Price, P. B. *Science* **1972,** *178*, 255-263.

79. Fleische.Rl; Price, P. B.; Walker, R. M. *Scientific American* **1969,** *220*, 30-39.

80. Price, P. B. Molecular Sieves and Methods For Producing Same. 3303085, Feb. 7, 1967, 1962.

81. Kuiper, S.; van Rijn, C. J. M.; Nijdam, W.; Elwenspoek, M. C. *Journal of Membrane Science* **1998,** *150*, 1-8.

82. M. Druin, J. L., S. Plovan Novel Open-Celled Microporus Film. 3801404, 1972.

83. Gore, R. Process for producing porous products. 3953566, 1976.

84. Gore, R. Very highly stretched polytetrafluoroethylene and process therefor. 3962153, June 8, 1976, 1976.

85. vandeWitte, P.; Dijkstra, P. J.; vandenBerg, J. W. A.; Feijen, J. *Journal of Membrane Science* **1996,** *117*, 1-31.

86. Peppas, N. A.; Hilt, J. Z.; Khademhosseini, A.; Langer, R. *Advanced Materials* **2006,** *18*, 1345-1360.

87. Lee, K. Y.; Mooney, D. J. *Chemical Reviews* **2001,** *101*, 1869-1879.

88. Peppas, N. A.; Huang, Y. *Pharmaceutical Research* **2002,** *19*, 578-587.

89. Drury, J. L.; Mooney, D. J. *Biomaterials* **2003,** *24*, 4337-4351.

90. Lavik, E. B.; Klassen, H.; Warfvinge, K.; Langer, R.; Young, M. J. *Biomaterials* **2005,** *26*, 3187-3196.

91. Stenzel, K. H.; Miyata, T.; Rubin, A. L. *Annual Review of Biophysics and Bioengineering* **1974,** *3*, 231-253.

92. Song, E.; Kim, S. Y.; Chun, T.; Byun, H. J.; Lee, Y. M. *Biomaterials* **2006,** *27*, 2951-2961.

93. Blacher, S.; Maquet, V.; Schils, F.; Martin, D.; Schoenen, J.; Moonen, G.; Jerome, R.; Pirard, J. P. *Biomaterials* **2003,** *24*, 1033-1040.

94. Soten, I.; Ozin, G. A. *Current Opinion in Colloid & Interface Science* **1999,** *4*, 325-337.

95. Gates, B.; Yin, Y. D.; Xia, Y. N. *Chemistry of Materials* **1999,** *11*, 2827-2836.

96. ChemWare, K., Polymer Analysis - Solubility and solvents for dissolution. In *http://home.planet.nl/~skok/database/solubility/*, Zeist, Netherlands, 2002.

97. Miller-Chou, B. A.; Koenig, J. L. *Progress in Polymer Science* **2003,** *28*, 1223-1270.

98. Mark, J., *Physical Properties of Polymers Handbook*. Woodbury, New York, 1996.

99. Murray, C. B.; Kagan, C. R.; Bawendi, M. G. *Annual Review of Materials Science* **2000,** *30*, 545-610.

100. Nakao, S. *Journal of Membrane Science* **1994,** *96*, 131-165.

101. Lin, Y. S.; Burggraaf, A. J. *Journal of the American Ceramic Society* **1991,** *74*, 219-224.

102. Dunn, B.; Zink, J. I. *Chemistry of Materials* **1997,** *9*, 2280-2291.

103. Kaneko, K. *Journal of Membrane Science* **1994,** *96*, 59-89.

104. Paredes, J. I.; Martinez-Alonso, A.; Tascon, J. M. D. *Microporous and Mesoporous Materials* **2003,** *65*, 93-126.

105. Manabe, S.; Shigemoto, Y.; Kamide, K. *Polymer Journal* **1985,** *17*, 775-785.

106. Manabe, S.; Kamata, Y.; Iijima, H.; Kamide, K. *Polymer Journal* **1987,** *19*, 391-404.

107. Zeman, L.; Denault, L. *Journal of Membrane Science* **1992,** *71*, 221-231.

108. Zeman, L. *Journal of Membrane Science* **1992,** *71*, 233-246.

109. Dietz, P.; Hansma, P. K.; Inacker, O.; Lehmann, H. D.; Herrmann, K. H. *Journal of Membrane Science* **1992,** *65*, 101-111.

110. Fritzsche, A. K.; Arevalo, A. R.; Moore, M. D.; Ohara, C. *Journal of Membrane Science* **1993,** *81*, 109-120.

111. Fritzsche, A. K.; Arevalo, A. R.; Moore, M. D.; Weber, C. J.; Elings, V. B.; Kjoller, K.; Wu, C. M. *Journal of Applied Polymer Science* **1992,** *46*, 167-178.

112. Fritzsche, A. K.; Arevalo, A. R.; Connolly, A. F.; Moore, M. D.; Elings, V.; Wu, C. M. *Journal of Applied Polymer Science* **1992,** *45*, 1945-1956.

113. Fritzsche, A. K.; Arevalo, A. R.; Moore, M. D.; Elings, V. B.; Kjoller, K.; Wu, C. M. *Journal of Membrane Science* **1992,** *68*, 65-78.

114. Nanotechnology, P., Polymer. In *Safari*, http://www.pacificnanotech.com/polymers_single.html, Ed. 2002-2006.

Chapter 3

1. Ulbricht, M. *Polymer* **2006,** *47*, 2217-2262.

2. Karageorgiou, V.; Kaplan, D. *Biomaterials* **2005,** *26*, 5474-5491.

3. Vankelecom, I. F. J. *Chemical Reviews* **2002,** *102*, 3779-3810.

4. Xia, Y. N.; Gates, B.; Yin, Y. D.; Lu, Y. *Advanced Materials* **2000,** *12*, 693-713.

5. Stein, A.; Schroden, R. C. *Current Opinion in Solid State & Materials Science* **2001,** *5*, 553-564.

6. Hoa, M. L. K.; Lu, M. H.; Zhang, Y. *Advances in Colloid and Interface Science* **2006,** *121*, 9-23.

7. Imhof, A.; Pine, D. J. *Nature* **1997,** *389*, 948-951.

8. Velev, O. D.; Lenhoff, A. M. *Current Opinion in Colloid & Interface Science* **2000,** *5*, 56-63.

9. Li, J.; Zhang, Y. *Chemistry of Materials* **2007,** *19*, 2581-2584.

10. Miguez, H.; Yang, S. M.; Ozin, G. A. *Langmuir* **2003,** *19*, 3479-3485.

11. Moon, J. H.; Kim, S.; Yi, G. R.; Lee, Y. H.; Yang, S. M. *Langmuir* **2004,** *20*, 2033-2035.

12. Hong, S. H.; Moon, J. H.; Lim, J. M.; Kim, S. H.; Yang, S. M. *Langmuir* **2005,** *21*, 10416-10421.

13. Yake, A.M.; Snyder, C.E.; Velegol, D. *Langmuir* **2007,** *23*, 9069-9075.

14. Velegol, D. *J. Nanophotonics* **2007,** *1*, 1-25.

15. Yan, F.; Goedel, A. *Advanced Materials* **2004,** 1*6*, 911-915.

16. Waterhouse, G. I. N.; Waterland, M. R. *Polyhedron* **2007,** *26*, 356-368.

17. Gates, B.; Qin, D.; Xia, Y. N. *Advanced Materials* **1999,** *11*, 466-469.

18. Lee, S. K.; Yi, G. R.; Yang, S. M. *Lab on aChip* **2006**, *6*, 1171-1177.

19. Hiemenz, P.; Rajagopalan, R. *Principles of Colloid and Surface Chemistry*; 3rd ed.; Marcel Dekker: NY, 1997; p 650.

20. Mueller, G. E. *Powder Technology* **1997,** *92*, 179-183.

21. Mueller, G. E. *Powder Technology* **2005,** *159*, 105-110.

22. Rengarajan, R.; Mittleman, D.; Rich, C.; Colvin, V. *Physical Review E* **2005,** *71*, 016615

23. Ge, H. L.; Song, Y. L.; Jiang, L.; Zhu, D. B. *Thin Solid Films* **2006,** *515*, 1539-1543.

24. Simonsen, A. C.; Hansen, P. L.; Klosgen, B. *Journal of Colloid and Interface Science* **2004,** *273*, 291-299.

25. Kim, B. M.; Qian, S.; Bau, H. H. *Nano Letter* **2005,** *5*, 873-878.

26. Jiang, P.; Hwang, K. S.; Mittleman, D. M.; Bertone, J. F.; Colvin, V. L. *Journal of American Chemical Society* **1999,** *121*, 11630-11637.

27. Brandrup, J. I., E.H.; Grulke, E.A.; Abe, A.; Bloch, D.R. *Polymer Handbook*; 4th ed.; John Wiley & Sons: NY, 2005.

28. *Technical Data Sheet - Norland Optical Adhesive*; Norland Product Inc.

29. Ishiyama, C.; Higo, Y. *Journal of Polymer Science Part B-Polymer Physics* **2002,** *40*, 460-465.

30. Stoye, D.; Freitag, W. *Paints, coatings, and solvents*; Wiley-VCH Verlag GmbH: Weinheim, 1998; p 431.

31. Gates, B.; Yin, Y. D.; Xia, Y. N. *Chemistry of Materials* **1999,** *11*, 2827-2836.

32. Coxeter, H. S. M. *Introduction to Geometry*; 2nd ed.; John Wiley & Sons: NY, 1969; p 13 -16.

33. Wang, H. Z.; Li, X. Y.; Nakamura, H.; Miyazaki, M. P.; Maeda, H. *Advanced Materials* **2002**, *22*, 1662-1666.

Chapter 4

1. Dittmeyer, R.; Hollein, V.; Daub, K. *Journal of Molecular Catalysis a-Chemical* **2001,** *173*, 135-184.

2. Stankiewicz, A. *Chemical Engineering and Processing* **2003,** *42*, 137-144.

3. Vankelecom, I. F. J. *Chemical Reviews* **2002,** *102*, 3779-3810.

4. Vankelecom, I. F. J.; Vercruysse, K. A. L.; Neys, P. E.; Tas, D. W. A.; Janssen, K. B. M.; Knops-Gerrits, P. P.; Jacobs, P. A. *Topics in Catalysis* **1998,** *5*, 125-132.

5. Stankiewicz, A. *Chemical Engineering Research & Design* **2006,** *84*, 511-521.

6. Ozdemir, S. S.; Buonomenna, M. G.; Drioli, E. *Applied Catalysis a-General* **2006,** *307*, 167-183.

7. Dixon, A. G. *Int. J. Chem. Reactor Eng.* **2003,** *1*, 1-35.

8. Song, J. H.; Kretzschmar, I. *Langmuir* **2008,** *24*, 10616-10620.

9. Perro, A.; Reculusa, S.; Ravaine, S.; Bourgeat-Lami, E. B.; Duguet, E. *Journal of Materials Chemistry* **2005,** *15*, 3745-3760.

10. Smoukov, S. K.; Gangwal, S.; Marquez, M.; Velev, O. D. *Soft Matter* **2009,** *5*, 1285-1292.

11. Chen, X.; Mao, S. S. *Chemical Reviews* **2007,** *107*, 2891-2959.

12. Feng, B.; Chen, J. Y.; Qi, S. K.; He, L.; Zhao, J. Z.; Zhang, X. D. *Journal of Materials Science-Materials in Medicine* **2002,** *13*, 457-464.

13. Kasemo, B. *Journal of Prosthetic Dentistry* **1983,** *49*, 832-837.

14. Quinn, R. K.; Armstrong, N. R. *Journal of the Electrochemical Society* **1978,** *125*, 1790-1796.

15. Armstrong, N. R.; Quinn, R. K. *Surface Science* **1977,** *67*, 451-468.

16. Li, Y. L.; Ishigaki, T. *Chemistry of Materials* **2001,** *13*, 1577-1584.

17. Chen, G. S.; Lee, C. C.; Niu, H.; Huang, W.; Jann, R.; Schutte, T. *Thin Solid Films* **2008,** *516*, 8473-8478.

18. Giolli, C.; Borgioli, F.; Credi, A.; Di Fabio, A.; Fossati, A.; Miranda, M. M.; Parmeggiani, S.; Rizzi, G.; Scrivani, A.; Troglio, S.; Tolstoguzov, A.; Zoppi, A.; Bardi, U. **2007**, 13-22.

19. Kwon, S.; Fan, M.; Cooper, A. T.; Yang, H. Q. *Critical Reviews in Environmental Science and Technology* **2008,** *38*, 197-226.

20. Carp, O.; Huisman, C. L.; Reller, A. *Progress in Solid State Chemistry* **2004,** *32*, 33-177.

21. Yu, J. C.; Yu, J. G.; Ho, W. K.; Jiang, Z. T.; Zhang, L. Z. *Chemistry of Materials* **2002,** *14*, 3808-3816.

22. Sibu, C. P.; Kumar, S. R.; Mukundan, P.; Warrier, K. G. K. *Chemistry of Materials* **2002,** *14*, 2876-2881.

23. Hong, X. T.; Wang, Z. P.; Cai, W. M.; Lu, F.; Zhang, J.; Yang, Y. Z.; Ma, N.; Liu, Y. J. *Chemistry of Materials* **2005,** *17*, 1548-1552.

24. Zhang, Y. H.; Ebbinghaus, S. G.; Weidenkaff, A.; Kurz, T.; von Nidda, H. A. K.; Klar, P. J.; Gungerich, M.; Reller, A. *Chemistry of Materials* **2003,** *15*, 4028-4033.

25. Prevo, B. G.; Velev, O. D. *Langmuir* **2004,** *20*, 2099-2107.

26. NIST, NIST X-ray Photoelectron Spectroscopy Database. National Institute of Standards and Technology: 2003.

27. Li, S. P.; Qin, Y. J.; Shi, J. H.; Guo, Z. X.; Yongfang, L.; Zhu, D. B. *Chemistry of Materials* **2005,** *17*, 130-135.

28. Pawar, A. B.; Kretzschmar, I. *Langmuir* **2008,** *24*, 355-358.

29. Galuska, A. A.; Uht, J. C.; Marquez, N. *Journal of Vacuum Science & Technology a-Vacuum Surfaces and Films* **1988,** *6*, 110-122.

30. Gonbeau, D.; Guimon, C.; Pfisterguillouzo, G.; Levasseur, A.; Meunier, G.; Dormoy, R. *Surface Science* **1991,** *254*, 81-89.

31. Werfel, F.; Brummer, O. *Physica Scripta* **1983,** *28*, 92-96.

32. Kalyanasundaram, K.; Gratzel, M. *Coordination Chemistry Reviews* **1998,** *177*, 347-414.

33. Love, J. C.; Gates, B. D.; Wolfe, D. B.; Paul, K. E.; Whitesides, G. M. *Nano Letters* **2002,** *2*, 891-894.

34. Gates, B.; Yin, Y. D.; Xia, Y. N. *Chemistry of Materials* **1999,** *11*, 2827-2836.

35. Velev, O. D.; Jede, T. A.; Lobo, R. F.; Lenhoff, A. M. *Chemistry of Materials* **1998,** *10*, 3597-3602.

36. Miller, S.; Berning, G. L. P.; Plank, H.; Roth, J. *Journal of Vacuum Science & Technology a-Vacuum Surfaces and Films* **1997,** *15*, 2029-2034.

37. Arvieu, C.; Manaud, J. P.; Quenisset, J. M. *Journal of Alloys and Compounds* **2004,** *368*, 116-122.

38. Cui, J. Q.; Kretzschmar, I. *Langmuir* **2006,** *22*, 8281-8284.

39. Cahill, D. G.; Allen, T. H. *Applied Physics Letters* **1994,** *65*, 309-311.

40. Eufinger, K.; Poelman, D.; Poelman, H.; De Gryse, R.; Marin, G. B. *Applied Surface Science* **2007,** *254*, 148-152.

41. Dingley, D. J.; Randle, V. *Journal of Materials Science* **1992,** *27*, 4545-4566.

42. Wilkinson, A. J.; Hirsch, P. B. *Micron* **1997,** *28*, 279-308.

43. Nam, H. J.; Amemiya, T.; Murabayashi, M.; Toh, K. *Journal of Physical Chemistry B* **2004,** *108*, 8254-8259.

44. Mills, A.; Lepre, A.; Elliott, N.; Bhopal, S.; Parkin, I. P.; O'Neill, S. A. *Journal of Photochemistry and Photobiology a-Chemistry* **2003,** *160*, 213-224.

45. Mattox, D. M., *Handbook of Physical Vapor Deposition (PVD) Processing: Film Formation, Adhesion, Surface Preparation and Contamination Control*. Noyes Publications: Westwood, NJ, 1998.

46. Zhang, J. H.; Sun, Z. Q.; Yang, B. *Current Opinion in Colloid & Interface Science* **2009,** *14*, 103-114.

47. Li, Q.; Retsch, M.; Wang, J. J.; Knoll, W. G.; Jonas, U., Porous Networks Through Colloidal Templates. In *Templates in Chemistry Iii*, 2009; Vol. 287, pp 135-180.

Chapter 5

1. Hammond, P. T. *Advanced Materials* **2004,** *16*, 1271-1293.

2. Shimomura, M.; Sawadaishi, T. *Current Opinion in Colloid & Interface Science* **2001,** *6*, 11-16.

3. Ikkala, O.; ten Brinke, G. *Chemical Communications* **2004**, 2131-2137.

4. Graham-Brady, L. L.; Arwade, S. R.; Corr, D. J.; Gutierrez, M. A.; Breysse, D.; Grigoriu, M.; Zabaras, N. *Probabilistic Engineering Mechanics* **2006,** *21*, 193-199.

5. Garcia, R.; Martinez, R. V.; Martinez, J. *Chemical Society Reviews* **2006,** *35*, 29-38.

6. Xia, Y. N.; Gates, B.; Yin, Y. D.; Lu, Y. *Advanced Materials* **2000,** *12*, 693-713.

7. Beams, J. W. *Reviews of Modern Physics* **1938,** *10*, 0245-0263.

8. Schneider, W. C.; Hogeboom, G. H. *Cancer Research* **1951,** *11*, 1-22.

9. Waage, E. V.; Rabinovi.Bs. *Chemical Reviews* **1970,** *70*, 377-387.

10. Sharma, V.; Park, K.; Srinivasarao, M. *Materials Science & Engineering R-Reports* **2009,** *65*, 1-38.

11. Philipse, A. P. *Current Opinion in Colloid & Interface Science* **1997,** *2*, 200-206.

12. Thomas, V.; Dean, D. R.; Vohra, Y. K. *Current Nanoscience* **2006,** *2*, 155-177.

13. Vankelecom, I. F. J. *Chemical Reviews* **2002,** *102*, 3779-3810.

14. Ulbricht, M. *Polymer* **2006,** *47*, 2217-2262.

15. Jung, S.; Ehlert, S.; Mora, J. A.; Kraiczek, K.; Dittmann, M.; Rozing, G. P.; Tallarek, U. *Journal of Chromatography A* **2009,** *1216*, 264-273.

16. Ehlert, S.; Roesler, T.; Tallarek, U. *Journal of Separation Science* **2008,** *31*, 1719-1728.

17. Muller, C. R.; Holland, D. J.; Sederman, A. J.; Mantle, M. D.; Gladden, L. F.; Davidson, J. F. In *Magnetic Resonance Imaging of fluidized beds*, 2008; pp 53-62.

18. Jiang, P.; Hwang, K. S.; Mittleman, D. M.; Bertone, J. F.; Colvin, V. L. *Journal of the American Chemical Society* **1999,** *121*, 11630-11637.

19. Cui, J. Q.; Kretzschmar, I. *Langmuir* **2006,** *22*, 8281-8284.

20. Marrazzo, C.; Di Maio, E.; Iannace, S.; Nicolais, L. *J. Cell. Plast.* **2008,** *44*, 37-52.

Chapter 6

1. Joannopoulos, J. D.; Villeneuve, P. R.; Fan, S. H. *Nature* **1997,** *386*, 143-149.

2. Lopez, C. *Advanced Materials* **2003,** *15*, 1679-1704.

3. Lopez, C. *Journal of Optics a-Pure and Applied Optics* **2006,** *8*, R1-R14.

4. Joannopoulos, J. D.; Johnson, S. G.; Winn, J. N.; Meade, R. D., *Photonic Crystals - Molding the flow of light*. Princeton University Press: 2008.

5. Yablonovitch, E. *Physical Review Letters* **1987,** *58*, 2059-2062.

6. Painter, O.; Lee, R. K.; Scherer, A.; Yariv, A.; O'Brien, J. D.; Dapkus, P. D.; Kim, I. *Science* **1999,** *284*, 1819-1821.

7. Kim, J.; Benson, O.; Kan, H.; Yamamoto, Y. *Nature* **1999,** *397*, 500-503.

8. Michler, P.; Kiraz, A.; Becher, C.; Schoenfeld, W. V.; Petroff, P. M.; Zhang, L. D.; Hu, E.; Imamoglu, A. *Science* **2000,** *290*, 2282-2285.

9. Gratzel, M. *Nature* **2001,** *414*, 338-344.

10. Natarajan, H.; Song, J. H.; Kretzschmar, I.; Menom, V. M. *Optical Express* **2009**.

11. Chung, Y. W.; Leu, I. C.; Lee, J. H.; Hon, M. H. *Langmuir* **2006,** *22*, 6454-6460.

12. Chung, Y. W.; Leu, I. C.; Lee, J. H.; Hon, M. H. *Applied Physics a-Materials Science & Processing* **2004,** *79*, 2089-2092.

13. Kim, M. H.; Im, S. H.; Park, O. O. *Advanced Functional Materials* **2005,** *15*, 1329-1335.

14. Im, S. H.; Park, O. O. *Langmuir* **2002,** *18*, 9642-9646.

15. Galisteo-Lopez, J. F.; Palacios-Lidon, E.; Castillo-Martinez, E.; Lopez, C. *Physical Review B* **2003,** *68*.

16. Nikolaev, I. S.; Lodahl, P.; Vos, W. L. *Journal of Physical Chemistry C* **2008,** *112*, 7250-7254.

17. Cifuentes, A.; Canalejas, P.; Ortega, A.; Diez-Masa, J. C. *Journal of Chromatography* **1998**, *283*, 561-571.

18. Pickett, G. T.; Gross, M.; Okuyama, H. *Physical Review Letters* **2000,** *85*, 3652-3655.
19. Mueller, G. E. *Powder Technology* **2005,** *159*, 105-110.

20. Smoukov, S. K.; Gangwal, S.; Marquez, M.; Velev, O. D. *Soft Matter* **2009,** *5*, 1285-1292.

21. Chen, X.; Mao, S. S. *Chemical Reviews* **2007,** *107*, 2891-2959.

22. Gangwal, S.; Cayre, O. J.; Velev, O. D. *Langmuir* **2008,** *24*, 13312-13320.

23. Brown, W. F., *Magnetic Materials*. McGraw-Hill: New York, 1958.